https://ntrs.nasa.gov/search.jsp?R=19740010532 2020-03-23T10:42:29+00:00Z

NASA CONTRACTOR REPORT

NASA CR-2275

NASA CR-2275

EXPERIMENTAL INVESTIGATION OF MODEL VARIABLE-GEOMETRY AND OGEE TIP ROTORS

by Anton J. Landgrebe and E. Dean Bellinger

Prepared by
UNITED AIRCRAFT RESEARCH LABORATORIES
East Hartford, Conn. 06108
for Langley Research Center

NATIONAL AERONAUTICS AND SPACE ADMINISTRATION • WASHINGTON, D. C. • FEBRUARY 1974

1. Report No.	2. Government Accession No.	3. Recipient's Catalog No.
NASA CR- 2275		

4. Title and Subtitle	5. Report Date
EXPERIMENTAL INVESTIGATION OF MODEL VARIABLE-GEOMETRY AND OGEE TIP ROTORS	February 1974
	6. Performing Organization Code
7. Author(s)	8. Performing Organization Report No.
Anton J. Landgrebe and E. Dean Bellinger	-
	10. Work Unit No.
9. Performing Organization Name and Address	
United Aircraft Research Laboratories East Hartford, CT 06108	11. Contract or Grant No. NAS 1-10906
	13. Type of Report and Period Covered
12. Sponsoring Agency Name and Address	Contractor Report
National Aeronautics and Space Administration Washington, DC 20546	14. Sponsoring Agency Code

15. Supplementary Notes

This is a final report.

16. Abstract

An experimental investigation was conducted to systematically explore the effects of inter-blade spatial relationships and pitch variations on rotor performance and wake geometry. Variable-geometry rotors consisting of various combinations of blade length, axial spacing, azimuth spacing, and collective pitch were tested at model scale in hover and forward flight. In addition, a hover test of a model rotor with an ogee blade tip design was conducted to determine its performance and wake characteristics. The results of this investigation indicate that properly selected variable-geometry rotor configurations can offer substantial improvements in hover performance without adversely affecting forward flight performance. Axial spacing of alternate blades was found to provide the greatest performance benefit, and further improvements were achieved by combining azimuth spacing with axial spacing. The performance benefit appears to be related to the relief of local adverse aerodynamic phenomena produced by vortex interference. The ogee tip design was found to substantially reduce the concentrated core intensity of the tip vortex, and could thus prove beneficial for the relief of blade-vortex interaction problems. However, the ogee tip was found to reduce hover performance at model scale.

17. Key Words (Suggested by Author(s))	18. Distribution Statement
Rotor configurations Rotor performance Rotor wake flow Blade tip shape	Unclassified

19. Security Classif. (of this report)	20. Security Classif. (of this page)	21. No. of Pages	22. Price*
Unclassified	Unclassified	112	Domestic, $4.25 Foreign, $6.75

*For sale by the National Technical Information Service, Springfield, Virginia 22151

CONTENTS

	Page
SUMMARY	1
INTRODUCTION	1
LIST OF SYMBOLS	3
VARIABLE-GEOMETRY ROTOR CONFIGURATIONS	6
Definition of Variable-Geometry Rotor Parameters	6
Selection of Rotor Configurations	7
VARIABLE-GEOMETRY ROTOR HOVER TEST	9
Test Equipment	9
Test Conditions	10
Test Procedures	12
Calibration	12
Data Acquisition	12
Data Reduction	13
Performance Data	13
Flow Visualization Data	13
Data Accuracy	14
Discussion of Hover Performance Results	15
Conventional Rotor	16
Effects of Azimuth Spacing and Axial Spacing	16
Effect of Collective Pitch Increment	18
Effect of Differential Radius	19
Effect of Combining Differential Radius and Differential Collective Pitch	21
Discussion of Flow Visualization Results	22
WIND TUNNEL TEST OF VARIABLE-GEOMETRY ROTORS	27
Test Equipment	27
Test Configurations and Operating Conditions	27
Test Procedures, Data Reduction and Accuracy	29
Discussion of Wind Tunnel Results	29
Performance Characteristics	29
Vibration Characteristics	30
Flapping Characteristics	31
HOVER TEST OF MODEL ROTOR BLADES WITH OGEE TIPS	32
CONCLUSIONS AND RECOMMENDATIONS	36
REFERENCES	38
FIGURES 1-54	40-110

EXPERIMENTAL INVESTIGATION OF MODEL VARIABLE-GEOMETRY AND OGEE TIP ROTORS

Anton J. Landgrebe and E. Dean Bellinger
United Aircraft Research Laboratories

SUMMARY

An experimental investigation was conducted to systematically explore the effects of inter-blade spatial relationships and pitch variations on rotor performance and wake geometry. Variable-geometry rotors consisting of various combinations of blade length, axial spacing, azimuth spacing, and collective pitch were tested at model scale in hover and forward flight. In addition, a hover test of a model rotor with an ogee blade tip design was conducted to determine its performance and wake characteristics. The results of this investigation indicate that properly selected variable-geometry rotor configurations can offer substantial improvements in hover performance without adversely affecting forward flight performance. Axial spacing of alternate blades was found to provide the greatest performance benefit, and further improvements were achieved by combining azimuth spacing with axial spacing. The performance benefit appears to be related to the relief of local adverse aerodynamic phenomena produced by vortex interference. The ogee tip design was found to substantially reduce the concentrated core intensity of the tip vortex, and could thus prove beneficial for the relief of blade-vortex interaction problems. However, the ogee tip was found to reduce hover performance at model scale.

INTRODUCTION

The importance of aerodynamic interactions between helicopter rotor blades and their tip vortices is well recognized. Many analytical and experimental programs have been conducted in recent years to study rotor-wake interaction effects. For example, previous experimental studies at the United Aircraft Research Laboratories (UARL), reported in Refs. 1 through 4 and other unpublished reports, have shown the relation between rotor hover performance and wake geometry as influenced by basic blade design parameters (solidity, aspect ratio, twist, taper, and airfoil section), rotor operational parameters (collective pitch and tip speed) and blade tip design. Also, analytical studies at UARL to determine wake effects for both hovering and forward flight conditions have been reported in Refs. 4 through 7. These studies have shown

that rotor hover performance is sensitive to wake geometry variations. Thus, if rotor wake geometry is properly modified through new rotor design concepts, it might be expected that significant performance benefits could be achieved. For example, with helicopter gross weights normally limited by hover performance, and payloads typically 20 to 25 percent of gross weight, an increase in hovering lift capability of 5 percent could result in a 20 to 25 percent increase in payload.

Previously, rotor design changes directed toward improving rotor performance and controlling tip vortex - blade interaction have mainly consisted of changes in individual blade and tip designs. Other than changing number of blades, very little has been done to change the spatial relationship between blades. Relieving the conventional geometric design constraints of rotors such as coplanar blades, equal blade azimuth spacing, equal blade length, and equal blade collective pitch values, opens an entirely new dimension of design variables. The potential for certain combinations of the new design variables to result in improved rotor configurations had not been explored in depth. However, it was recognized that reorientation of the tip vortices relative to the blades, as provided by these new design variables, could potentially lead to improvements in rotor performance and possibly rotor dynamic and noise characteristics. Thus, a model variable-geometry rotor (VGR) was designed and tested to explore the effects of differential radius, axial spacing, azimuth spacing, and collective pitch. As conceived at the NASA Langley Research Center, the variable-geometry rotor is essentially composed of two corotating conventional rotor systems, with equal number of blades, that can be axially and azimuthally spaced relative to one another. Alternate blades can have unequal length and unequal collective pitch settings.

The objective of this model rotor investigation was to systematically explore the effects of inter-blade spatial relationships on rotor performance and wake geometry to determine promising rotor configurations for full-scale applications.

Detrimental blade-vortex interactions may also be alleviated by reducing the intensity of the vortex during formation by suitable tip-shape modifications. An additional objective of this investigation was to test such a tip-shape proposed by the NASA Langley Research Center. This design known as the "ogee" tip was adapted to a conventional model rotor and tested as part of this investigation to explore its influence on rotor hover performance and wake characteristics.

LIST OF SYMBOLS

AR	blade aspect ratio, R/c
b	number of blades in rotor
c	blade chord, cm (or in.)
c_o	chord of reference blade (longest blade), cm (or in.)
C_D	rotor drag coefficient: $\text{drag}/\rho\pi R_o^2(\Omega R_o)^2$
C_L	rotor lift coefficient: $\text{lift}/\rho\pi R_o^2(\Omega R_o)^2$
C_Q	rotor torque coefficient: $\text{torque}/\rho\pi R_o^3(\Omega R_o)^2$
C_T	rotor thrust coefficient: $\text{thrust}/\rho\pi R_o^2(\Omega R_o)^2$
e	flapping hinge offset distance from shaft axis, cm (or in.)
M_T	Mach number at tip of blade, ΩR/speed of sound
M_{T_o}	tip Mach number of longest blades in differential radius configurations
$\bar{r}$	radial coordinate from rotor shaft axis to point on tip vortex, nondimensionalized by R_o, (see Fig. 9)
R	rotor radius (or blade set radius), cm (or in.)
R_o	radius of rotor (or blade set) with reference blades (longest blades), cm (or in.)
t	time, sec
V	forward velocity or tunnel flow velocity, m/sec (or ft/sec)
z	axial distance, measured along rotor axis relative to upper hub, positive up, cm (or in.)
$\bar{z}$	axial coordinate relative to center of upper hub nondimensionalized by R_o, $\bar{z} = z/R_o$, (see Fig. 9)

$\bar{z}_T$ tip vortex axial coordinate relative to the tip of blade, nondimensionalized by R_o, positive up (see Fig. 9)

α_s rotor shaft angle, angle between forward velocity and plane normal to shaft axis, positive nose up, deg

β blade flapping angle relative to coned position, deg

β_{PTP} peak-to-peak amplitude of blade flapping angle, deg

γ blade Lock number

δ blade root cutout, measured from shaft axis, cm (or in.)

ΔR radius increment between blades sets (1) and (2), $R_{(1)}-R_{(2)}$, (see Fig. 1), cm (or in.)

$\overline{\Delta R}$ radius increment ratio, $\Delta R/R_o$

Δz axial spacing between hubs of upper and lower blade sets, $z_{(1)}-z_{(2)}$, (see Fig. 1), cm (or in.)

$\overline{\Delta z}$ axial spacing ratio, $\Delta z/c_o$

$\Delta\theta$ collective pitch angle increment between blade sets (1) and (2), $\theta_{(1)}-\theta_{(2)}$, deg

$\Delta\psi$ azimuth spacing, azimuth increment between blade sets (1) and (2), $\psi_{(1)}-\psi_{(2)}$, (see Fig. 1), deg

θ_1 blade linear twist, deg

θ collective pitch angle (mean pitch value for configurations with $\Delta\theta \neq 0$), deg

θ_{75} collective pitch angle at 0.75 R, deg

μ rotor advance ratio, $V/\Omega R_o$

ρ air density, gram-sec^2/cm^4

σ rotor solidity ratio, $\sigma = bc/\pi R$

ψ blade azimuth angle, measured in the direction of rotation; for hover test: measured from plane of smoke; for wind tunnel test: measured from the downstream blade position, deg

ψ_1 azimuth angle of blade 1, deg; in flow visualization photographs blade 1 is defined as the blade which most recently passed through the reference plane of smoke.

$\psi_{(1)}, \psi_{(2)}$ azimuth angle of a blade of the upper or lower rotor, respectively, deg; in flow visualization photographs $\psi_{(1)}$ is the azimuth angle of the upper blade which most recently passed through the reference plane of smoke.

ψ_w tip vortex azimuth angle, azimuth angle of point on tip vortex relative to the blade from which it was shed, measured from the blade (see Fig. 9), deg

ψ_{w_1} tip vortex azimuth angle relative to blade 1, deg

Ω rotor rotational frequency, rad/sec

Subscripts

0 subscript indicating reference blade (longest blade)

1,2 subscripts indicating blade number

(1), (2) subscripts indicating blade sets (1) and (2); except for coplanar blade sets: (1) = upper blade set, (2) = lower blade set; for coplanar blades: (1) = larger blade set, (2) = smaller blade set

VARIABLE-GEOMETRY ROTOR CONFIGURATIONS

Definition of Variable-Geometry Rotor Parameters

For a 6-bladed rotor, a wide range of rotor configurations can be achieved with a variable-geometry model without unbalancing the total rotor system by considering the blades to be divided into two separate blade sets in which each set of three blades is symmetric as shown in Fig. 1. The blades within each blade set are coplanar, azimuthally symmetric, and equal in length. Also, the collective pitch angles of the blades within a blade set are the same. The major parameters that were investigated are defined below in Table I in terms of dimensional values for the two blade sets (subscripted (1) and (2)) and the reference radius (R_o) and chord length (c_o). The reference radius (R_o) and reference chord (c_o) correspond to those of the longest blades tested -- 0.7 m (27.5 in.) and 3.73 cm (1.47 in.), respectively. The major parameters are termed variable-geometry rotor parameters or simply VGR parameters.

TABLE I

DEFINITIONS OF VARIABLE-GEOMETRY ROTOR PARAMETERS

VGR Parameter	Symbol and Definition	
Axial Spacing Ratio.	$\Delta z = \frac{\overline{\Delta z}}{c_o} = \frac{z_{(1)} - z_{(2)}}{c_o}$	(1)
Radius Increment Ratio	$\Delta R = \frac{\overline{\Delta R}}{R_o} = \frac{R_{(1)} - R_{(2)}}{R_o}$	(2)
Azimuth Spacing, deg	$\Delta\psi = \psi_{(1)} - \psi_{(2)}$	(3)
Collective Pitch Increment, deg...	$\Delta\theta = \theta_{(1)} - \theta_{(2)}$	(4)

The convention used to distinguish between blade sets 1 and 2 is that blade set 1 is the upper rotor and blade set 2 is the lower rotor. For coplanar configurations, where there is no upper or lower rotor, the largest diameter blade set is defined as blade set 1. In accordance with these definitions, the axial spacing ratio is always a positive quantity whereas the other VGR parameters may be either positive or negative. The azimuth spacing value used is always the minimum spacing (e.g., in Fig. 1 $\Delta\psi$ = 30 deg not $\Delta\psi$ = 90 deg). The notation and sign conventions used to describe the variable-geometry rotor parameters are included in Fig. 1 for quick reference.

Selection of Rotor Configurations

The primary consideration in the selection of the specific variable-geometry rotor configurations for this investigation was to provide configurations which would include a wide but realistic range of the VGR parameters. The values listed below in Table II were selected as the nominal values for the VGR parameters which were tested in varied combinations on a 6-bladed rotor.

TABLE II

TEST VALUES OF VARIABLE-GEOMETRY ROTOR PARAMETERS

VGR Parameters	Nominal Test Values*
Axial Spacing Ratio, $\overline{\Delta z}$	0, 1, (2)
Radius Increment Ratio, $\overline{\Delta R}$	0, $\pm$0.15, ($\pm$0.30)
Azimuth Spacing, $\Delta\psi$, deg	0, $\pm$15, $\pm$30, 60
Collective Pitch Increment, $\Delta\theta$, deg..	0, ($\pm$2)
*Parentheses indicate secondary test values.	

Schematics of the variable-geometry rotor configurations showing the blades positioned according to each of the VGR parameter values are presented in Fig. 2. In addition to varied combinations of the values in Table II, other values were used for a small number of test conditions (e.g., $\Delta\psi = \pm 45$ deg, $\overline{\Delta z} = 1.5$ and 2.5).

Axial spacing ratios of 1 and 2 chord lengths were believed to be within the practical limit considering reasonable limitations of shaft size, weight and drag. Except for the coplanar configurations, complete flexibility in the selection of blade azimuth spacing, $\Delta\psi$, was available. The values in Table II were selected considering a 6-bladed test rotor. For coplanar configurations the azimuth spacings were limited to 60 and $\pm$30 deg due to the physical constraints at the rotor hub. For collective pitch increment, $\Delta\theta$, the selected values of $\pm$2 deg correspond to increasing and decreasing the pitch angle on each blade set by one degree relative to the pitch setting of a reference configuration having no differential collective pitch. A rotor with six blades was available as the reference radius rotor ($\overline{\Delta R} = 0$). Two blade sets, each with three blades, were fabricated with radii of 70 and 85 percent

of the radius of the reference blade set to provide the additional values in radius increment ratio, $\overline{\Delta R}$, of 0.30 and 0.15, respectively. When establishing the blade design for the two shorter blade sets, constant solidity was maintained by varying the chord between blade sets. The offset of the flapping hinge (e) and the dimensional root cutout distance was also maintained constant between blade sets of varying diameter. The values of the rotor design parameters for each of the blade sets with varying blade length are tabulated in Table III.

TABLE III

ROTOR DESIGN PARAMETERS*

Design Parameters	Blade Set 1	Blade Set 2	Blade Set 3
Number of blades in blade set. . .	3	3	3
Blade radius, R, cm (in.).	69.85(27.5)	59.37(23.37)	48.90(19.25)
Blade chord, c, cm (in.)	3.73(1.47)	4.39(1.73)	5.33(2.10)
Blade aspect ratio, AR	18.7	13.5	9.2
Blade twist, θ_1, deg.	0	0	0
Blade taper.	0	0	0
Blade airfoil section (NACA) . . .	0012	0012	0012
Flapping hinge offset ratio, e/R .	0.093	0.110	0.133
Flapping hinge offset ratio, e/R_o.	0.093	0.093	0.093
Blade root cutout, δ/R.	0.171	0.212	0.245
Blade root cutout, δ/R_o	0.171	0.171	0.171
Rotor solidity (for six blades). .	0.102	0.102	0.102

*Total number of blades in rotor = 6.

VARIABLE-GEOMETRY ROTOR HOVER TEST

Test Equipment

The hover test program was conducted at the UARL model rotor hover test facility. The test facility, shown in Fig. 3, is located in a large enclosed area of sufficient size to prevent significant wall and ground effects. The facility is equipped with a rotor test rig, smoke and schlieren flow visualization equipment, thrust and torque instrumentation, and a movable ground plane. For this test the ground plane was positioned at 3.5 rotor radii below the rotor for testing out of ground effect. Photographs of a variable-geometry rotor configuration on the model rotor test rig are shown in Fig. 4 and close-ups of the rotor hubs are shown in Fig. 5. A 40-horsepower, variable speed electric motor was used as a power source. The rotor was driven through a 3:1 speed reduction system to allow operation at a tip speed of 198 m/sec (650 ft/sec). Average rotor thrust and torque measurements were made by means of strain-gaged load cells. The motor-balance assembly is shown in the schematic cross section of the rotor test rig in Fig. 6. The rig instrumentation used to monitor the operation included a solid state counter for measuring rotor rpm, a vibration meter, and a model power control console.

Flow visualization equipment included the following:

1. Variable position smoke rakes.

2. A 70 mm camera and two high-intensity, short duration light sources.

3. An electronic time-delay control to permit photographing of the cyclic time history of the rotor wake.

4. A Fastax movie camera and high-intensity lights for high frame-speed movies.

5. A light source, mirrors, schlieren knife edge, and Fastax movie camera for high-speed schlieren movie photography.

The model rotor system consisted of rotor hubs and model blades which provided all required combinations of axial spacing, azimuth spacing, radius ratio, and collective pitch. Two separate rotor hub systems were used for the coplanar and noncoplanar rotors, as shown in Fig. 5. Azimuth spacing variations were achieved in the coplanar hub through indexing the blade cuffs within a circular slot in the hub. Due to the physical interference constraint for the coplanar hub, the spacing between adjacent blades was restricted to a minimum of 30 degrees. For the noncoplanar hub, the relative

azimuth spacing of the two blade sets was varied by rotating the lower hub on the shaft relative to the upper hub. Hinges were provided in the blade cuffs to provide flapping articulation. The model blade design consisted of an aluminum spar and balsa trailing-edge section. The blades were designed such that the elastic axis, chordwise center of gravity, and aerodynamic center were coincident at the quarter-chord position. The mass and stiffness properties of the model blades greatly exceeded those of model blades dynamically scaled from typical full-scale blades. For example, the Lock number of the larger blades (aspect ratio = 18.2) operating at a tip speed of 198 m/sec (650 fps) was 3.5 compared to a typical full-scale Lock number of 10. Hence, model blade coning angles were lower than full-scale coning angles. However, the use of such rotor blades permitted concentration on the aerodynamic, rather than the aeroelastic aspects of rotor hover performance. A tabulation of the blade design parameters was presented in Table III. Photographs of the model blades are presented in Fig. 7.

Test Conditions

The hover test was divided into two phases. In Phase 1, reasonable combinations of the test parameter values were selected for a 6-bladed rotor following the division of the VGR parameters into the primary and secondary values which were noted in Table II. All combinations of the primary test values were tested in Phase 1, as well as most combinations of primary and secondary values. However, no testing was conducted of combinations consisting of only secondary values in this phase. Phase 2 consisted of testing combinations of some VGR parameters not included in Phase 1 in addition to some Phase 1 configurations over an extended range of collective pitch values. A summary of the rotor configurations and test conditions for the VGR hover test is presented in Table IV.

All test configurations were operated at two rotational speeds, Ω, 218.2 rad/sec and 283.6 rad/sec, which correspond to tip speeds of 152.4 m/sec (500 fps) and 198.1 m/sec (650 fps), respectively, for the larger diameter blade set. For the reduced diameter blade sets the tip speeds were proportionally lower due to the constant rotational speeds. The rotor tip speeds and corresponding tip Mach numbers for all configurations are presented in Table V. For the conventional rotor and for configurations representing independent variations of the major variables ($\overline{\Delta R}$, $\overline{\Delta z}$, $\Delta\psi$, and $\Delta\theta$), five nominal values of collective pitch (θ = 0, 6, 8, 10, 11 deg) were tested to provide reference performance results. The maximum collective pitch of 11 deg was determined by a sharp increase in rotor noise level for several configurations at the higher tip speed (198 m/sec). This boundary was explored during the tests of Ref. 1 and was found to be related to incipient stall flutter. For other configurations, a minimum of two nominal collective pitch values (θ = 8, 10 deg) were tested.

TABLE IV

ROTOR CONFIGURATIONS AND TEST CONDITIONS FOR THE VARIABLE-GEOMETRY-ROTOR HOVER TEST

	No. of Blades	Collective Pitch Increment, $\Delta\theta$	Axial Spacing Ratio, $\Delta\bar{z}$	Radius Increment Ratio, $\Delta\bar{R}$	Azimuth Spacing $\Delta\psi$, deg	No. of VGR Parameter Combinations	Minimum No. of Collective Pitch, θ, Values	No. of Tip Speeds, ΩR	Minimum No. of Test Conditions	
Phase 1	6	0	0	0	60	1	5	2	10	Conventional 6-bladed rotor
	"	"	"	"	30	1	5	2	10	Independent azimuth spacing variation
	"	"	"	0.15,0.30	60	2	5	2	20	Independent radius ratio variation
	"	"	"	"	$\pm$30	4	2	2	16	
	"	"	1.0	0	60	1	5	2	10	Independent vertical spacing variation
	"	"	"	0,$\pm$0.15	0,$\pm$15,$\pm$30	15	2	2	60	
	"	"	"	$\pm$0.15	60	2	2	2	8	
	"	"	"	$\pm$0.30	0,$\pm$15,$\pm$30, 60	12	2	2	48	
	"	"	2.0	0	60	1	5	2	10	Independent vertical spacing variation
	"	"	"	0,$\pm$0.15	0,$\pm$15,$\pm$30	15	2	2	60	
	"	"	"	$\pm$0.15	60	2	2	2	8	
	"	$\neq$0	0	0	60	1	5	2	10	Independent pitch ratio variation
	"	"	"	"	30	1	2	2	4	
	"	"	"	0.15	30,60	2	2	2	8	
	"	"	1.0	0,$\pm$0.15	0,$\pm$15,$\pm$30, 60	20	2	2	80	
						76			362	Totals
Phase 2	6	0	1.0	0	45,-45	2	3	2	12	
	"	"	1.5,2.5	"	30	2	2	2	8	
	"	$\neq$0	2.0	"	30	1	1	2	2	
						5			22	Totals

TABLE V

ROTOR TIP SPEEDS AND TIP MACH NUMBERS FOR
THE VARIABLE-GEOMETRY ROTOR HOVER TEST

Blade Set Radius R, cm (in.)	Ω = 218.2 rad/sec		Ω = 283.6 rad/sec	
	Tip Speed ΩR, m/sec (fps)	Tip Mach Number M_T	Tip Speed ΩR, m/sec (fps)	Tip Mach Number M_T
69.85 (27.5)	152.4 (500)	0.45	198.1 (650)	0.58
59.37 (23.37)	129.5 (425)	0.38	168.4 (552.5)	0.49
48.90 (19.25)	106.7 (350)	0.31	138.7 (455)	0.41

Test Procedures

Calibration. - Prior to testing, the thrust and torque derivatives (thrust and torque per strain-gage unit) were determined by statically applying known forces and moments to the rotor hub.

Collective pitch angle was set manually with an estimated accuracy of $\pm$0.2 deg. Blade tracking was checked by observing the blade tips through a transit with lighting supplied by a strobotac. To calibrate the flow visualization photographs and to minimize errors due to camera angle and lens distortion, a planar grid indicating 2 percent increments of the rotor radius was placed in the plane of the smoke (reference plane) and photographed prior to the test. Photographs of this grid system were used in the construction of a grid template overlay for the reduction of the flow visualization photographs to radial and axial wake coordinates. The blade azimuth position was calibrated for each Ω by calculating the delay time between the passage of a reference blade through the reference plane and the passage of a single tooth gear mounted on the rotor shaft.

Data acquisition. - The procedure for data acquisition was similar to that described in Ref. 1. Each test condition was repeated at least twice within a test run (a test run consisted of data recorded between the starting and stopping of the rotor rotation), and the results were averaged. Many of the test conditions were repeated to check the repeatability of the data.

To obtain flow visualization data, smoke was injected into the flow by movable smoke rakes located above and to the side of the rotor. The smoke rakes were positioned by remote control to insure a clearly defined tip vortex. The wake patterns were recorded on film with remotely operated cameras. Illumination was provided for still photographs by two microflash units (time duration 0.5 microsecond for stop action). A time-delay system was used to trigger the cameras and microflash units when the rotor was at a desired azimuth position. The delay system used a one/rev signal from the rotor shaft as a reference, and the delay time (manually adjusted) was measured on an electronic counter. For each test condition, 70 mm photographs were taken at preselected azimuth positions of a reference blade with respect to the plane of the smoke. A sample flow visualization photograph is presented in Fig. 8. Photographs were generally taken at azimuth angles of 0, 15, 30, 45, 60, 90, and 105 deg. To supplement these still photographs and to assist in the interpretation thereof, high frame-speed movies (4000 frames/sec) using schlieren techniques were taken at selected conditions.

Data Reduction

Performance data. - Thrust and torque measurements were converted to thrust coefficient-solidity ratio (C_T/σ), and torque coefficient-solidity ratio (C_Q/σ) values for all test conditions. The air density (ρ) used in nondimensionalizing the data was calculated for each test condition, based on the recorded temperature and pressure readings.

Flow visualization data. - To take advantage of the symmetrical nature of the near wake of a hovering rotor as well as to facilitate the acquisition of quantitative data, the wake for this investigation was observed by emitting smoke externally from the blades (i.e., in the nonrotating system). Smoke was emitted from smoke rakes in a single plane and the flow patterns were photographed, as shown in Fig. 8. In this manner, a two-dimensional cross section of the wake near the rotor was recorded. The cross sections of the tip vortices appear as circles in which the central regions are clear of smoke. The centers of the circular cross sections are interpreted as the centers of the tip vortex core. The vortex sheet cross sections are indicated by the discontinuities present in the smoke filaments passing through the inner region of the rotor wake.

The photographic wake data were analyzed for selected test conditions to determine the tip vortex characteristics. The conditions were selected so as to permit assessment of the effects of the VGR parameters. Radial and axial wake coordinates of the tip vortices were determined from the photographs as functions of the wake azimuth angle (ψ_w), which is equal to the blade azimuth travel ($\psi = \Omega t$) from the time it generates the vortex cross section. To

illustrate the wake azimuth angle concept a schematic of the wake of a 2-bladed rotor is presented in Fig. 9. In this figure, the tip vortex labeled ψ_w = 180 deg was shed from blade 2 which has travelled 180 deg from the time it passed through the plane of the smoke (reference plane). The following tip vortex was shed by blade 1 the previous time it passed through the reference plane, and thus the wake azimuth angle for this tip vortex cross section is 360 deg. It should be noted that the cross sections in the visible wake near the rotor remain approximately in the same plane (rotor wake tangential velocities are small). For the near wake of a hovering rotor, the wake coordinates for each blade at a given azimuth angle are essentially equivalent due to symmetry.

The coordinates of the wake for a given test condition were determined by the following procedure. A transparent grid template was constructed from the photograph of the reference grid. With the grid template as an overlay, the radial and axial coordinates of the wake from several blades in a single photograph were determined along with the corresponding wake azimuth coordinates. This was repeated for a sequence of photographs taken with the rotor at a series of prescribed rotational positions. A sample sequence is presented in Fig. 10, in which the rotor rotational positions are designated by the azimuth position, ψ, of the blade which most recently passed through the reference plane containing the smoke. The radial and axial coordinate results from the series of photographs were then plotted as functions of ψ_w. To facilitate the comparison of wake geometries from varying rotors and test conditions, the radial and axial coordinates were nondimensionalized by the rotor radius, and differences in axial coordinates due to blade coning were eliminated by using the blade tip as the reference ($\bar{z}_T$ instead of $\bar{z}$ in Fig. 9). The range of wake azimuth angles for which data could be acquired was limited by the visibility of the smoke. For 6-bladed rotors, less than one revolution from each blade was visible. However, this was adequate because rotor performance is mainly sensitive to the near wake (region to approximately 0.3 R below rotor).

Data Accuracy

Static data repeatability for thrust and torque was determined from repeated calibrations of the strain gages. Dynamic data repeatability was determined by considering both the deviations from average values from repeated test points within test runs and deviations between repeated test runs. Based on these considerations, the accuracy of the hover performance data is estimated to be within the following values:

	$M_T = 0.45$	$M_T = 0.58$
Thrust Coefficient/Solidity, C_T/σ	± 0.0004	± 0.0003
Torque Coefficient/Solidity, C_Q/σ	± 0.00006	± 0.00004

The estimated values do not reflect scatter in the performance data due to inaccuracies in setting the collective pitch. It will be shown that the collective setting scatter did not significantly influence the thrust-torque performance curves of interest in this investigation.

The estimated accuracies with which the parameters determining a given test condition could be set are given below:

Parameter	Accuracy
Collective Pitch, θ	± 0.2 deg
Tip Speed, ΩR	± 0.3 m/sec (± 1 fps)
Azimuth Increment, $\Delta\psi$	± 2 deg
Axial Spacing, $\overline{\Delta z}$	± 0.02

The estimated accuracy of measuring the tip vortex coordinates are listed below:

Wake Coordinate	Accuracy
Azimuth, ψ_w	± 3 deg
Radial, $\bar{r}$	± 0.005
Axial, $\bar{z}_T$	± 0.005

Discussion of Hover Performance Results

The hover performance test data for each rotor configuration were transformed to graphical form by plotting the rotor thrust-solidity ratio (C_T/σ) versus the torque-solidity ratio (C_Q/σ) for each collective pitch setting (θ) and tip Mach number (M_T). The resulting graphs were analyzed to assess the influence of each of the major variables on model rotor hover performance. It is noted that although the performance results are presented in the C_T/σ, C_Q/σ format, the solidity for all rotor configurations tested was constant ($\sigma = 0.102$), so that the results are also directly representative of comparisons based on C_T and C_Q. In addition, since the radius of the reference blade (R_o) was used throughout in nondimensionalizing, the performance results are also representative of the dimensional thrust-torque variation.

Conventional rotor. - The hover performance of the conventional 6-bladed rotor ($\Delta\bar{z} = 0$, $\Delta\bar{R} = 0$, $\Delta\psi = 60$ deg, $\Delta\theta = 0$) is presented in Fig. 11. Results of repeat runs are included in this figure for $\theta = 8$, 10, and 11 deg to illustrate the repeatability of the test data when collective pitch is reset between test runs. Due to the ± 0.2 deg accuracy of setting collective pitch, some scatter in the performance data is indicated. However, this scatter due to pitch setting was limited to movement along the thrust-torque curve. Since the objective of this investigation is to compare the relative performance efficiency of the various configurations, departures from the reference thrust-torque curves (e.g., thrust increment at a given torque) rather than movements along them are of primary significance. Thus the data in Fig. 11 were averaged in subsequent figures to provide a standard set of conventional rotor data to compare with data for variable-geometry configurations.

Effects of azimuth spacing and axial spacing. - The independent effects of azimuth spacing ($\Delta\psi$) and axial spacing ($\Delta\bar{z}$) on hover performance are presented in Figs. 12 and 13, respectively. For the purposes of this report, an "independent effect" is defined as the independent variation of one VGR variable from the base conventional rotor configuration. Thus, for the independent variation of azimuth spacing ($\Delta\psi$) the other VGR variables are $\Delta\bar{z} = 0$, $\Delta\bar{R} = 60$ deg, and $\Delta\theta = 0$. Likewise, for the independent variation of axial spacing ($\Delta\bar{z}$) the other VGR variables are $\Delta\bar{R} = 0$, $\Delta\psi = 60$ deg, and $\Delta\theta = 0$. It is shown in Fig. 12 that varying the azimuth spacing from the conventional 60 deg to 30 deg has little effect on performance. However, varying axial spacing, as shown in Fig. 13 has a significant effect. An independent axial spacing variation of one chord length ($\Delta\bar{z} = 1$) results in a slight performance benefit only at the high thrust levels, but an axial spacing of two chord lengths ($\Delta\bar{z} = 2$) results in an appreciable performance benefit, particularly at the high thrust - high tip Mach number test conditions. For example, at a C_Q/σ of approximately 0.009 the thrust is increased by five percent. At a C_T/σ of 0.08 the torque is reduced by ten percent. The corresponding change in figure of merit is from 0.55 for the conventional rotor to 0.61. As indicated in Fig. 13 the performance benefit is achieved at the fixed 11 deg collective pitch setting through a decrease in torque as opposed to an increase in thrust. In addition to a possible reduction in induced drag, the performance benefit is probably due to a reduction in the severity of profile drag divergence near stall at the tips of the blades when alternate blades are axially spaced.

The effects on hover performance of combining axial and azimuth spacing are shown in Figs. 14 and 15. For clarity these figures have been divided into parts (a) and (b) to separate the effects of positive and negative azimuth spacing. It is noted that the scale factor has been changed from that of the previous figures. In Fig. 14, the effects of azimuth spacing at an axial spacing, $\Delta\bar{z}$, of one chord length are shown as compared to the

performance of the conventional rotor. Several azimuth spacings result in a substantial improvement in performance which increases with increasing tip Mach number and thrust level. The configurations which demonstrate the greatest improvement at this axial spacing are the $\Delta\psi = 30$, -30, and 45 deg configurations. Also of interest is the difference in performance at similar collective pitch settings for the $\Delta\psi = 0$ configuration for which the blades are positioned one directly above the other. Although the performance curve in Fig. 14(b) is similar to that of the conventional rotor, the performance at a specified pitch setting is shifted down the conventional rotor curve so that a significant decrease in thrust and torque results. The extent of this performance shift increases with collective pitch, and at a pitch setting of 11 deg the pitch increment relative to the conventional rotor value is one deg. Although small shifts in the data points along the performance curve can be attributed to the aforementioned accuracy range of setting the blade pitch (± 0.2 deg), the extent of the shift for this configuration greatly exceeds that range. Also, the pitch setting was not changed between the testing of the $\Delta\psi = 0$ deg and the other azimuth spacing configurations at this axial spacing. Thus, there is a pronounced interference effect between the closely spaced blades which causes the performance shift of this "biplane configuration" relative to the conventional rotor.

The effects of various combinations of azimuth spacing with an axial spacing ($\overline{\Delta z}$) of two chord lengths are shown in Fig. 15. The performance trends with tip Mach number and thrust level are generally consistent with those at the one chord length spacing. However, the improvements in performance are even greater. Also, the performance variations with azimuth spacing are much smaller. For example, whereas a significant performance difference between the $\Delta\psi = 30$ and 60 deg configurations was indicated in Fig. 14 for $\overline{\Delta z} = 1$, only a slight difference occurs at $\overline{\Delta z} = 2$. Even the performance shift at a given pitch setting, noted above for the "biplane configuration", has decreased significantly.

It is concluded from the data presented thus far that axial spacing is the predominant factor in improving hover performance. However, additional improvements may be achieved through combining the proper selection of azimuth spacing with axial spacing. The highest performance increase measured was a seven percent increase in thrust level at a C_Q/σ of approximately 0.009. This performance increase was achieved with the following configuration and operating condition:

$$\overline{\Delta R} = 0, \quad \overline{\Delta z} = 2, \quad \Delta\psi = 30 \text{ deg}, \quad \Delta\theta = 0, \quad b = 6, \quad M_T = 0.58, \quad \theta = 11.5 \text{ deg}$$

A 12 percent decrease in torque was demonstrated for this configuration at a $C_T/\sigma = 0.08$ ($\theta = 11$ deg). The corresponding change in figure of merit is

from 0.55 of the conventional rotor to 0.62. Based on the demonstrated trends, higher performance increases than those measured should be obtainable for the 6-bladed rotor at higher collective pitch settings (thrust levels), tip Mach numbers, and axial spacings. Also, as shown in Fig. 15, for the axial spacing of two chord lengths the performance increase was fairly independent of azimuth spacing, and thus similar performance benefits may have been obtained at other azimuth spacings if tested at the same thrust level.

The question that remains is whether or not the performance continuously improves as axial spacing is increased. In part (a) of Fig. 16, the effect on performance of varying axial spacing in small increments from 1 to 2.5 chord lengths is shown for the 30 deg azimuth spacing. As indicated, the performance of the configuration tested consistently increases with axial spacing. In part (b) of Fig. 16, the data points for three of the $\Delta\psi = 30$ deg configurations from part (a) have been replaced with faired curves to more clearly compare their performance with that of the conventional rotor. At the high thrust - tip Mach number combinations for this configuration, most of the performance benefit is achieved with one chord length axial spacing.

Effect of collective pitch increment. - The independent effect of collective pitch increment, shown in Fig. 17, was determined by setting different collective pitch values on the two blade sets (alternate blades) of the otherwise conventional rotor configuration. The collective pitch increment, $\Delta\theta$, is defined as the total pitch increment between the two blade sets (1) and (2). The collective pitch on each blade set is defined as follows:

$$\theta_{(1)} = \theta + \Delta\theta/2 \tag{5}$$

$$\theta_{(2)} = \theta - \Delta\theta/2 \tag{6}$$

In Fig. 17, the mean collective pitch, θ , is equivalent to the conventional rotor collective pitch at each thrust level. As indicated in Fig. 17, collective pitch increment generally has a negligible effect on performance for conventional axial and azimuth spacing. A slight decrease in performance is shown in Fig. 17 at the high thrust level for the configuration with $\Delta\theta = 2$ deg at the tip Mach number of 0.58. This performance decrease may be simply attributable to the more severe stall of the blade set with the higher pitch setting.

Data showing the effect of collective pitch increment on performance for various combinations of axial and azimuth spacing are presented in Fig. 18. In part (a) of this figure, performance data are presented for an axial spacing of one chord length, several azimuth spacings, and a collective pitch increment between the upper and lower blade sets of 2 deg. The mean collective pitch value for each configuration is 8 deg. Although there are some minor reductions in performance, the primary variations in the data are mainly along the $\Delta\theta = 0$ performance curves. In part (b) of Fig. 18, performance data are presented for a higher mean collective pitch value ($\theta = 11.5$ deg). Results for two axial spacings, $\overline{\Delta z} = 1$ and 2, one azimuth spacing, $\Delta\psi = 30$ deg, and collective pitch increments, $\Delta\theta = 0$ and -1, are shown. At the lower tip Mach number, $M_T = 0.45$, the performance differences between the configurations, with and without differential pitch are negligible. A slight performance decrease is shown for the differential pitch configurations at the higher tip Mach number. This is consistent with the previously mentioned trend for operation in stall.

In conclusion, it appears that differential collective pitch between blade sets generally has a negligible or slightly detrimental effect on hover performance.

Effect of differential radius. - To determine the effect of differential radius, two additional blade sets with radii 70 and 85 percent of the radius of the reference rotor were tested separately in combination with a blade set of the reference rotor (see Fig. 2). The corresponding radius increment ratios, $\overline{\Delta R}$, of the two resulting rotors and the base rotor are 0.30, 0.15, and 0.0, respectively. As mentioned previously, blade area (cR) was held constant for all blades and, thus, all rotors had the same solidity (based on the total disc area). In addition to radii, the tip speeds of the two blade sets that comprise differential radius configurations obviously differed. When nondimensionalizing the rotor thrust and torque to C_T/σ and C_Q/σ, the radius and tip speed of the reference rotor were used. By using common nondimensionalizing factors for all rotors, the data to be presented are also representative of dimensional thrust and torque for all rotors.

The independent effect of differential radius on hover performance is shown in Fig. 19. Only the radius increment ratio, $\overline{\Delta R}$, was changed relative to the conventional rotor configuration to demonstrate the independent effect of $\overline{\Delta R}$. The tip Mach numbers, M_{T_o}, indicated on the figure are those of the reference blade set. The decrease in thrust and torque at a given collective pitch with increasing radius increment ratio is evident, and is simply attributed to the lower tip speed of the shorter blade set. The performance efficiency improves with increasing $\overline{\Delta R}$ at the low thrust levels. This is due to the decreased profile drag on the shorter blades associated with the

lower tip speed (see data at θ = 0 deg). As thrust level is increased the performance with $\Delta\bar{R}$ deteriorates and drops below the conventional rotor at high thrust levels. This is because that, in order to attain the same thrust level as that of the conventional rotor, the differential radius rotor must operate at a higher collective pitch (1 to 2 deg) to compensate for the loss in thrust due to the lower tip speed of the shorter blades. This causes the differential radius rotor to stall earlier than the conventional rotor which results in a decrease in performance efficiency. The increase in performance at low thrust levels and decrease at high levels will be shown to be characteristic of all differential radius configurations tested.

The effect of differential radius on performance for coplanar blades at azimuth spacings of $\Delta\psi$ = 60, 30, and -30 deg is shown in Fig. 20. In part (a) of this figure most of the data for the same configuration as Fig. 19 has been replotted using an expanded scale to simplify comparison with the other azimuth spacing configurations in parts (b) and (c). The previously noted performance trends for an azimuth spacing of 60 deg are similar for azimuth spacings of 30 and -30 deg. Also, the data for the positive and negative 30 deg azimuth spacing shown in parts (b) and (c) are essentially identical. Thus, the effect of differential radius for a given azimuth spacing appears to be independent of whether the short blades are leading or lagging the reference blades.

The effect of differential radius on the performance of configurations with combinations of axial and azimuth spacing is shown in Fig. 21 for some of the configurations tested. It was found that, except for the $\Delta\bar{z}$ = 1, $\Delta\psi$ = 0 configuration (biplane configuration) where a consistent reduction in performance occurred, the data for a given finite radius increment ratio were independent of axial and azimuth spacing (within a C_T/σ of $\pm$0.001 at a given C_Q/σ). This was found to be true even though the base performance curves in this figure, for rotors with equal length blades, shifted with axial and azimuth spacing as discussed previously. It thus appears that any gains in performance that were previously achieved with axial and azimuth spacing were associated with the fact that the blades were of equal length. This lends credence to the supposition that the performance gains with axial and azimuth spacing are due to the relief of aerodynamic interference effects in the tip region of the equal length blades.

The performance trends on a thrust-torque (or C_T - C_Q) basis, with differential radius are similar to the trends with decreasing solidity (Ref. 1). That is, the observed decrease in profile drag at low thrust levels and the earlier stall at high thrust levels is characteristic of a solidity reduction.

Effect of combining differential radius and differential collective pitch. - The final VGR configuration to be considered consisted of combining differential radius ($\overline{\Delta R} = \pm 0.15$) with differential collective pitch for various axial and azimuth spacings. With but one exception, differential collective pitch was produced by increasing the pitch of the shorter blade set. The intent was to increase the thrust of the shorter blade set to a level closer to that of the larger blade set. The effect of the combined differential radius and differential collective pitch configuration on performance is shown in Fig. 22 relative to identical configurations without differential collective pitch. In part (a), the data for coplanar configurations are presented for two azimuth spacings, $\Delta\psi = 30$ and 60 deg. Performance is shown to increase with increasing pitch on the shorter blades ($\Delta\theta < 0$ for positive $\overline{\Delta R}$ configurations). In part (b), the data for configurations with an axial spacing of one chord length is presented. Data are presented for radius increment ratios, $\overline{\Delta R}$, of 0.15 and -0.15 which correspond to the 85 percent length blades mounted below and above the reference blades, respectively. Consistent with the coplanar rotor results in part (a), increasing the collective pitch on the shorter blade set for configurations with differential radius and axial spacing results in improved performance. This performance gain, relative to the $\Delta\theta = 0$ configuration, is greater with the shorter blades above the longer blades ($\overline{\Delta R} = -0.15$ compared to $\overline{\Delta R} = 0.15$). The greatest performance gain, at the tested thrust level, was measured for the "biplane configuration" ($\overline{\Delta R} = -0.15$, $\overline{\Delta z} = 1$, $\Delta\psi = 0$, $\Delta\theta > 0$) at the higher tip Mach number. The results for the $\Delta\psi = 15$ deg configurations (not shown) were similar to the $\Delta\psi = 0$ results although not quite as extreme. The results for negative azimuth spacings (also not shown) were essentially equivalent to those of similar configurations but with positive spacing. The effect of increasing the collective pitch on the long blades instead of the short blades is shown in part (a) of Fig. 22 (see data for $\Delta\theta = 4$ deg) to be detrimental to performance.

The performance improvement achieved through increasing the pitch on the shorter blades results in delaying the adverse stall behavior of differential radius configurations. In Fig. 23, sample results showing the improved performance at thrust levels near stall and the associated performance benefit over the conventional rotor are presented for one of the configurations of Fig. 22. (The trends observed for this configuration are representative.) The improved performance may be attributable to the following. Since, at the same collective pitch, the longer blades would reach drag divergence earlier due to their higher tip Mach numbers, it is more efficient to increase the pitch separately on the shorter blades to place these blades at a more favorable L/D condition. The effects are relatable to those produced on conventional rotors by redistributing the blade loading inboard with high twist and/or taper. It is thus concluded

that use of the proper differential collective pitch enhances the performance of differential radius configurations by delaying the profile torque rise of the longer blades. However, since the maximum thrust condition was not investigated, the extent of this performance benefit at higher thrust levels remains to be determined.

Discussion of Flow Visualization Results

To gain insight into the aerodynamic environment influencing the hover performance of the variable-geometry rotor configurations, the flow visualization data taken during testing were reduced to determine tip vortex geometry characteristics. Wake coordinates and sample photographs are presented herein for selected configurations. The configurations were selected to demonstrate the characteristic wake features associated with each of the VGR variables and the most promising combinations of these design variables. Presented in this section are wake coordinates for configurations with (1) independent variations of each VGR parameter and (2) combinations of axial and azimuth spacing.

The tip vortex coordinates for the conventional 6-bladed rotor at a collective pitch setting of 10 deg are presented in Fig. 24. A sample photograph of the wake for one rotor position where the azimuth position of blade 1 (ψ_1) is 15 deg is also shown (see Fig. 10 for sequence of photographs at varying ψ). The wake data in Fig. 24 were found to be in excellent agreement with the generalized wake results of Ref. 1 which includes an extensive description of the wake characteristics for conventional hovering rotors and wake data for varying numbers of blades, twist, aspect ratio, thrust level, and tip Mach number. Wake symmetry was assumed in determining the tip vortex coordinates. As described in Ref. 1, the tip vortex for a 6-bladed hovering rotor becomes unsteady between one-half and one revolution from the blade. The extent of the tip vortex coordinate data is thus limited to the near wake region. It is noted, however, that it is the near wake geometry which is of primary significance for performance considerations.

The effect of an independent variation of blade azimuth spacing on tip vortex geometry is shown in Fig. 25. The main wake feature for this configuration is the impingement of the tip vortex of the reference blade (blade 1) on the following blade (blade 2). This impingement is evident in the photograph where blade 2 is just about to enter the plane of the smoke. Reducing the azimuth spacing from the 60 deg of a conventional rotor to 30 deg provides less time for the tip vortex to descend. This coupled with the lower position of the second blade results in the vortex impinging on that

blade. The lower position of the second blade indicates lower coning* and thrust relative to blade 1 which can be attributed to the aerodynamic interference associated with the close proximity of the vortex. For azimuth angles beyond the vortex impingement, a clearly defined vortex core could not be distinguished for the vortex of blade 1 in the flow visualization photographs. The coordinates for the tip vortex from blade 2 were found to be generally similar to those from the conventional blade. The exception is the absence of the abrupt change in axial coordinate which corresponds to the abrupt increase in axial velocity due to the passage of the following blade. This is due to the increased azimuth spacing between blades 2 and 3 (90 versus 60 deg) which results in a greater axial distance between the vortex and the following blade (blade 3).

The effect of independent variations of blade axial spacing is shown in Figs. 26 and 27 for $\Delta\bar{z} = 1$ and 2, respectively. The vortex trajectory from the upper blade (blade 1) passes radially inside the trajectory of the lower blade (blade 2). Near the rotor, the circulation directions of the vortices from the upper and lower blades are such that the vortex from the upper blade is accelerated to a greater downward velocity than the conventional rotor vortex. Likewise, the vortex from the lower blade is decelerated in the vertical direction. As a result, the vortex from the upper blade passes below the vortex from the lower blade. This occurs when the vortices are just below the tip path plane of the lower blade set as indicated by the intersection of the axial coordinate curves in Figs. 26 and 27. A general observation that applies to all configurations is that, when the vortices from two adjacent blades initially reverse their relative axial positions, it occurs at or just below the tip path plane of the lower blade set.

Flow visualization results for configurations with a 30 deg azimuth spacing and various axial spacings are presented in Figs. 28 to 34. These are the configurations which showed significant potential for performance improvement. In Fig. 28, the tip vortex coordinates for an axial spacing, $\Delta\bar{z}$, of one chord length are shown. The movement of the vortices from the

*The axial spacing, $\Delta\bar{z}$, is defined at the hub. It is not exactly representative of axial spacing at the blade tips due to possible differences in coning between blades. The nominal coning angle for the model blades at this condition is approximately 2 deg. A difference in coning and thrust of approximately 20 percent is indicated between blades 1, 3, 5, and 2, 4, 6.

upper and lower blades about one another is evident from the alternate crossings of both the radial and axial coordinate plots. This movement may be clearly observed in photographs showing the time history of the wake (Fig. 29) and in the photograph (Fig. 30) in which the tip vortex cross sections are labeled (A through F) according to the blade from which they were generated. The tip vortex coordinates and the vortex positions relative to the blade are compared to those of the conventional rotor in Figs. 31 and 32 for this axial spacing of 1.0. The primary differences from the tip vortex geometry of a conventional rotor blade are evident in the axial coordinates shown in Fig. 31. In the important region directly behind the blade, ($\psi_w < 180$ deg) the vortex from the upper blade is displaced further from the tip path plane and the vortex from the lower blade is displaced nearer to the tip path plane. This combined with the change in the spatial relationships between blades results in the blade-vortex positions shown in Fig. 32 in comparison with those of a conventional rotor. As will be discussed later in this section, the increased axial distances between the blades and the vortices, particularly for the upper blades (0.08R versus 0.02R), is of importance when considering hover performance. Beyond an axial spacing of 1.5, it was found that the vortex pairs no longer cross each other in the radial direction as shown in Figs. 33 and 34 for axial spacings of 2.0 and 2.5, respectively. As axial spacing is increased for the 30 deg azimuth spacing, the vortex from blade 1 approaches blade 3 on the lower blade set and at a spacing of 2.5 the vortex impinges on the blade (see Fig. 34) at the indicated thrust level ($C_T/\sigma = 0.072$).

The vortex coordinates for the "biplane configurations" ($\Delta\psi = 0$) are of special interest in that they demonstrate an unusual alteration of the vortex pattern at one of the axial spacings tested. In Fig. 35, the coordinates for an axial spacing of one chord length are shown to be similar to those in Fig. 28 for the same axial spacing but an azimuth spacing of 30 deg. That is, the vortex pairs move around one another in a similar manner. However, as shown in Fig. 36 for an axial spacing of 2.0, the vortices do not cross paths. At ψ_{w_1} = 120 to 150 deg, the crossing in the axial direction is abruptly prevented by the influence of the bound and tip vortex from blade 4 on the vortex of blade 2.

The flow visualization results for the differential collective pitch configurations were the most difficult to analyze. For some of these configurations portions of the near wake appeared to be unsteady, and it was difficult to accurately track the vortex locations with an acceptable degree of confidence. For this reason the tip vortex coordinates showing the effect of an independent collective pitch variation from the conventional rotor are not included herein. However, the coordinates for a 30 deg azimuth spacing configuration with a differential collective pitch of 2 deg are presented in

Fig. 37. It appears that the close passage of the vortex from blade 1 to blade 2 results in a decreased thrust level and coning angle for blade 2 as indicated by the lower axial position of its tip. It is also observed that the two vortices from blades 1 and 2 remain close together which results in considerable interaction.

The independent effect of differential radius on tip vortex geometry is shown in Figs. 38 and 39 for radius increment ratios of 0.15 and 0.3. The axial spacing shown between alternate blade tips is due to differences in the vertical tip positions with coning for unequal blade lengths and differences in coning angle between the long and short blades for unequal Lock numbers. Unlike the other VGR variables, differential radius does not singly result in pronounced distortions of the tip vortex trajectories -- at least for the relatively large radius increment ratios tested.

Sample flow visualization photographs for other variable-geometry rotor configurations are presented in Fig. 40.

Descriptions are given in Refs. 1 and 2 of the effects of tip vortex positions on hover performance. It is concluded therein that changes in hover performance may be directly related to changes in wake geometry. Of particular significance are the relative positions between the blades and the initial tip vortices that pass beneath the blades. In an attempt to determine if there is any obvious correlation between performance trends and wake geometry trends for the variable-geometry rotors, the tip vortex coordinate variation with axial spacing was plotted for VGR configurations with an azimuth spacing of 30 deg. This set of configurations was selected because it demonstrated a significant performance increase with increased axial spacing. The variation with $\overline{\Delta z}$ of the axial and radial coordinates for the points on the tip vortices which are directly beneath an upper and lower blade (blade-vortex intersections) is shown in Fig. 41. The axial coordinates, $\bar{z}_T$, represent the vertical distances from each vortex to the tip of a single upper or lower blade, as noted. The coordinates for the conventional rotor are also shown for comparison. The age of each vortex is indicated by ψ_w. The ψ_w values may be used in identifying the blade which shed each vortex if it is recognized that ψ_w is equivalent to the azimuth interval between the blade which shed the vortex and the selected upper or lower blade in Fig. 41. For the zero axial spacing configuration, coordinates of vortex points shed from the upper blade for ψ_w values of 120, 150, 240, and 270 deg are not shown because, as previously mentioned, they were indistinguishable after the vortex impingement.

For the lower blade, no obvious reason for a performance increase with axial spacing is evident from the vortex coordinate trends. Some vortices move away from the blade while others move closer. However, for the upper blade, the minimum axial distance between the blade and vortex is increased by more than a factor of three relative to the distance for the conventional rotor. This is more clearly indicated in Fig. 42 where the coordinates in Fig. 41 have been cross-plotted to provide a pictorial view of the movement of the tip vortex positions with axial spacing variations*. The increased distance between the near vortex and the upper blade could result in the relief of vortex induced stall at the blade tip which is produced by the strong upflow just outboard of the vortex, as described in Refs. 1 and 2. Thus an increase in performance at the high thrust levels could result for the three upper blades. The relationship between performance and vortex position for the three lower blades is difficult to interpret. Although the vortex from the preceding blade moves further above the blade with increased axial spacing, the vortices from the previous blade pair move closer to the blade. In fact, as shown previously in Fig. 34, a near vortex impingement occurs for $\Delta\bar{z} = 2.5$. However, the close position of this vortex may not be as severe for this configuration as for the conventional rotor because of (1) its occurrence on only three of the six blades, (2) the reduced possibility of inducing tip stall due to its more inboard radial position ($\bar{r} = 0.88$ versus 0.94) at which the Mach number and local angle of attack are normally lower, and (3) the counteracting inflow effect of the tip vortex outboard of the impinging vortex. It thus appears that a net gain in performance for configurations with axial and azimuth spacing is due to a net improvement in the vortex orientation for the upper blades and a compensating vortex orientation for the lower blades. However, the extreme complexity of the vortex system makes it difficult to conclude this without an extensive analytical study of the entire rotor-wake system**.

---

*The two pictorial views in Fig. 42 are views of the tip vortex cross sections in the planes of the upper and lower blades which are similar to the view in a smoke photograph when a blade is in the plane of the smoke. To illustrate this, the labelled vortex cross sections (A through F) in the photograph in Fig. 30, where the lower blade is in the plane of the smoke, are indicated in Fig. 42 (b).

**The possibility that the performance benefit with axial spacing is due to some phenomenon unrelated to tip vortex interference is also recognized. For example, it may be that the general downwash pattern across the blades is favorably altered when axial spacing is introduced, or that the lower rotor, by virtue of axial location, produces an increase in effective disc area thereby providing improvements associated with lower disc loading.

WIND TUNNEL TEST OF VARIABLE-GEOMETRY ROTORS

Several of the model variable-geometry rotor configurations were selected for an exploratory wind tunnel test to compare the performance, vibrations, and flapping response of variable-geometry rotors with a conventional rotor.

Test Equipment

The wind tunnel test program was conducted in the UARL 4 x 6 ft subsonic wind tunnel (Fig. 43) which has a closed circuit and operates at a maximum test section velocity of 110 mph. Static pressure in the irregular octagonal test section is atmospheric. The same rotor test rig, rotor hubs, and blades used in the hover test were used in the wind tunnel test. Photographs of a conventional and variable-geometry rotor mounted in the wind tunnel are presented in Fig. 44. Rotor thrust, torque, and longitudinal force were measured by means of strain-gaged load cells or bending beams. A provision for varying rotor shaft angle between ± 12 deg was available. Cyclic pitch control was not provided and collective pitch was set manually. Longitudinal and lateral vibration amplitudes were measured on the rotor shaft using conventional vibration pickups. Blade flapping was measured through the deflection of strain-gaged bending beams mounted on the hubs and wired to a slip ring-visicorder system which provided direct read-out of the flapping time history.

Test Configurations and Operating Conditions

The wind tunnel test was limited in scope to an exploratory test of a few variable-geometry rotor configurations. A configuration with axial spacing of one chord length and an azimuth spacing of 30 deg was selected as the base variable-geometry rotor configuration on the basis of the potential performance advantage demonstrated in the hover test. Two azimuth spacing variations (60 and -30 deg) and the reference conventional rotor made up the other primary configurations. A greater axial spacing ($\overline{\Delta z} = 2.0$) was selected as one of the secondary configurations along with configurations including differential radius and differential collective pitch. An attempt to test a biplane configuration ($\overline{\Delta z} = 1.0$, $\Delta\psi = 0$) was terminated due to blade contact occurring in forward flight. Whereas, the primary configurations were tested over an extensive range of advance ratio, collective pitch, and shaft angle, only a minimal amount of data were obtained for the secondary configurations. The test configurations and control settings are listed in Table VI. Generally, each test configuration was tested at a tip

speed of 91.4 m/sec (300 fps), advance ratios of 0.1, 0.2, 0.3, 0.4, and 0.47, and at shaft angle increments of 2 deg. Tip speeds above 91.4 m/sec and certain high advance ratio,high lift conditions were not tested due to blade edgewise stress limits. These limits were associated with the absence of lag hinges in the model and not with any characteristic of the variable-geometry rotors.

TABLE VI

TEST CONFIGURATIONS AND CONTROL SETTINGS
VARIABLE-GEOMETRY ROTOR WIND TUNNEL TEST

Rotor Configuration	Collective Pitch, θ, deg	Shaft Angle Range α_s, deg
Conventional Rotor $\overline{\Delta R} = 0$, $\overline{\Delta z} = 0$, $\Delta\theta = 0$, $\Delta\psi = 60$	0 3 6 9 12	0 to 12 -6 to 6 -12 to 0 -12 to 0 -12 to -4
Variable-Geometry Rotor $\overline{\Delta R} = 0$, $\overline{\Delta z} = 1.0$, $\Delta\theta = 0$, $\Delta\psi = 30$	3 6 9	-8 to 8 -12 to 0 -12 to 0
Variable-Geometry Rotor $\overline{\Delta R} = 0$, $\overline{\Delta z} = 1.0$, $\Delta\theta = 0$, $\Delta\psi = 60$	3 6 9	-6 to 6 -10 to 0 -12 to 0
Variable-Geometry Rotor $\overline{\Delta R} = 0$, $\overline{\Delta z} = 1.0$, $\Delta\theta = 0$, $\Delta\psi = -30$	3 6 9	-6 to 6 -10 to 0 -12 to 0
Variable-Geometry Rotor $\overline{\Delta R} = 0$, $\overline{\Delta z} = 1$, $\Delta\theta = 0$, $\Delta\psi = 0$	6	0
Variable-Geometry Rotor $\overline{\Delta R} = 0$, $\overline{\Delta z} = 2.0$, $\Delta\theta = 0$, $\Delta\psi = 30$	9	-10 to 0
Variable-Geometry Rotor $\overline{\Delta R} = 0$, $\overline{\Delta z} = 1.0$, $\Delta\theta = -1$, $\Delta\psi = 30$	$\theta_{(1)} = 9$ $\theta_{(2)} = 10$	-10 to 0
Variable-Geometry Rotor $\overline{\Delta R} = 0.15$, $\overline{\Delta z} = 1.0$, $\Delta\theta = 0$, $\Delta\psi = 30$	9	-10 to 0

Test Procedures, Data Reduction, and Accuracy

The test procedure consisted of mounting the desired rotor configuration, setting the collective pitch and shaft angle, and varying the tunnel air speed to attain the required advance ratios. Recorded data consisted of rotor thrust, longitudinal force, torque, blade flapping, and rotor shaft vibration levels. The rotor performance data were transformed to coefficient form, C_L/σ, C_D/σ, and C_Q/σ. In order to eliminate the influence of the non-scaled hubs and shaft, tares representing the lift, drag, and torque of the isolated hubs and shaft were measured and removed from the data. Peak-to-peak blade flapping and vibration amplitudes were analyzed to determine the influence of the various rotor configurations on blade response and rotor vibration levels. The estimated accuracy of the data is shown in Table VII.

TABLE VII

ESTIMATED ACCURACY OF WIND TUNNEL DATA

Lift coefficient/solidity, C_L/σ	± 0.002
Drag coefficient/solidity, C_D/σ	± 0.001
Torque coefficient/solidity, C_Q/σ . . .	± 0.0002
Blade flapping amplitude, β_{PTP}, deg. . .	± 0.3
Relative vibration amplitude, cm (in.)..	± 0.12 (± 0.005)

Discussion of Wind Tunnel Results

Performance characteristics. - Sample comparisons of the forward flight performance characteristics of one of the variable-geometry rotors versus a conventional rotor configuration are presented in Fig. 45, parts (a) and (b) for advance ratios of 0.1 and 0.3. As mentioned above, the rotor configuration shown ($\overline{\Delta R} = 0$, $\overline{\Delta z} = 1$, $\Delta\psi = 30$ deg, $\Delta\theta = 0$) was selected as the base configuration for the wind tunnel test because of its improved hover performance. Rotor lift, drag, and torque coefficients nondimensionalized by rotor solidity are plotted versus rotor shaft angle for three collective pitch values. The performance results are shown to be generally equivalent for the two rotors. In Fig. 45, part (c), a performance comparison over the advance ratio range tested is shown for three representative operating

conditions consisting of three different combinations of collective pitch and shaft angle. Again, the performance of the two rotors is shown to be generally equivalent. A performance comparison between other primary rotor configurations which have to other azimuth spacings ($\Delta\psi$ = 60 and -30 deg) and the conventional rotor indicated similar results. This was also true for the limited amount of data obtained for the configuration with an axial spacing of two chord lengths as shown in Fig. 46. It is thus concluded that, with the exception of slight differences for a few isolated conditions, variations of blade azimuth spacing and axial spacing have a negligible effect on integrated forward flight performance. Considering these wind tunnel results together with those of the hover test, it appears that variable-geometry rotor configurations with axial and azimuth spacing can offer improved hover performance without adversely affecting forward flight performance.

The influence on forward flight performance of differential collective pitch and differential radius as variations from the base variable-geometry rotor is shown in Figs. 47 and 48. Based on the limited wind tunnel data obtained for these secondary configurations, the following performance trends are indicated. Increasing the pitch on the three blades of the lower blade set reduced forward flight performance for conditions near stall as indicated in Fig. 47 by the decrease in rotor lift curve slope and increase in rotor drag and torque slopes relative to the base configuration*. As anticipated, the lift and torque of the differential radius configuration decreased relative to that of the base configuration for the same collective pitch setting as shown in Fig. 48. The decrease due to the shorter length blades corresponds to an approximate one degree decrease in pitch on the base configuration and is consistent with the hover results discussed previously.

Vibration characteristics. - The shaft vibration data were analyzed to determine the influence of the variable-geometry rotor configurations on vibration levels. The vibration data were obtained from vibration meters mounted to the rotor shaft and oriented to measure the peak-to-peak amplitude in the longitudinal and lateral directions in a plane normal to the shaft. The vibrations of the various rotor configurations were compared at similar operating conditions. A comparison of the rotors with an axial spacing of one chord length and varying azimuth increments indicated that, at least below stall, there is no significant effect of azimuth spacing between the upper and lower blades on vibrations. Based on a limited amount

*This trend was also observed from the data at other advance ratios.

of data, this was also found to be true for independent variations of (1) axial spacing from one to two chord lengths and (2) differential collective pitch (one deg) between alternate blades. The vibrations of the configurations with axial spacing (dual hub rotors) were of the same order of magnitude as those of the conventional coplanar rotor; however, direct comparisons between rotors were not believed to be meaningful because of the different hub mass characteristics. As anticipated, vibrations increased substantially for stalled conditions. Excessive vibration, which prohibited testing at and above an advance ratio of 0.3, were produced by the differential radius configuration. For example, the rotor with $\overline{\Delta R} = 0.15$ produced peak vibrations approximately 3 times higher than the rotor with $\overline{\Delta R} = 0$ at an advance ratio of 0.3.

Flapping characteristics. - Sample comparisons of the flapping angle variation with azimuth position for a variable-geometry rotor ($\overline{\Delta R} = 0$, $\overline{\Delta z} = 1$, $\Delta\psi = 30$ deg, $\Delta\theta = 0$) and a conventional rotor are presented in Fig. 49 for two test conditions. The mean flapping angle (coning angle) has been removed to directly compare the harmonic content of flapping. The flapping is essentially first harmonic fore-and-aft, typical of hinged blades without cyclic pitch. Flapping is shown with respect to the azimuth angle of the upper blade ($\psi_{(1)}$). The phase shift between the flapping peaks of the upper and lower blades corresponds closely to the built-in azimuth spacing of 30 deg.

The blade flapping amplitudes measured for the various rotor configurations are presented in Fig. 50 at selected advance ratios. The peak-to-peak flapping angles associated with each control setting (θ,α_s) are listed separately for each blade set ($\beta_{PTP(1)}$ and $\beta_{PTP(2)}$) of the variable-geometry rotor configurations, and the conventional rotor flapping amplitudes are included for comparison. It is recognized that the absolute values of the flapping amplitudes are not representative of typical full-scale rotors due to the absence of cyclic pitch and appropriate scaling. However, the data were taken to observe relative differences between rotor configurations for use as an indicator of wake interference effects. Comparing the flapping amplitudes at similar control settings indicates that flapping varies between blade sets within a configuration as well as between configurations. This is true even for the configurations which include only axial and azimuth spacing for which performance variations were negligible. The difference in flapping amplitude between the upper and lower blades at a given pitch setting generally increases with thrust level (or shaft angle). An interesting reversal from the upper blade having the higher amplitude to the lower blade having the higher amplitude is shown in Fig. 50, part (a), for a variation of azimuth spacing from 30 to 60 deg. For example, at the highest lift tested ($C_L/\sigma = 0.10$), the peak-to-peak flapping of the upper blades of the configuration with an azimuth spacing of 30 deg is higher by

1.8 deg (β_{PTP} = 17.0 versus 15.2 deg). Conversely, for the 60 deg configuration, the peak-to-peak flapping of the upper blades is lower by 1.7 deg (β_{PTP} = 14.8 versus 16.5 deg). It thus appears that, although the integrated performance (lift, drag, and torque) is essentially unchanged by axial and azimuth spacing, these inter-blade spacing variables do result in blade response variations. It is recognized that some variations in flapping could be produced by aerodynamic interference effects from the model drive shaft which may influence one blade set or configuration more than the other; however, it is expected that the primary variations in flapping are caused by differences in blade-vortex interference effects associated with variations in wake geometry.

HOVER TEST OF MODEL ROTOR BLADES WITH OGEE TIPS

Conventional, coplanar model rotors with blades having an ogee tip design were hover tested as part of this investigation. The ogee tip shape, shown in Fig. 51, as conceived at the NASA Langley Research Center, evolved from exploratory, small-scale, smoke tunnel tests which were directed toward reducing the intensity of the tip vortex during its formation by suitable tip-shape modifications.

The conceptual basis of the ogee tip, as stated in Ref. 8, is as follows. "The shape is based upon a concept of a two stage tip vortex formation mechanism, which results from the three-dimensionality of the flow field. The primary vortex is formed along the streamwise edge of a rectangular wing tip - much like a delta wing leading edge vortex. This separation vortex forms an intense core and as it passes off the tip trailing edge the wing shed vortex sheet is entrained and concentrated into a combined tip vortex system. The separation vortex mechanism is not essential to the overall lifting system. The ogee tip shape is designed to eliminate the separation vortex. This is achieved by cutting back the tip streamwise edge, starting at the leading edge, at an angle sufficient to assure that the local flow swirl angle cannot produce a reattachment of the flow coming from beneath the tip on the upper surface. The cutback angle gradually decreases toward the wing trailing edge, due to a drop-off in differential pressure and the associated swirl angle. The tip edge is faired smoothly into the wing trailing edge to avoid a sharp discontinuity in local flow." Essentially, this tip shape change decreases the steep gradient in the local lift distribution in the tip region, and prevents the formation of a separation vortex.

Model blades with interchangeable epoxy-plastic tip sections, shown in Fig. 52, were used to conduct an exploratory tip design test. Carbon fibers were inserted in the ogee tip sections to increase their structural strength. Blades with the NASA ogee and rectangular tip sections were hover tested. The blades were similar to the reference radius blades (R = 27.5 in.) of the variable-geometry rotor test except for twist and the provision for mounting varying tip sections. Both tip sections were tested on 3- and 6-bladed rotors at three tip speeds and several collective pitch settings. The tests were conducted at the same hover test facility described earlier for the variable-geometry rotor hover test. The nominal model blade characteristics and rotor operating conditions are listed in Table VIII.

TABLE VIII

NOMINAL MODEL BLADE CHARACTERISTICS AND ROTOR OPERATING CONDITIONS -- OGEE TIP DESIGN TEST

Linear twist, deg.	-8
Radius, R, cm (in.).	69.9 (27.5)
Chord, c, cm (in.)	3.73 (1.47)
Airfoil section.	NACA 0012
Number of blades, b.	3, 6
Tip speeds, ΩR, m/sec (fps).	107 (350), 160 (525), 183 (600)
Tip Mach numbers, M_T	0.31, 0.47, 0.54
Collective pitch settings, θ, deg. .	0, 6, 8, 10, 11, 11.5 (or 12)

The maximum tip Mach number was limited to 0.54 to avoid possible fracture of the extreme end of the model ogee tip section. The hover performance results for the ogee tip are compared in Fig. 53 with the rectangular tip data. The data accuracy varies with tip Mach number as estimated in Table IX. At low thrust levels, the ogee tip performance is equivalent to that of the rectangular tip for a 3-bladed rotor. A small performance improvement, which borders on the range of the experimental accuracy, is shown for the 6-bladed ogee tip rotor. The model ogee tip stalls earlier than the rectangular tip resulting in performance degradation at high thrust levels Ogee tip data were not acquired for the 3-bladed rotor at a tip Mach number

TABLE IX

ESTIMATED PERFORMANCE DATA ACCURACY -- TIP DESIGN TEST

Performance Parameter	Tip Mach Number		
	$M_T = 0.31$	$M_T = 0.47$	$M_T = 0.54$
Thrust coefficient/solidity, C_T/σ	0.0007	0.0004	0.0004
Torque coefficient/solidity, C_Q/σ	0.00013	0.00007	0.00004

of 0.54 due to a structural failure of a tip. However, the stall trend is clearly established from the data at the other tip Mach numbers and for six blades.

A question arises as to the proper solidity ratio to use when comparing the performance data of the two rotors. In Fig. 53, a constant solidity ($\sigma = 0.102$) based on the nominal chord and radius noted in Table VII was used. Thus the comparison in Fig. 53 is similar to a comparison of the performance on a thrust versus torque basis. Comparison of the performance data on this basis is of interest to the designer who is constrained to a fixed rotor radius and a nominal chord and desires the maximum thrust-torque ratio from his rotor. However, this form of comparison does not account for the reduction in solidity of the ogee tip which a portion of the performance degradation can be attributed to. For performance based on a solidity value which accounts for the blade area removed in the tip region ($\sigma = 0.0964$), the C_T/σ and C_Q/σ values of the ogee tip rotor in Fig. 53 should be multiplied by 1.04. Alternately, using weighted solidity ratios which emphasize the importance of the blade outboard region, C_T/σ and C_Q/σ values of the ogee tip rotor in Fig. 53 should be multiplied by 1.13 and 1.16, respectively. Based on weighted solidity ratios the performance curves of the ogee tip rotor are closer to those of the rectangular rotor than is shown in Fig. 53. However, a performance degradation still exists in the stall region. A portion of the performance degradation of the ogee tip may be attributed to a change in airfoil efficiency arising from the reduction in Reynolds number with decreasing tip chord and the departure of the airfoil section from a NACA 0012 section to an elliptical section at the tip. Although these results demonstrate the performance trends for model rotors employing the ogee tip, they may not be conclusive for full-scale rotors due to the Reynolds number influences. The difference in the tip Reynolds number range of the rectangular and ogee tip sections between the model blade and a typical full-scale blade is shown in Table X. Considering the significant differences in the airfoil characteristics for the above Reynolds numbers, the model rotor performance results should be considered as only a preliminary evaluation of the ogee

TABLE X

SCALING PARAMETERS FOR THE OGEE AND RECTANGULAR TIPS

Scaling Parameter	Model Blade (M_T = 0.47)		Full-Scale Blade	
	Rectangular	Ogee	Rectangular	Ogee
Chord at tip, cm (in.)	3.73 (1.47)	0.15 (0.06)	45.7 (18)	1.78 (0.7)
Reynolds number at blade tip (approx.)	400,000	16,000	6,000,000	250,000

tip, and full-scale rotor testing is recommended. The desirability of full-scale rotor testing of the ogee tip is reinforced by the inconsistency of other experimental performance results from recent model wing section and model propeller tests (Refs. 8 and 9). In Ref. 8, the lift to drag ratio of the ogee tip wing at full-scale Reynolds number, before stall onset, was reported to be improved over the rectangular tip wing by about five percent, whereas, in Ref. 9, a performance decrease of ten to sixteen percent is noted for the ogee tip adapted to a highly twisted model propeller.

Flow visualization photographs and movies were taken during the tip test using smoke and schlieren movie techniques. Sample smoke photographs for the ogee and rectangular tips are shown in Fig. 54. In contrast to the rectangular tip data, the smoke flow visualization data for the ogee tip showed that the tip vortices were more diffused. The schlieren results showed that the rectangular tip produced strong concentrated vortices, but the tip vortices of the ogee tipped blades were barely visible. This indicates that the ogee tip design reduces the concentration of the tip vortex over that produced by a rectangular tip.

These flow visualization results are consistent with the results of Refs. 8, 9, and 10 which also show that the concentration mechanism associated with the interaction of the intense core of the separation vortex and the trailing vortex sheet is no longer present. In Ref. 9, a model propeller with ogee tips is shown to produce a very small concentrated vortex from the extreme tip, and a large diffuse swirling mass behind the central region of the tip. From the fixed wing vortex measurements of Ref. 8, it was reported that the core diameter from the ogee tip was weakly defined and estimated to be substantially larger (two to five times) than that from the rectangular tip, and the maximum tangential velocities in the vortex core are reduced below those of a rectangular tip by a factor of four. The data also show that significantly more time is required for the vortex formed by the ogee tip to roll up completely and develop its

maximum tangential velocity. It was reported that the vortex formation process is more similar to the roll up of a trailing vortex sheet than the formation of a conventional tip vortex.

Thus, all model results to date, both rotating and nonrotating, indicate that the elimination of the separation vortex mechanism, which was the goal of the ogee tip design, was substantially achieved. It should be noted, however, that the ogee tips reduced model scale rotor performance as reported herein, and thus the impact of the aerodynamic phenomenon produced by this tip shape on full-scale rotor performance should be established.

CONCLUSIONS AND RECOMMENDATIONS

The following conclusions apply to the 6-bladed variable-geometry rotor and ogee tip configurations as tested in this investigation at model scale.

1. Axial spacing of alternate blades offers a significant hover performance advantage relative to a conventional rotor configuration at thrust levels near stall. This performance advantage generally becomes greater with increased axial spacing, thrust level, and tip Mach number.

2. Combining the proper azimuth spacing with axial spacing offers an additional hover performance improvement. The extent of this added improvement is lessened as the axial spacing is increased from one to two chord lengths.

3. Varying the azimuth spacing independently from the 60 deg spacing of the conventional coplanar rotor does not improve hover performance.

4. Differential collective pitch for rotors having equal length blades generally has a negligible or detrimental effect on hover performance.

5. Differential radius offers improved performance at low thrust levels, but this advantage is compromised by the lower thrust capability attributed to earlier stall. The performance degradation associated with this premature stall can be delayed by increasing the collective pitch of the short blades relative to the long blades.

6. The tip vortex patterns of variable-geometry rotor configurations are much more complex than those of conventional rotors. The relation between these complex vortex patterns and the measured hover performance trends are difficult to interpret without an extensive analytical study

of the entire rotor-wake system. However, from consideration of the tip vortex geometry and the associated blade-vortex interference effects for rotors with axial spacing, it appears that the measured performance gain of such rotors may be due to a net improvement in the vortex orientation relative to the individual blades. In particular, the improved performance at high thrust levels may be associated with induced stall relief on the upper blades provided by the tip vortex reorientation.

7. Variations of rotor axial and azimuth spacing generally have a negligible effect on integrated forward flight performance.

8. Differences in blade flapping amplitudes of variable-geometry rotor configurations in forward flight imply differences in aerodynamic interference effects which may be attributable to variations in wake geometry.

9. No pronounced vibration problems were evident in forward flight for constant radii configurations; however vibration levels of the differential radius configurations tested became excessive at advance ratios of 0.3 and above.

10. Flow visualization results indicate that the ogee tip design influences the tip vortex formation mechanism and succeeds in reducing the concentration of the tip vortex. However, the ogee tips reduce model scale hover performance. The impact of the aerodynamic phenomenon produced by the ogee tip on full-scale performance remains to be established.

The implications of Reynolds number effects when applying these conclusions to full-scale rotors is well recognized, particularly since the significant performance gains achieved with the model variable-geometry rotors were at thrust levels near stall. It is also recognized that other means of achieving hover performance improvements are available through refinements in blade design (e.g., twist, camber, and planform variations). However with performance improvements up to 7 percent measured for the model scale rotors and further gains indicated by the data trends, investigation of variable-geometry configurations for full-scale rotors appears warranted. It is thus recommended that the results of this exploratory investigation be used to select certain rotor configurations for full-scale testing to substantiate the model rotor trends and to establish the merit of variable-geometry rotor configurations in relation to other improved design concepts. Also, tests of 4-bladed variable-geometry configurations and an investigation of the possible beneficial influence of variable-geometry rotor configurations on blade response and noise characteristics are recommended. Finally, it is recommended that analytical methods be developed to predict variable geometry-rotor performance and blade response characteristics.

REFERENCES

1. Landgrebe, A. J., An Analytical and Experimental Investigation of Helicopter Rotor Hover Performance and Wake Geometry Characteristics, USAAMRDL Technical Report 71-24, Eustis Directorate, U. S. Army Air Mobility Research & Development Laboratory, Fort Eustis, Va., June 1971.

2. Landgrebe, A. J., The Wake Geometry of a Hovering Helicopter Rotor and Its Influence on Rotor Performance, Journal of the American Helicopter Society, Vol. 17, No. 4, October 1972, pp. 3-15.

3. Bellinger, E. D., Experimental Investigation of Effects of Blade Section Camber and Planform Taper on Rotor Hover Performance, USAAMRDL Technical Report 72-4, Eustis Directorate, U. S. Army Air Mobility Research & Development Laboratory, Fort Eustis, Va., March 1972.

4. Landgrebe, A. J., and Cheney, M. C., Rotor Wakes - Key to Performance Prediction, American Helicopter Society Midest Region Symposium on the Status of Testing and Modeling Techniques for V/STOL Aircraft, October 1972.

5. Landgrebe, A. J., An Analytical Method for Predicting Rotor Wake Geometry, Journal of American Helicopter Society, Vol. 14, No. 4, October 1969, pp. 30-32.

6. Bellinger, E. D., Analytical Investigation of the Effects of Blade Flexibility, Unsteady Aerodynamics, and Variable Inflow on Helicopter Rotor Stall Characteristics, NASA CR-1769, September 1971.

7. Landgrebe, A. J. and Bellinger, E. D., An Investigation of the Quantitative Applicability of Model Helicopter Rotor Wake Patterns Obtained from a Water Tunnel, USAAMRDL Technical Report 71-69, Eustis Directorate, U. S. Army Air Mobility Research & Development Laboratory, Fort Eustis, Va., December 1971.

8. Rorke, J. B., Moffitt, R. C., and Ward, J. F., Wind Tunnel Simulation of Full Scale Vortices, Preprint No. 623, 28th Annual National Forum of the American Helicopter Society, May 1972.

9. Walters, R. E. and Skujins, O., A Schlieren Technique Applied to Rotor Wake Studies, American Helicopter Society Mideast Regional Symposium on the Status of Testing and Modeling Techniques for V/STOL Aircraft, October 1972.

10. Ward, J. F. and Young, W. H., Jr., A Summary of Current Research in Rotor Unsteady Aerodynamics With Emphasis on Work at Langley Research Center, Specialists Meeting on the Aerodynamics of Rotary Wings, AGARD Fluid Dynamics Panel, October 1972.

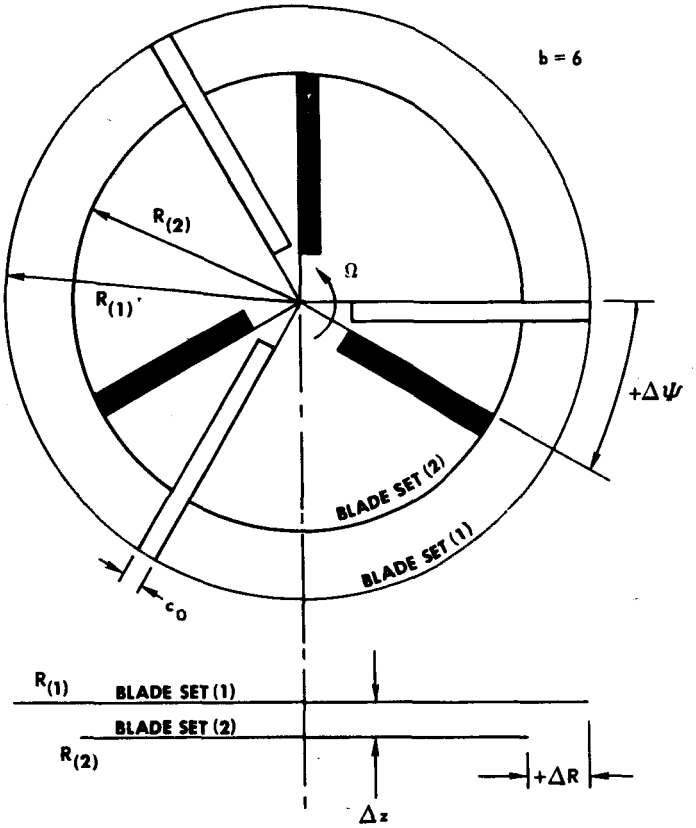

NOTATION

b	Number of blades in rotor
$R_{(1)}, R_{(2)}$	Radii of blade sets (1) and (2)
ΔR	Radius difference between blade sets (1) and (2), $R_{(1)} - R_{(2)}$
R_0	Reference blade radius (largest radius)
$z_{(1)}, z_{(2)}$	Axial coordinates of upper and lower blade sets (1) and (2)
Δz	Axial spacing between upper and lower blade sets, $z_{(1)} - z_{(2)}$
c_0	Reference blade chord (chord of largest radius blade)
$\Delta\psi$	Azimuth increment of blade set (1) relative to blade set (2), $\psi_{(1)} - \psi_{(2)}$
$\theta_{(1)}, \theta_{(2)}$	Collective pitch angles on blade sets (1) and (2)
$\Delta\theta$	Collective pitch angle increment between blade sets (1) and (2), $\theta_{(1)} - \theta_{(2)}$
θ	Nominal collective pitch value (mean pitch value for configurations with $\Delta\theta \neq 0$)
$\overline{\Delta R}$	Radius increment ratio, $\Delta R/R_0$
$\overline{\Delta z}$	Vertical spacing ratio, $\Delta z/c_0$

Except for coplanar blade sets: (1) = upper blade set, (2) = lower blade set.
For coplanar blades: (1) = larger blade set, (2) = smaller blade set.

Figure 1. - Schematic of Variable-Geometry Rotor and Notation.

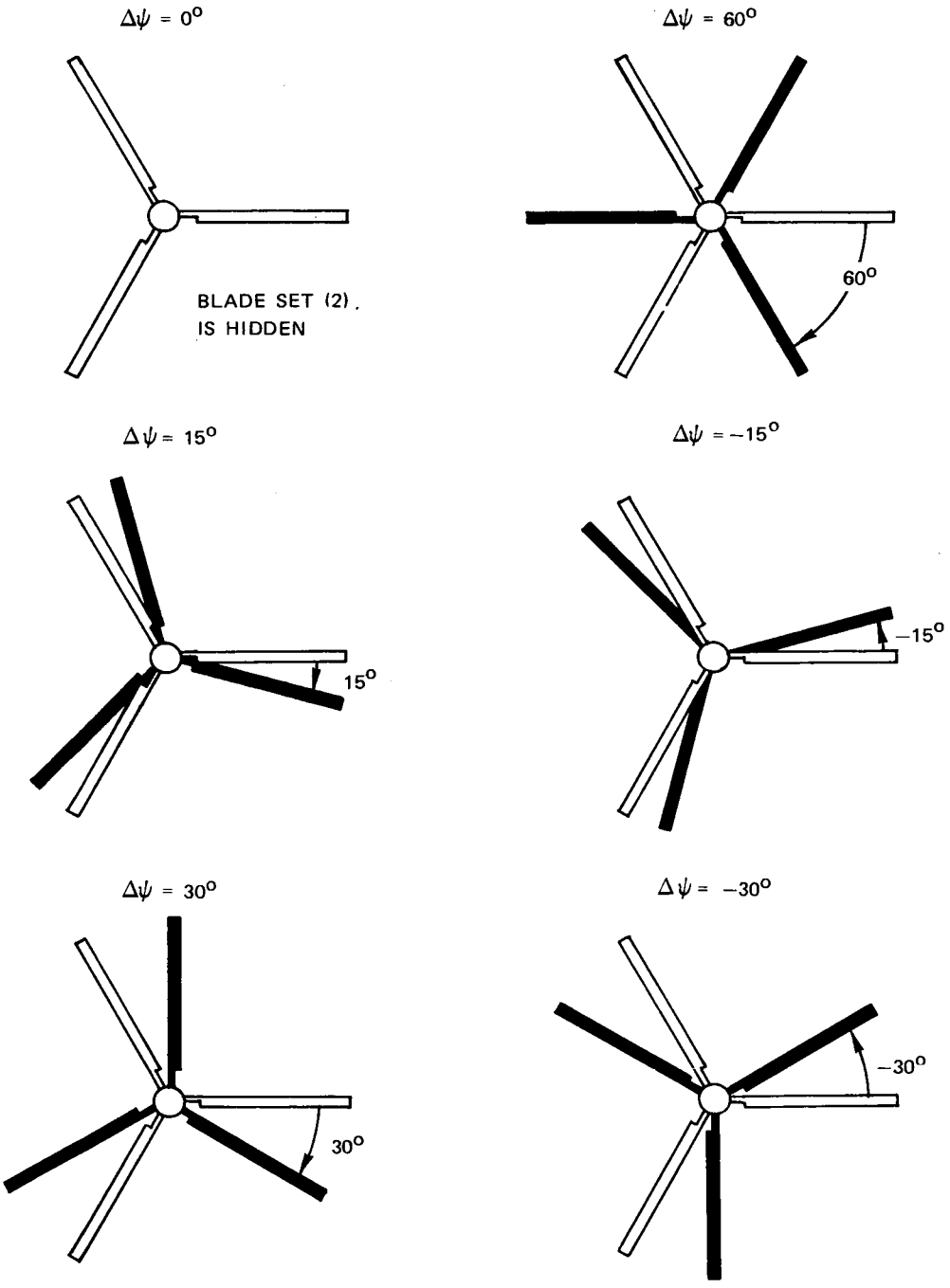

(a) - Azimuth Spacings.

Figure 2. - Variable-Geometry Rotor Configurations.

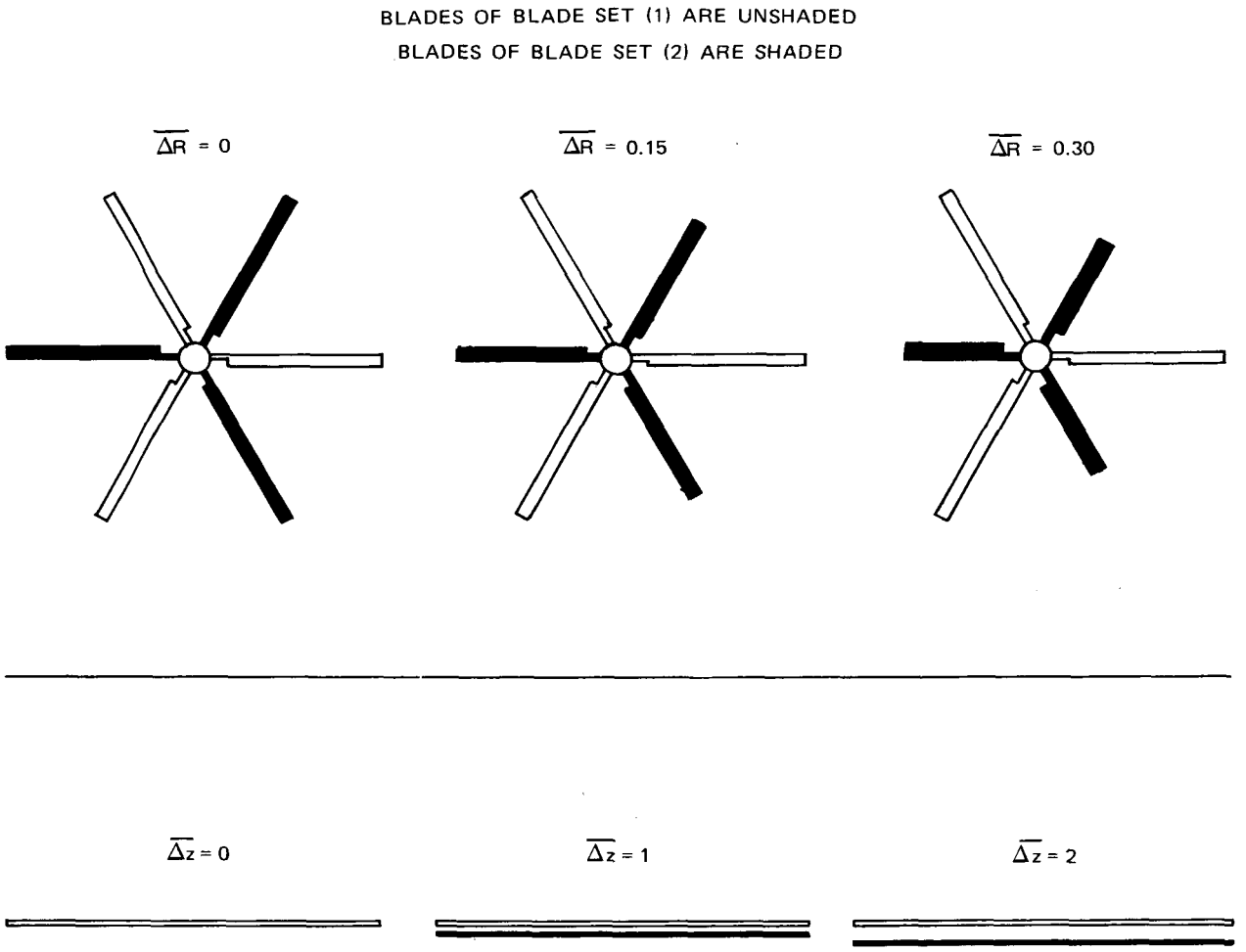

(b) - Radius Increment Ratios and Axial Spacings.

Figure 2. - Concluded.

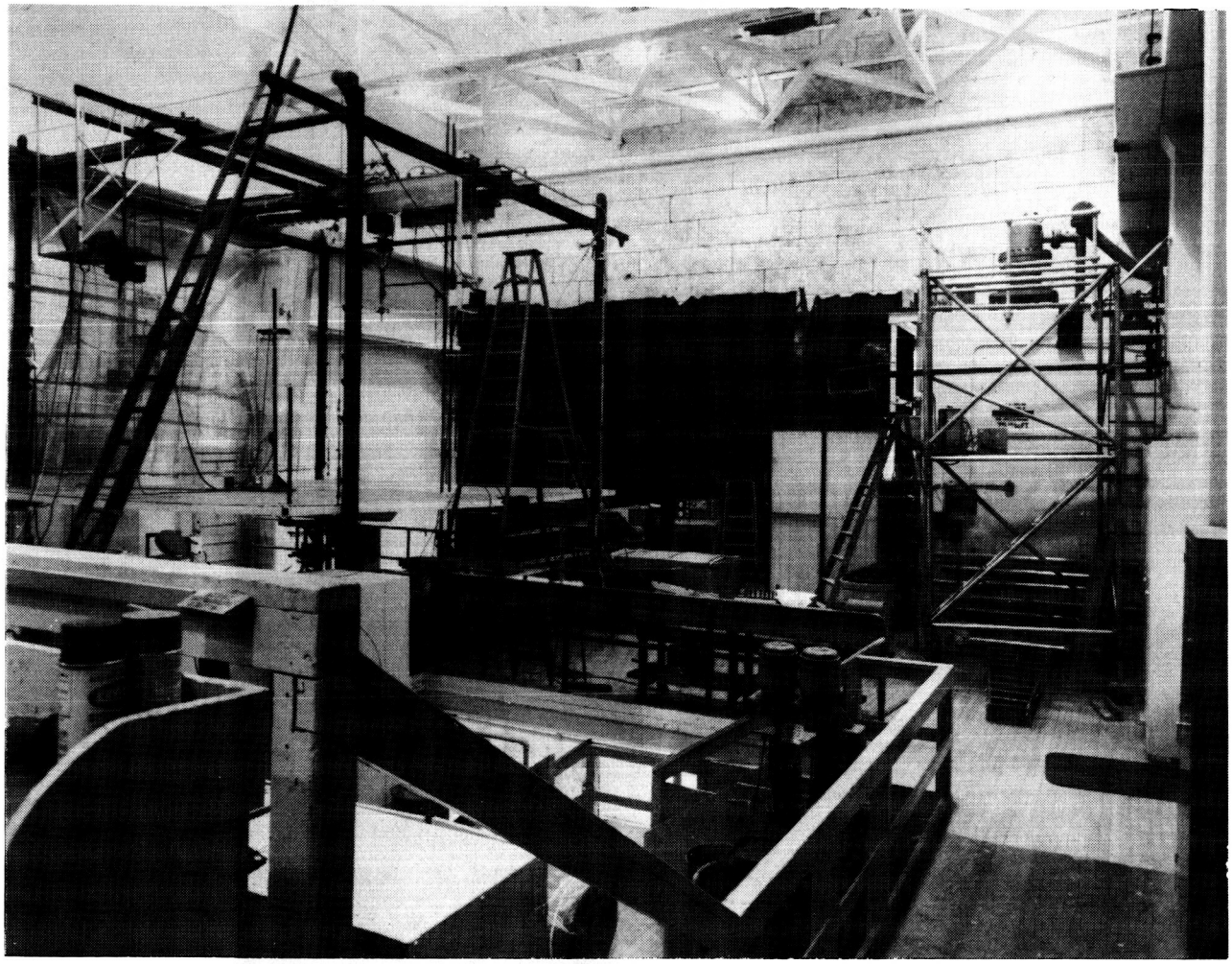

Figure 3. - UARL Model Rotor Hover Test Facility.

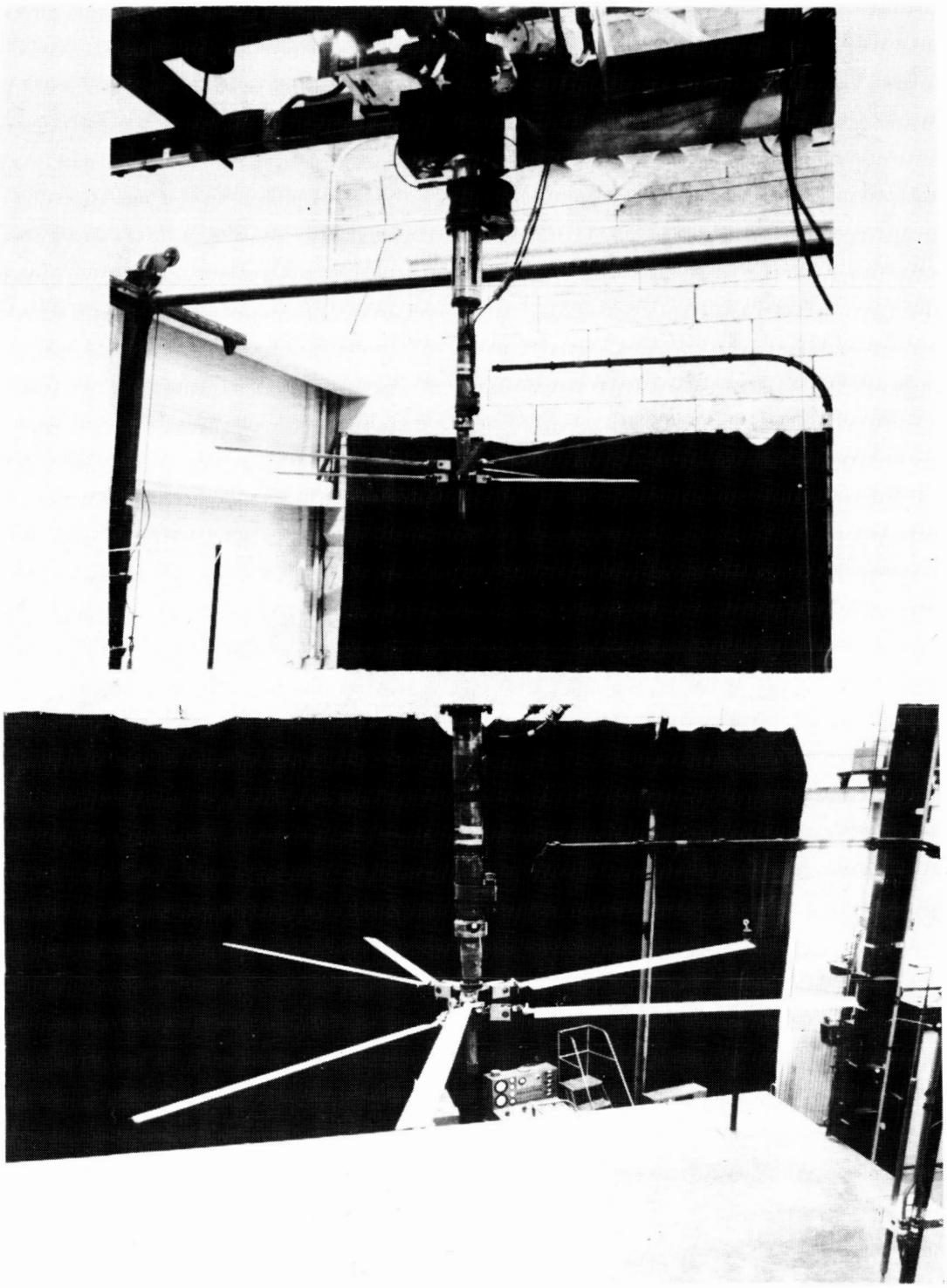

Figure 4. - Model Rotor Hover Test Rig.

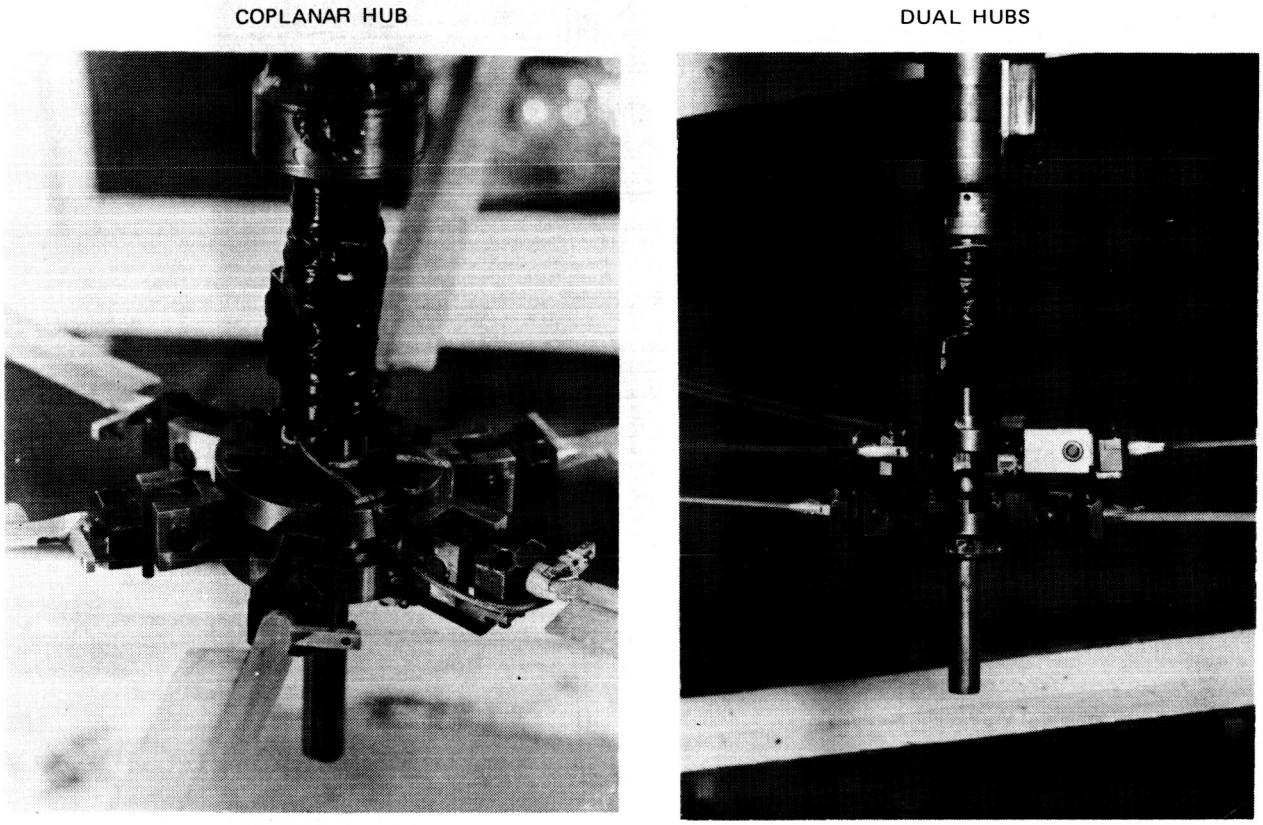

Figure 5. - Model Rotor Hubs.

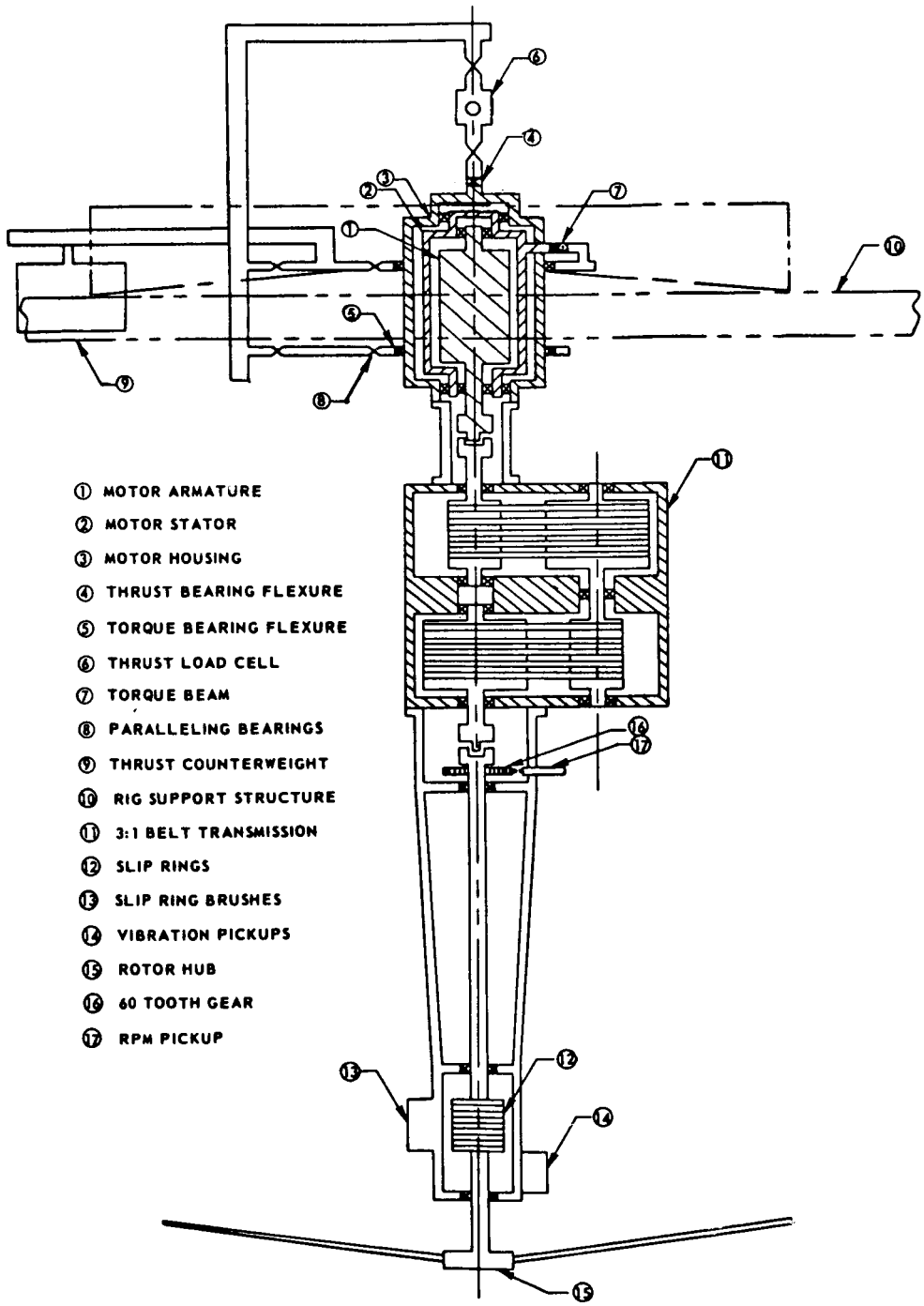

Figure 6. - Schematic Cross Section of Rotor Test Rig.

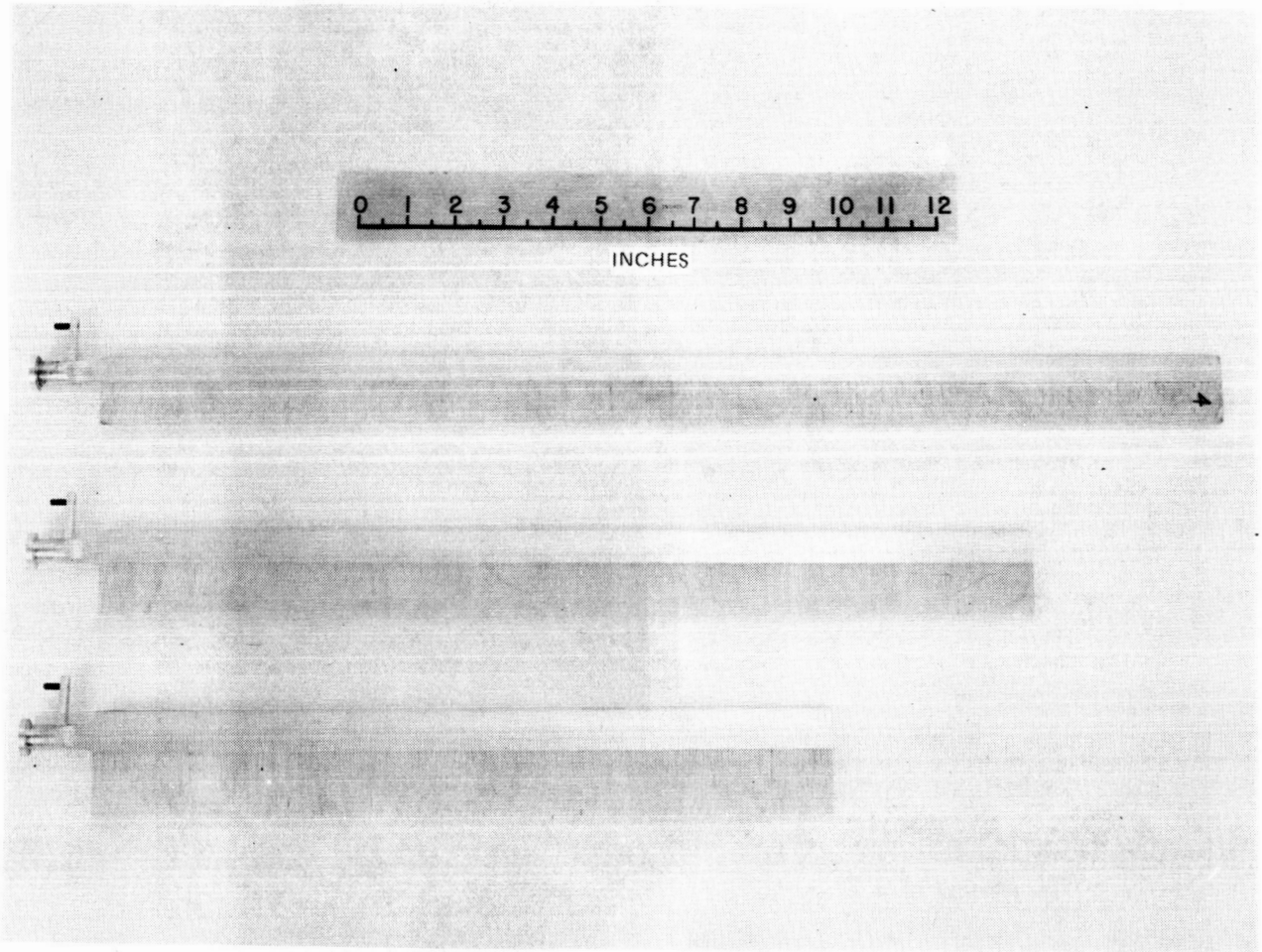

Figure 7. - Model Rotor Blades.

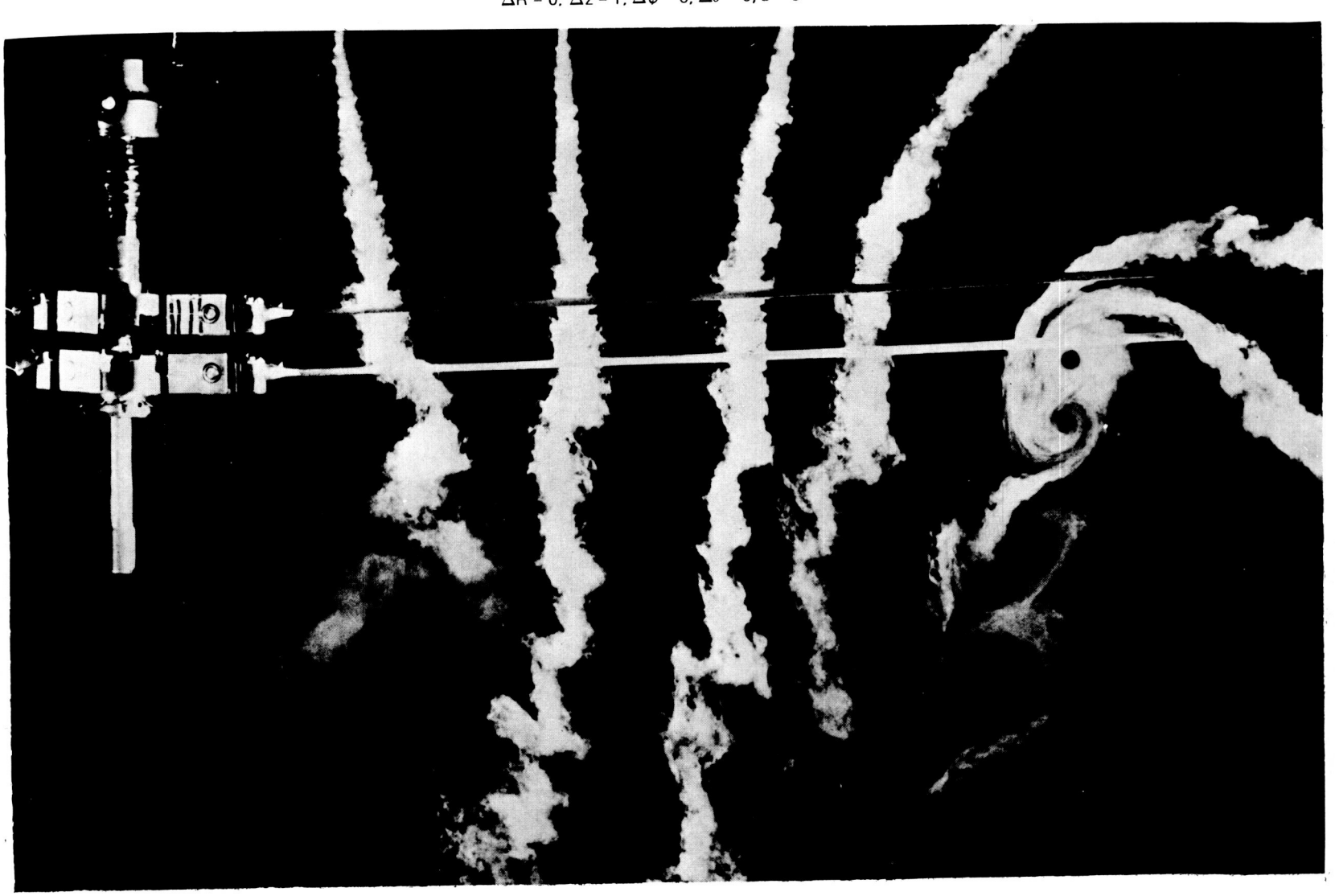

Figure 8. - Sample Flow Visualization Photograph for Variable-Geometry Rotor.

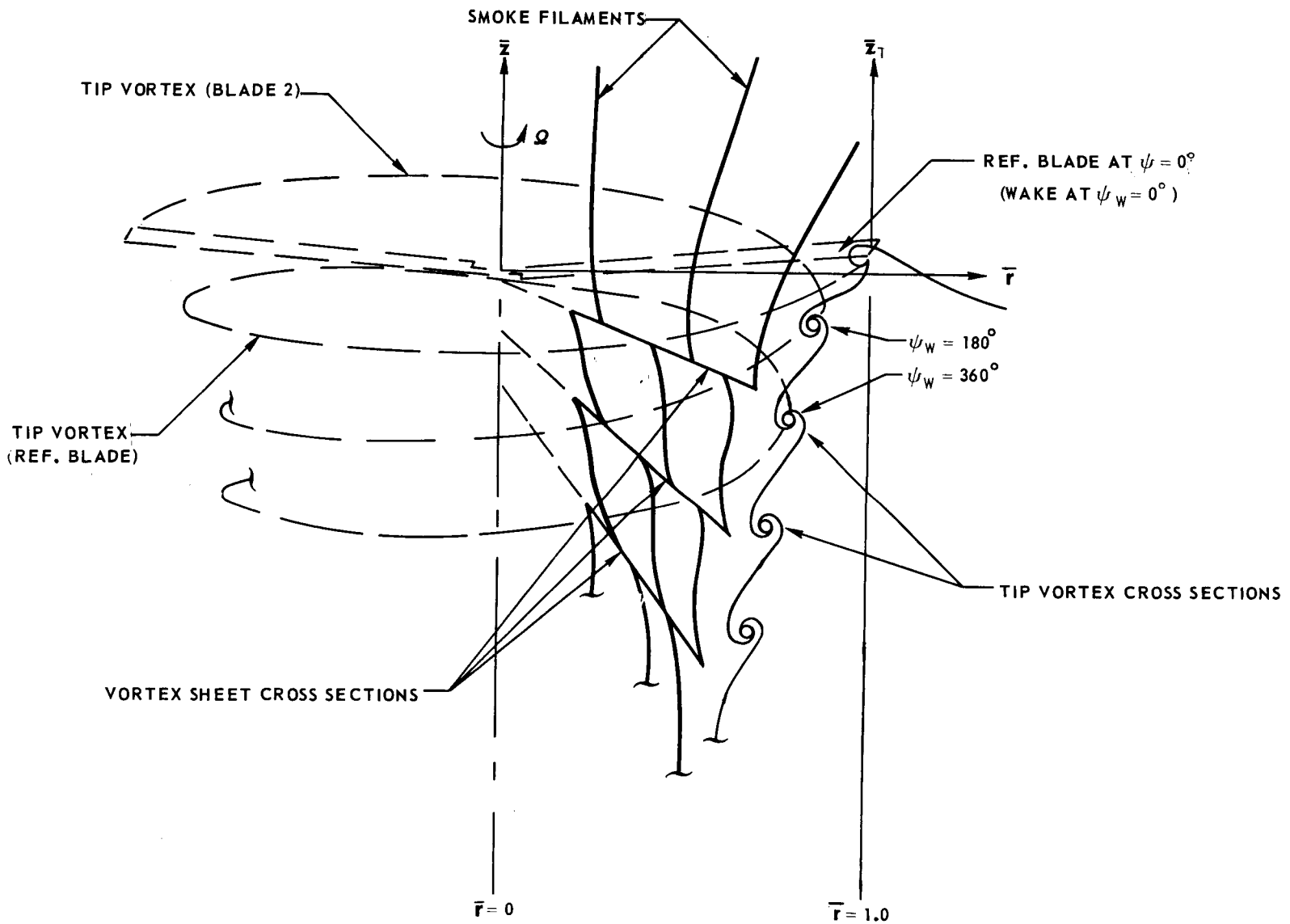

Figure 9. - Schematic of Wake Cross Section Showing Wake Coordinate System.

CONVENTIONAL ROTOR b = 6

$\psi = 0^{o}$

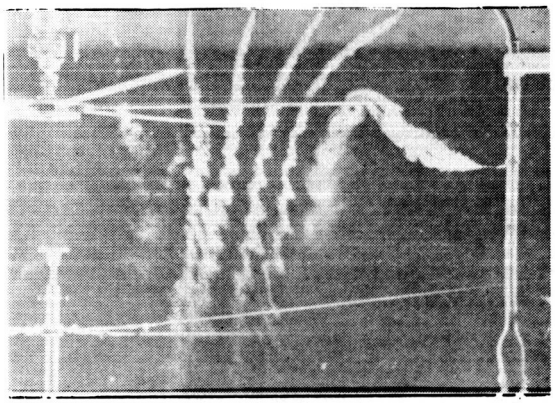

$\psi = 15^{o}$

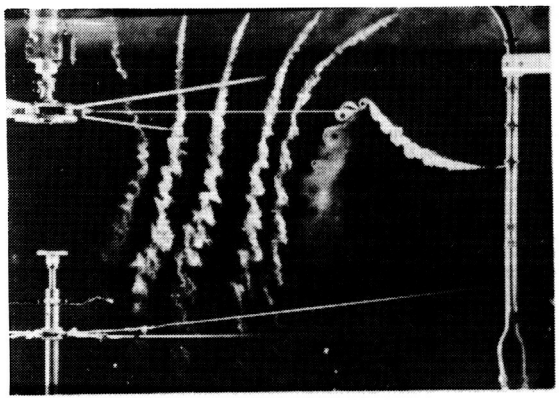

$\psi = 30^{o}$

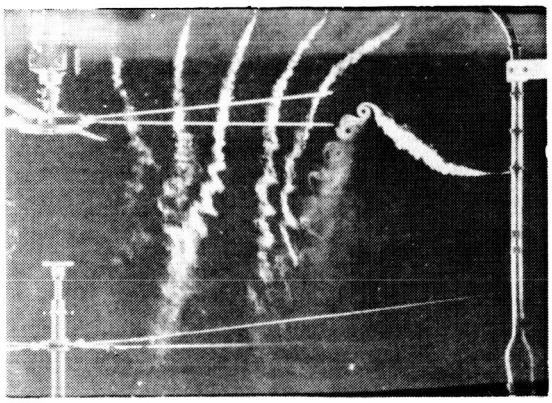

$\psi = 45^{o}$

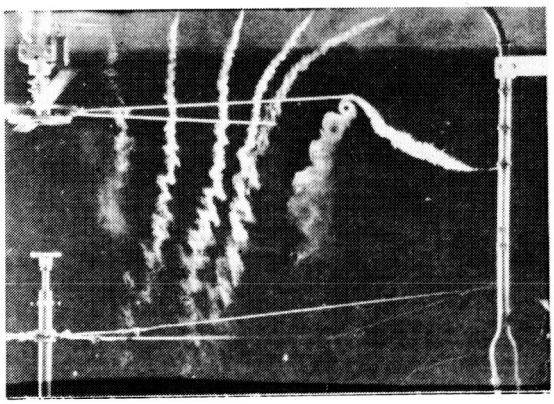

Figure 10. - Sequence of Flow Visualization Photographs Showing the Time History of the Wake.

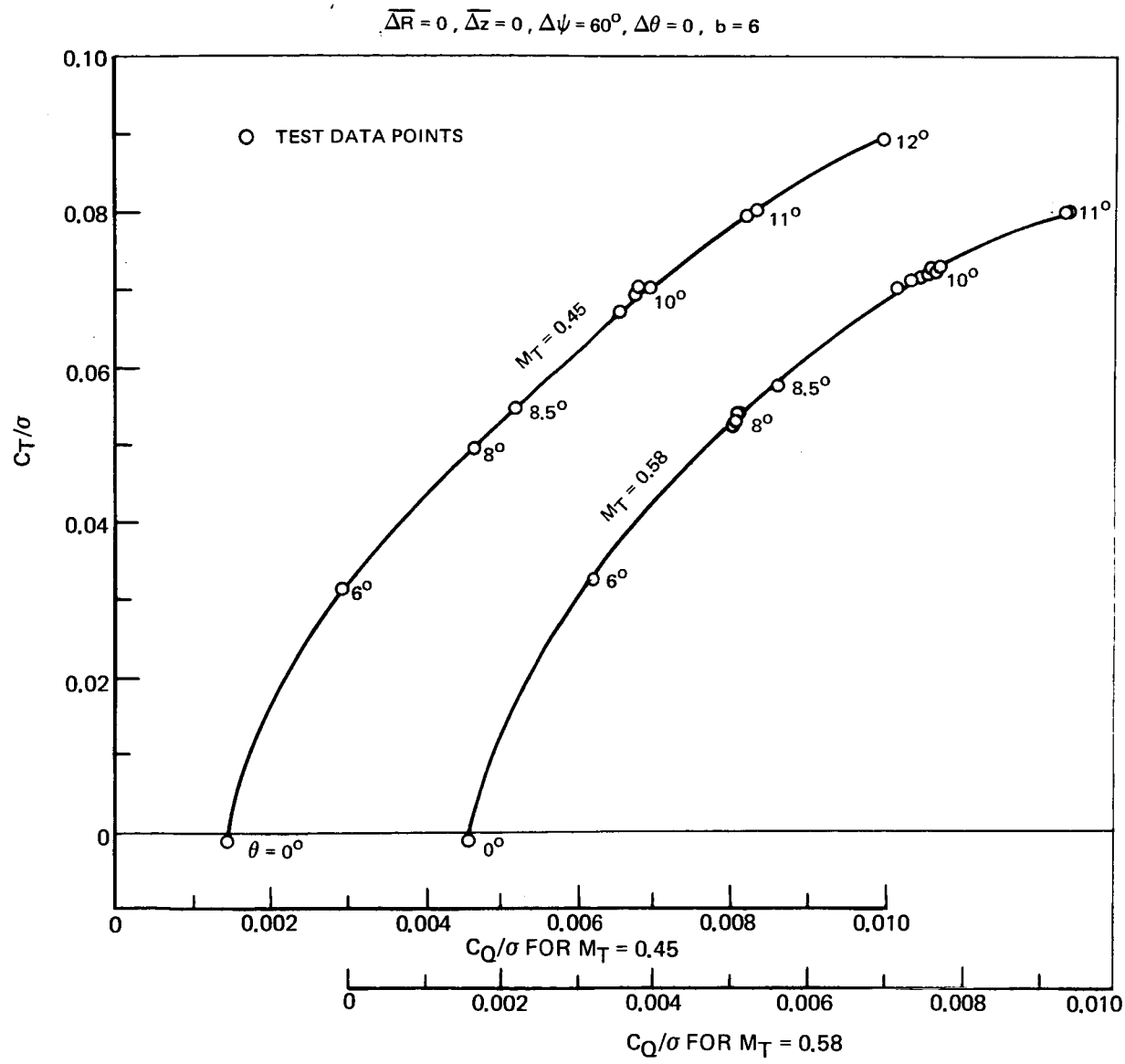

Figure 11. - Hover Performance of the Conventional 6-Bladed Rotor.

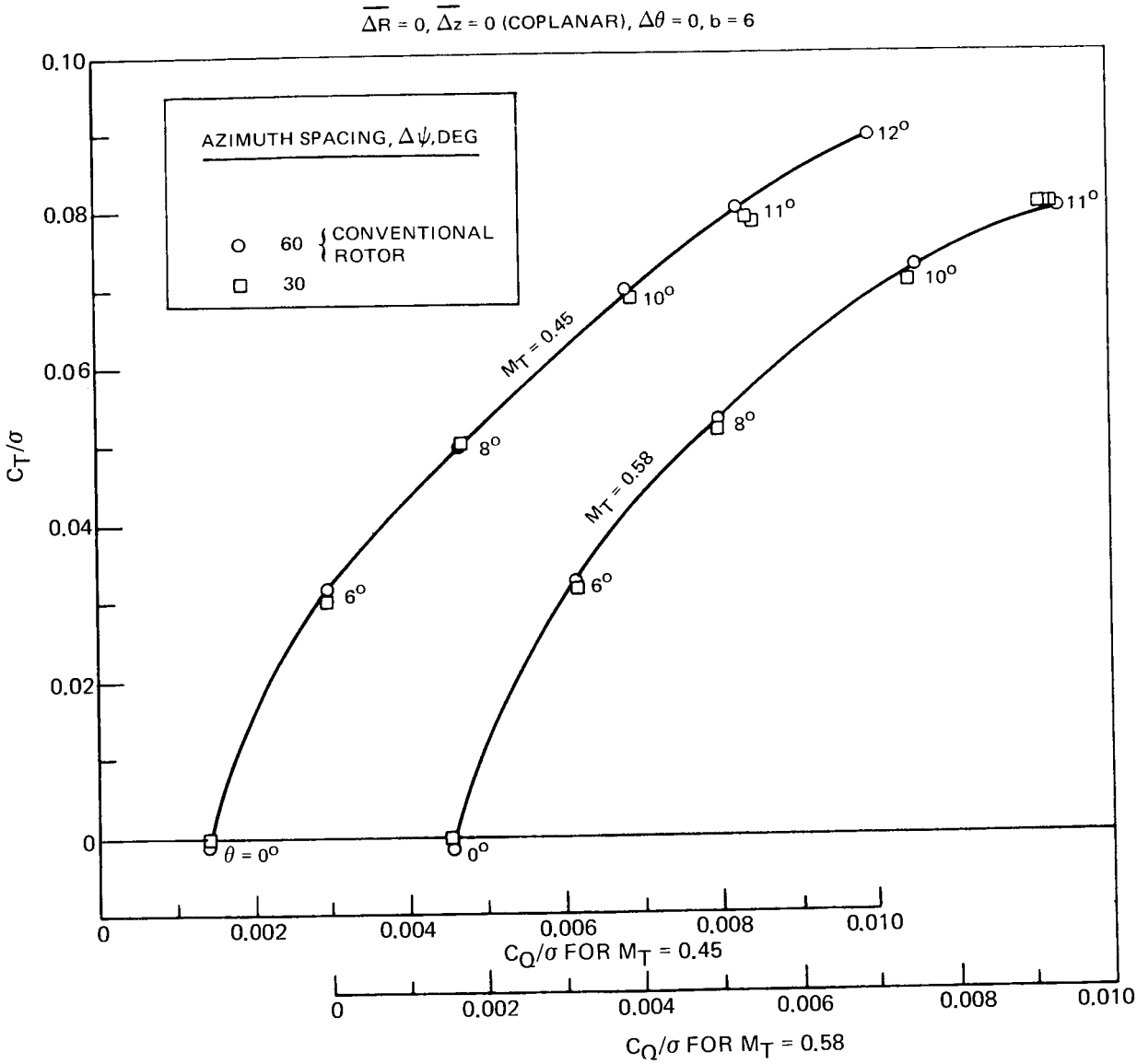

Figure 12. - Independent Effect of Azimuth Spacing on Hover Performance.

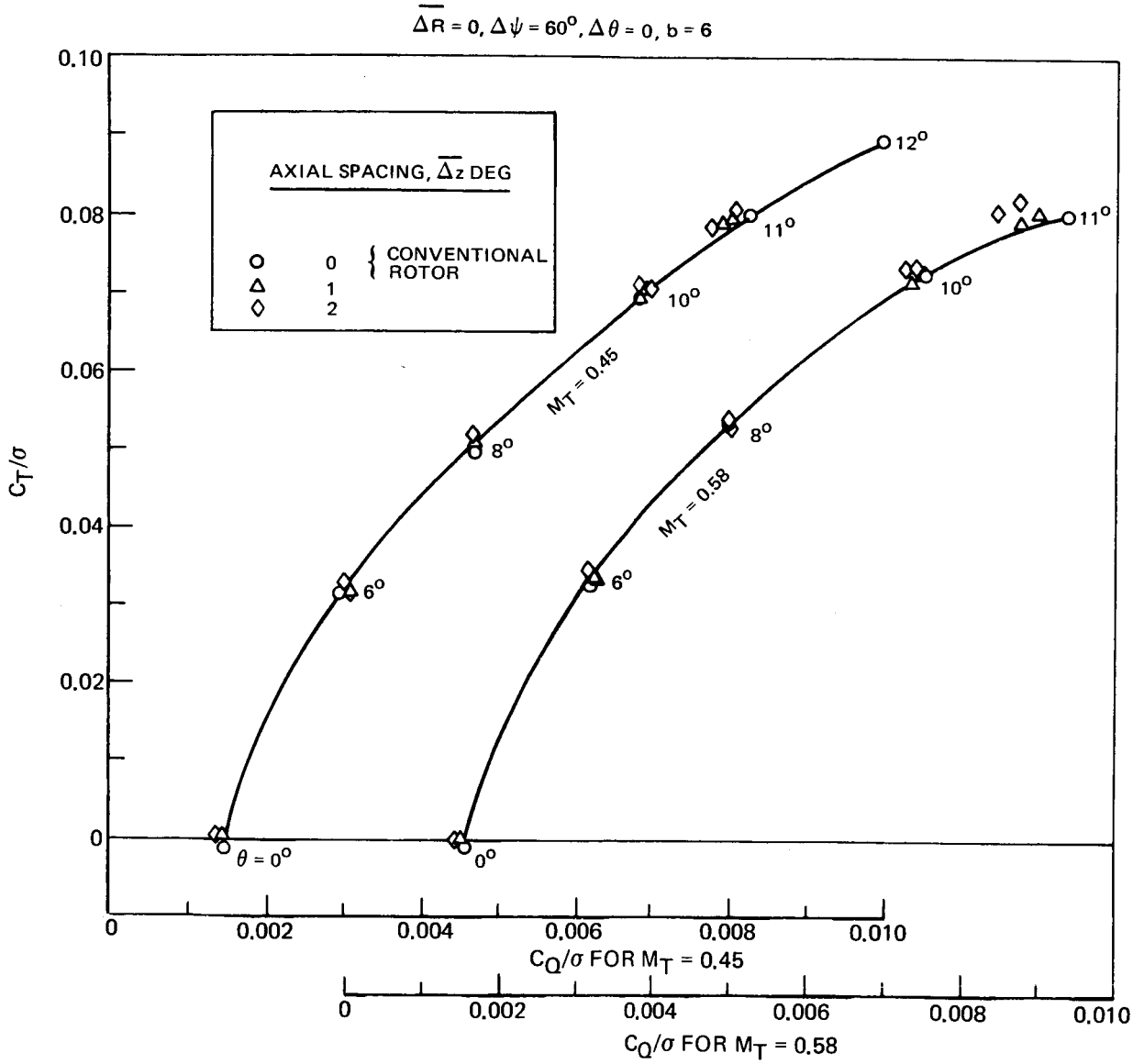

Figure 13. - Independent Effect of Axial Spacing on Hover Performance.

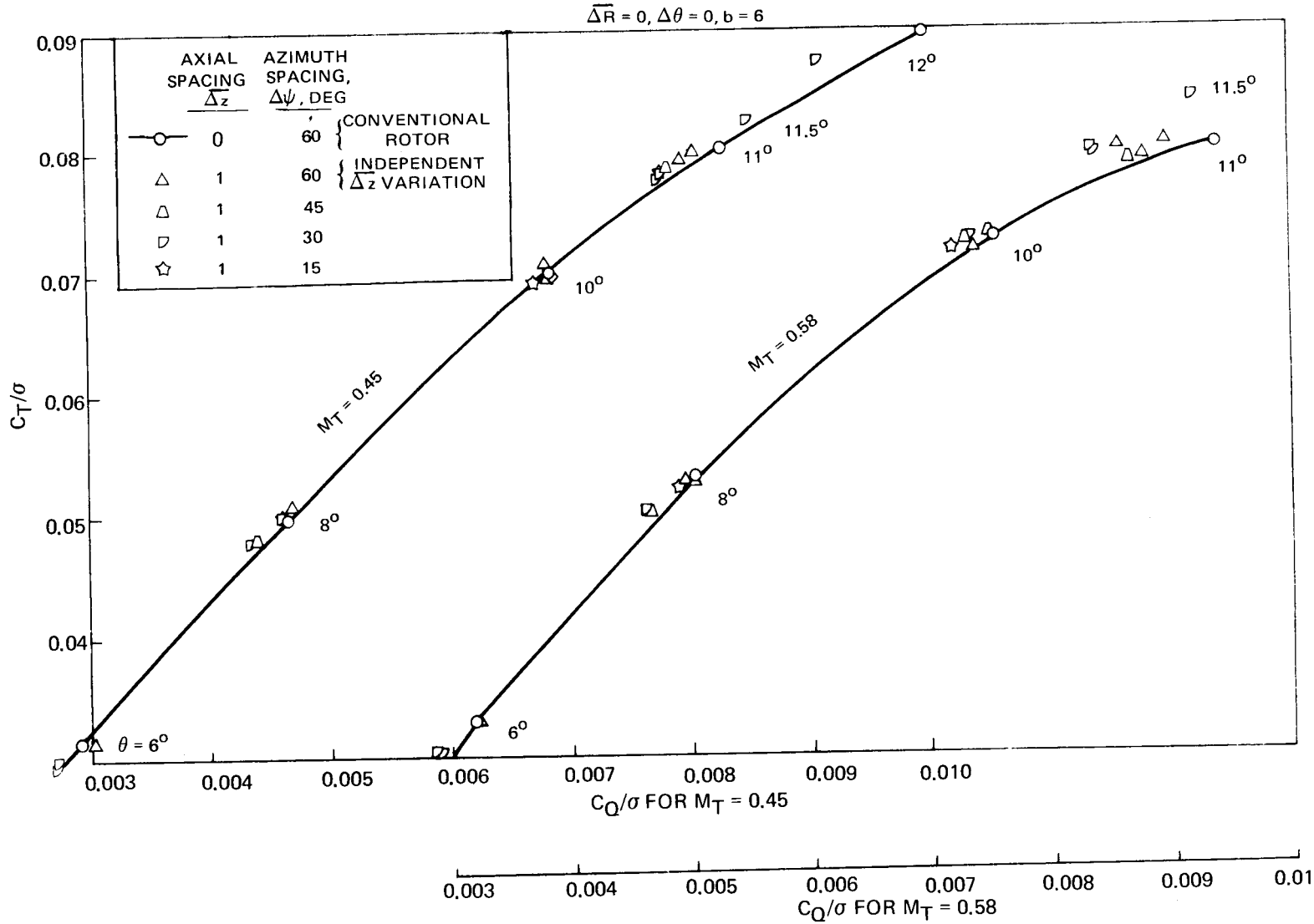

(a) - Positive Azimuth Spacings.

Figure 14. - Effect of Combined Axial and Azimuth Spacing on Hover Performance for Axial Spacing, $\overline{\Delta z}$ = 1.

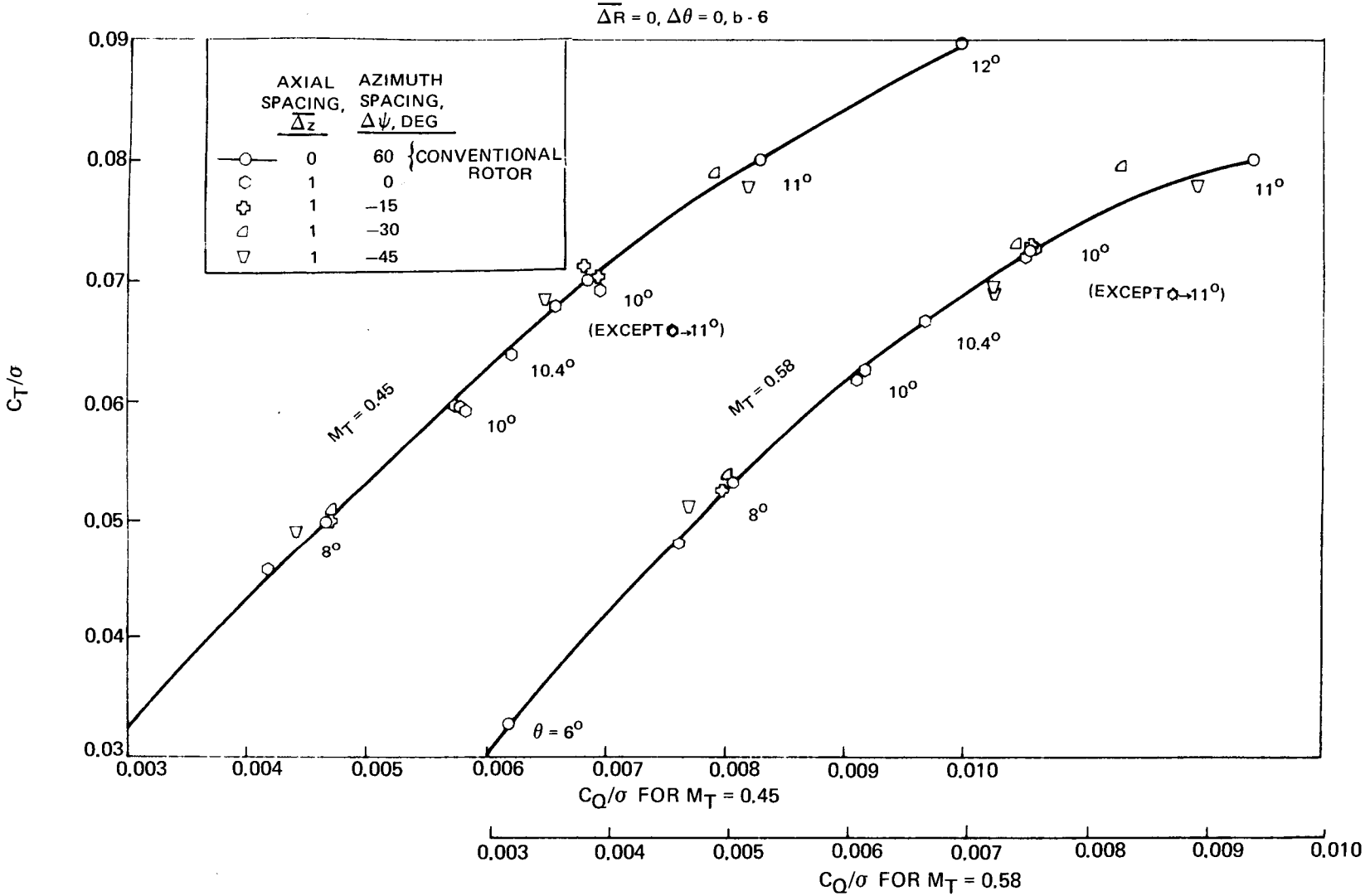

(b) - Zero and Negative Azimuth Spacings.

Figure 14. - Concluded.

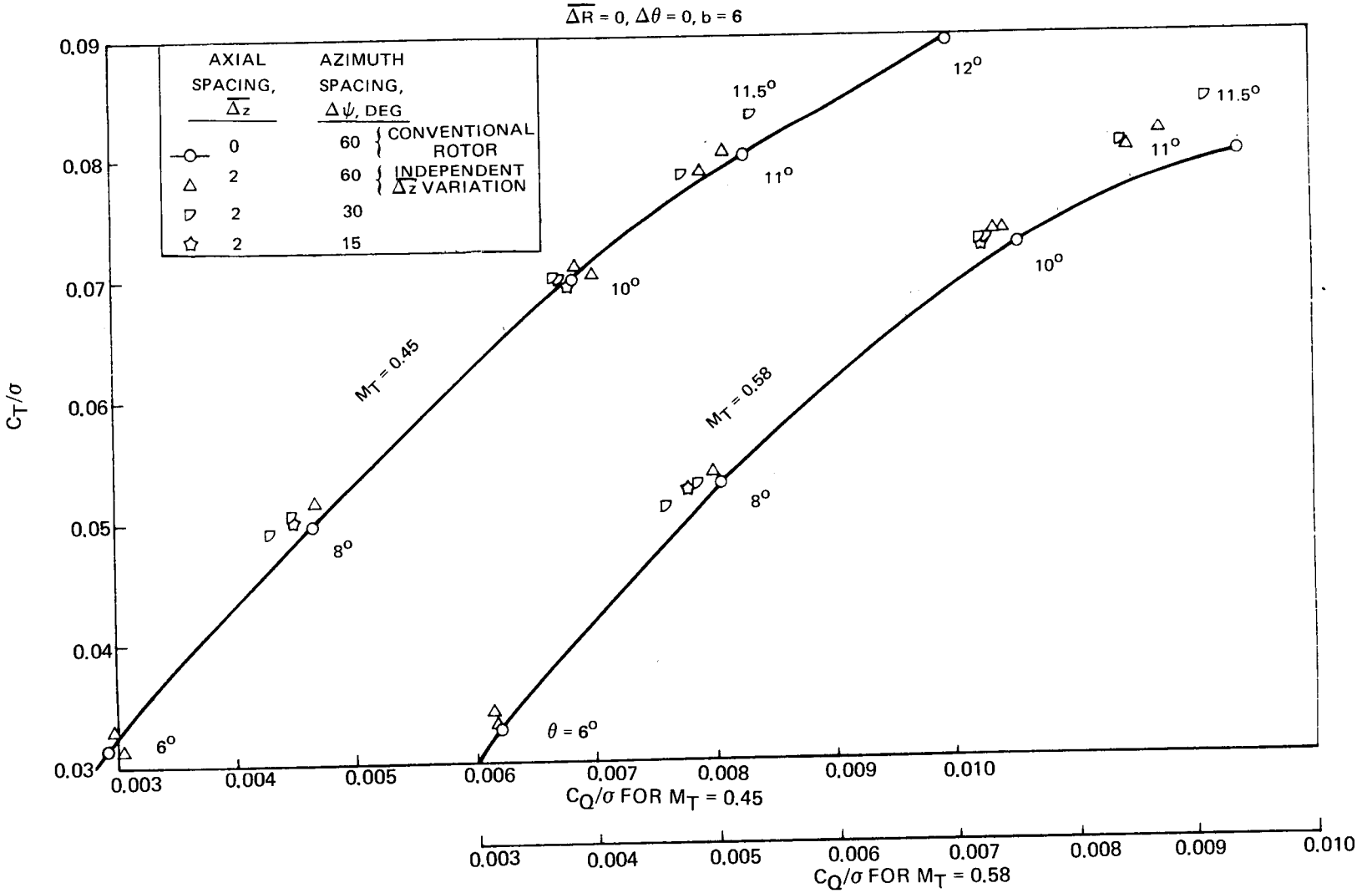

(a) - Positive Azimuth Spacings.

Figure 15. - Effect of Combined Axial and Azimuth Spacings on Hover Performance for Axial Spacing, $\overline{\Delta z}$ = 2.

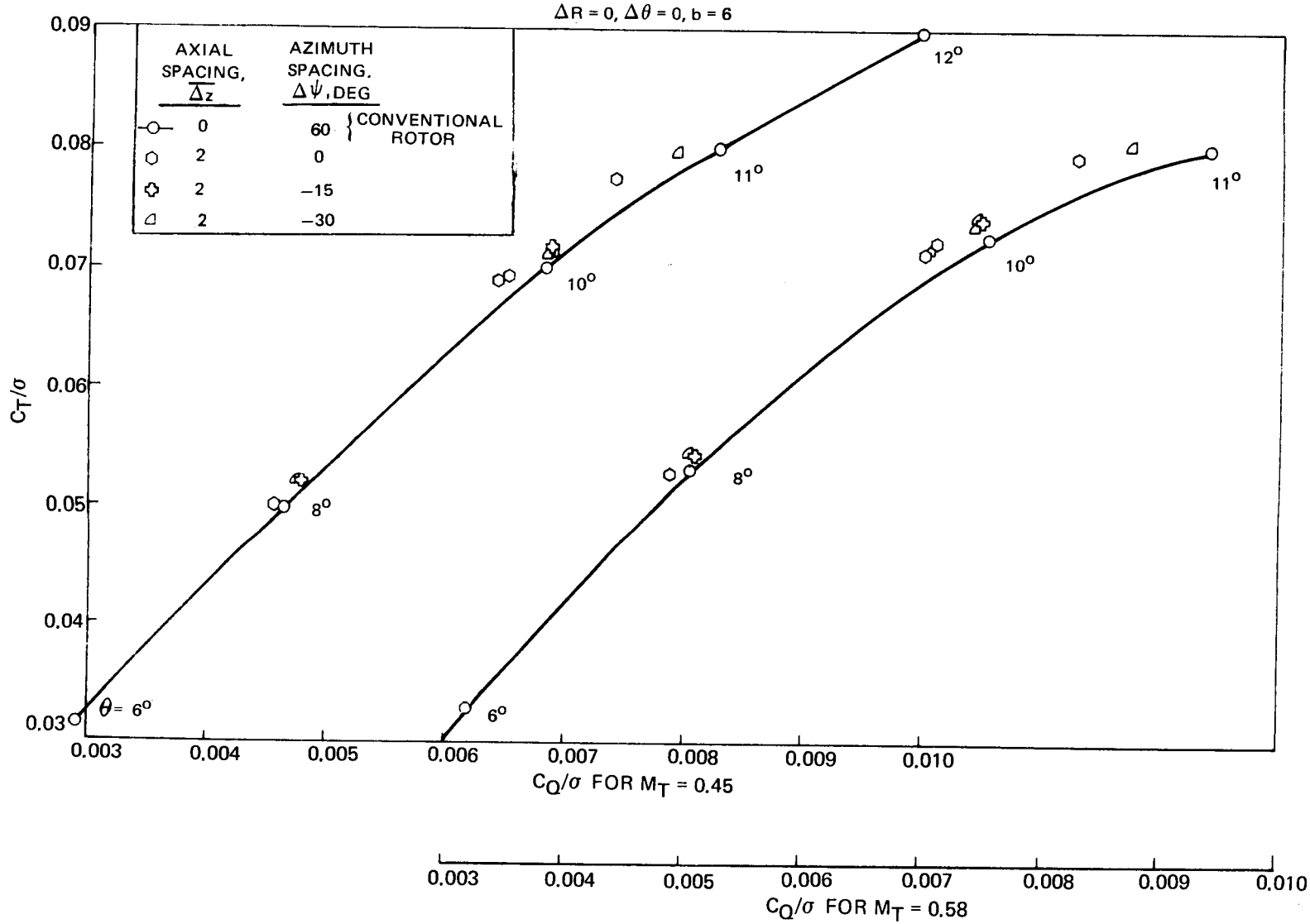

(b) - Zero and Negative Azimuth Spacings.

Figure 15. - Concluded.

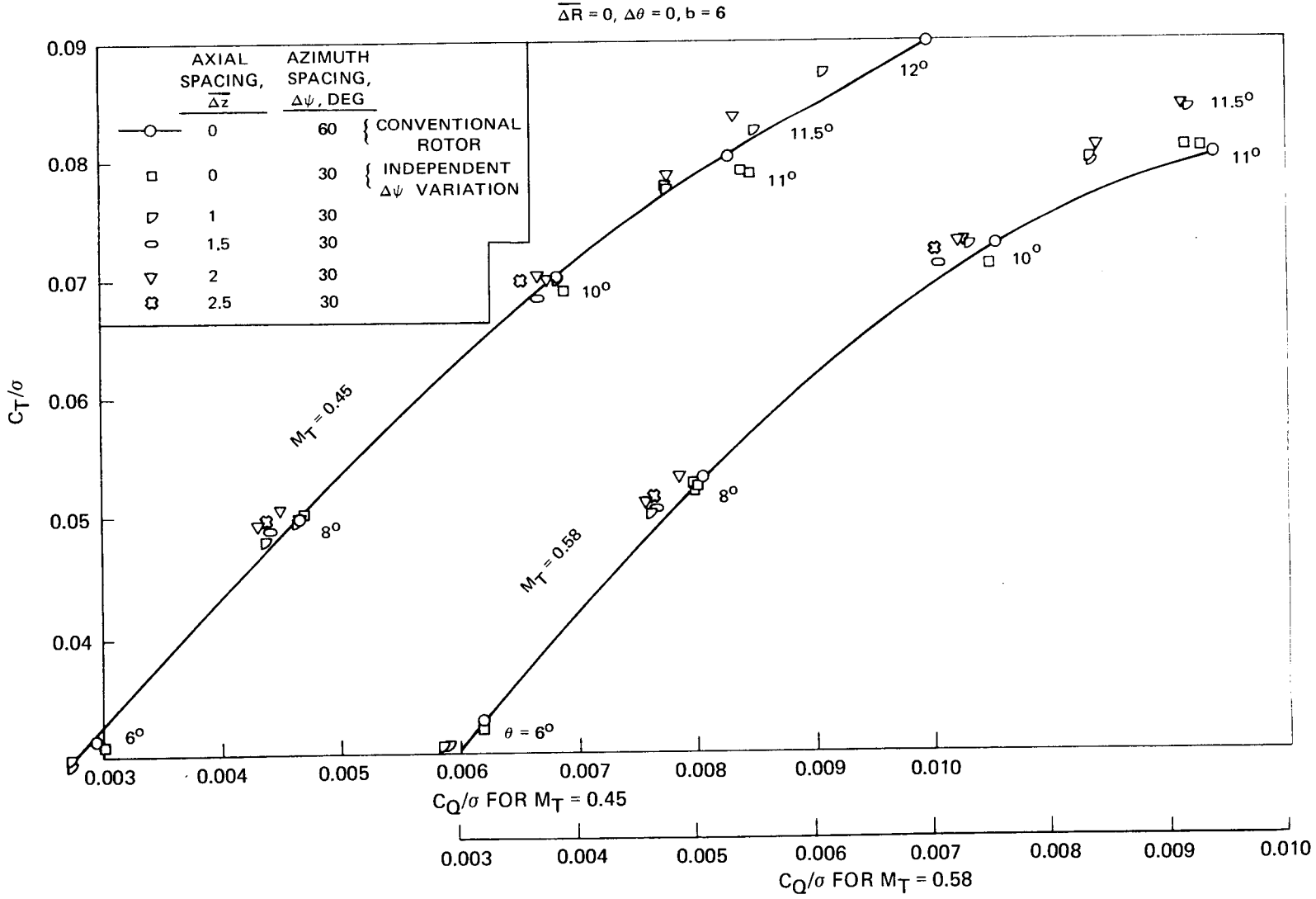

(a) - Test Data Points.

Figure 16. - Effect of Axial Spacing on Hover Performance for an Azimuth Spacing of 30 deg.

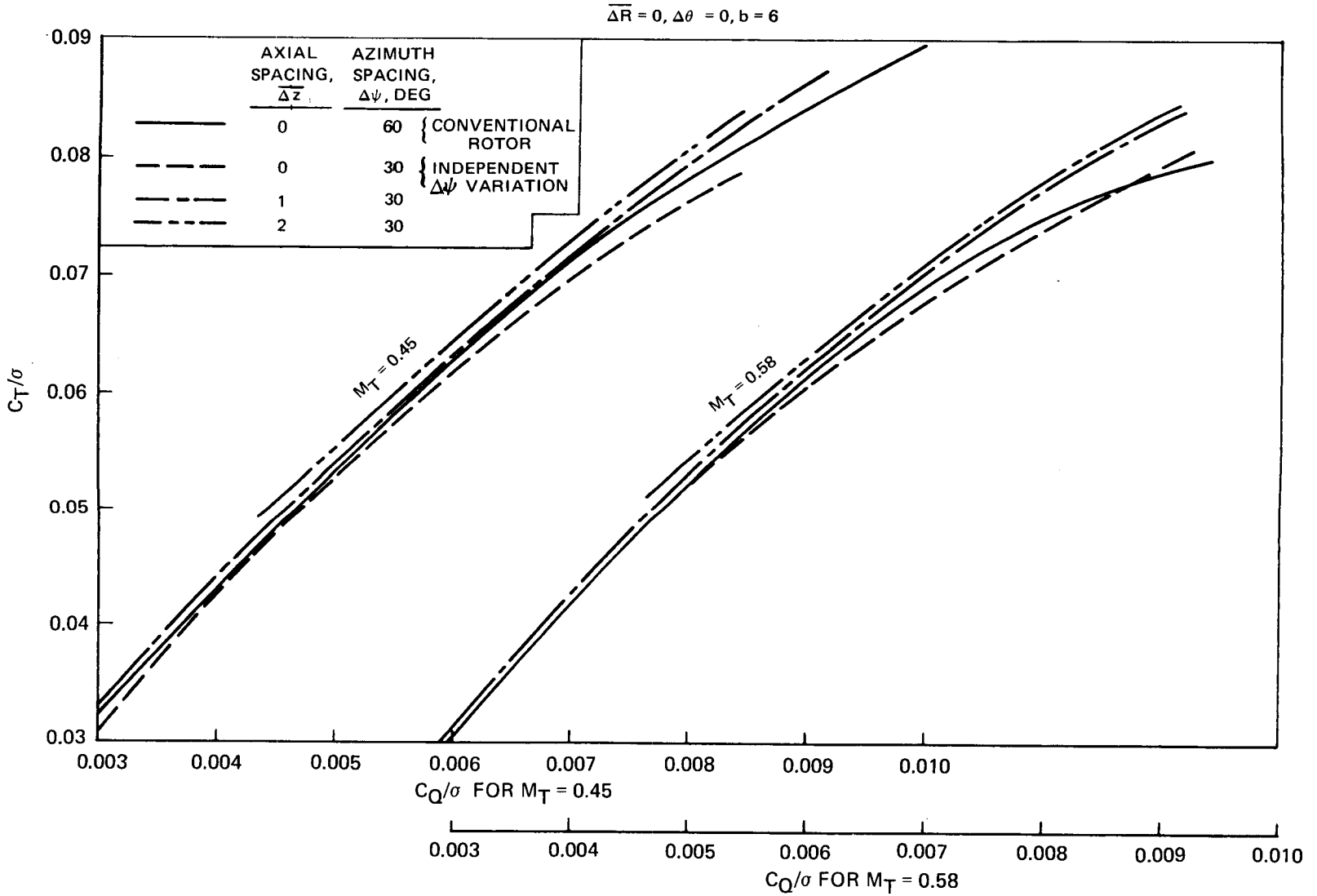

(b) - Faired Data.

Figure 16. - Concluded.

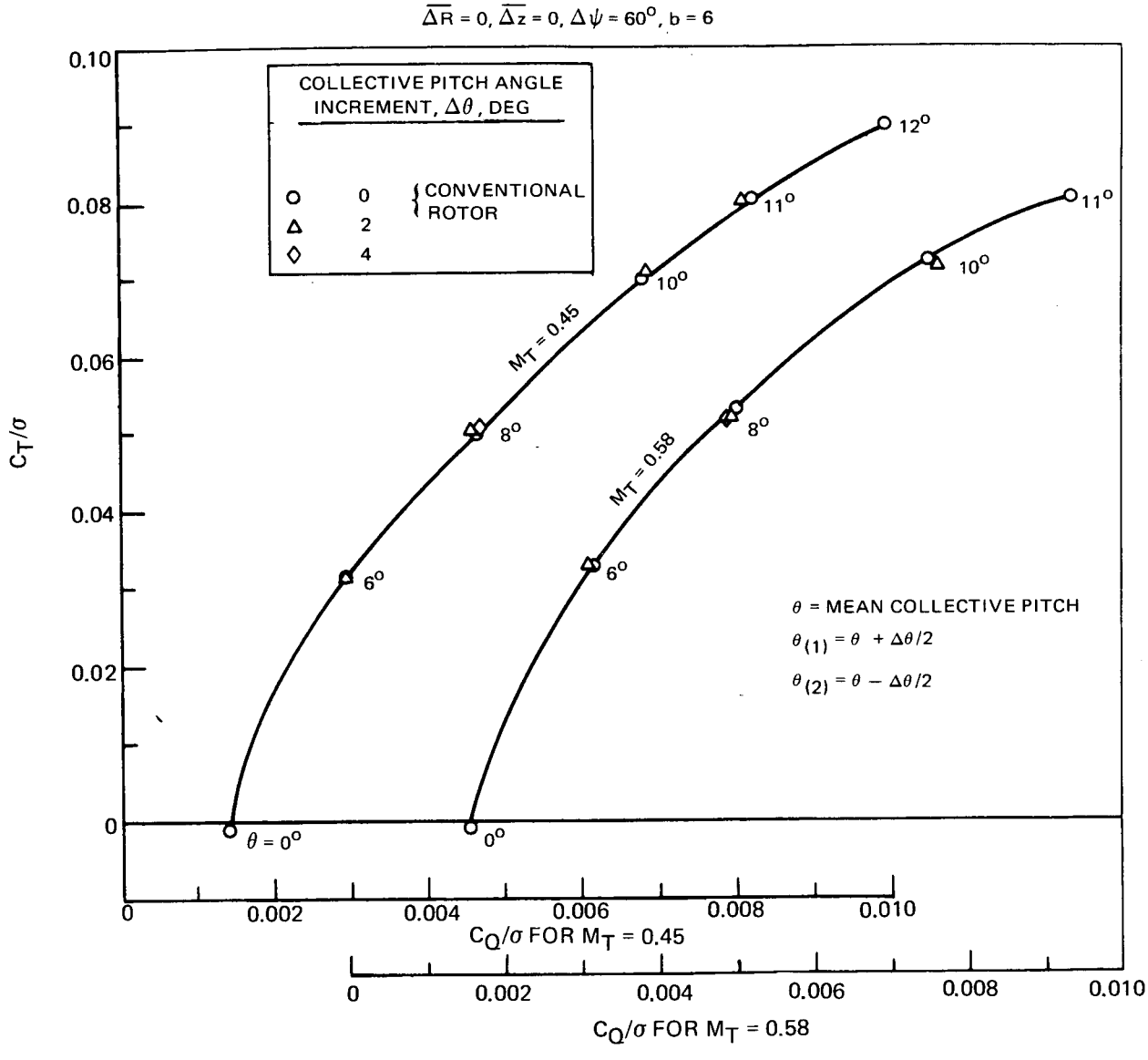

Figure 17. - Independent Effect of Differential Collective Pitch on Hover Performance.

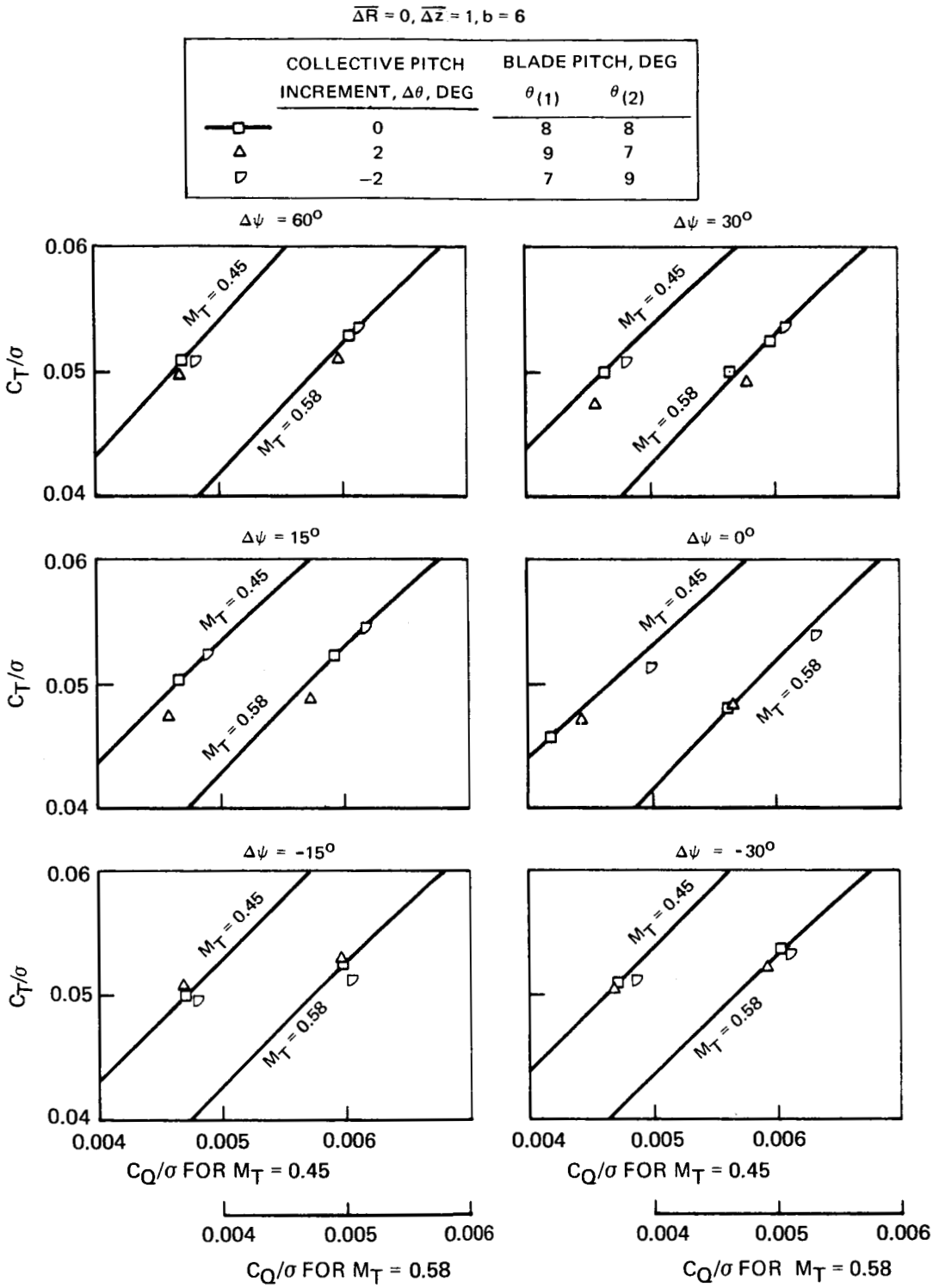

(a) - Mean Collective Pitch, θ = 8 deg.

Figure 18. - Effect of Collective Pitch Increment on Hover Performance for Various Combinations of Axial and Azimuth Spacings.

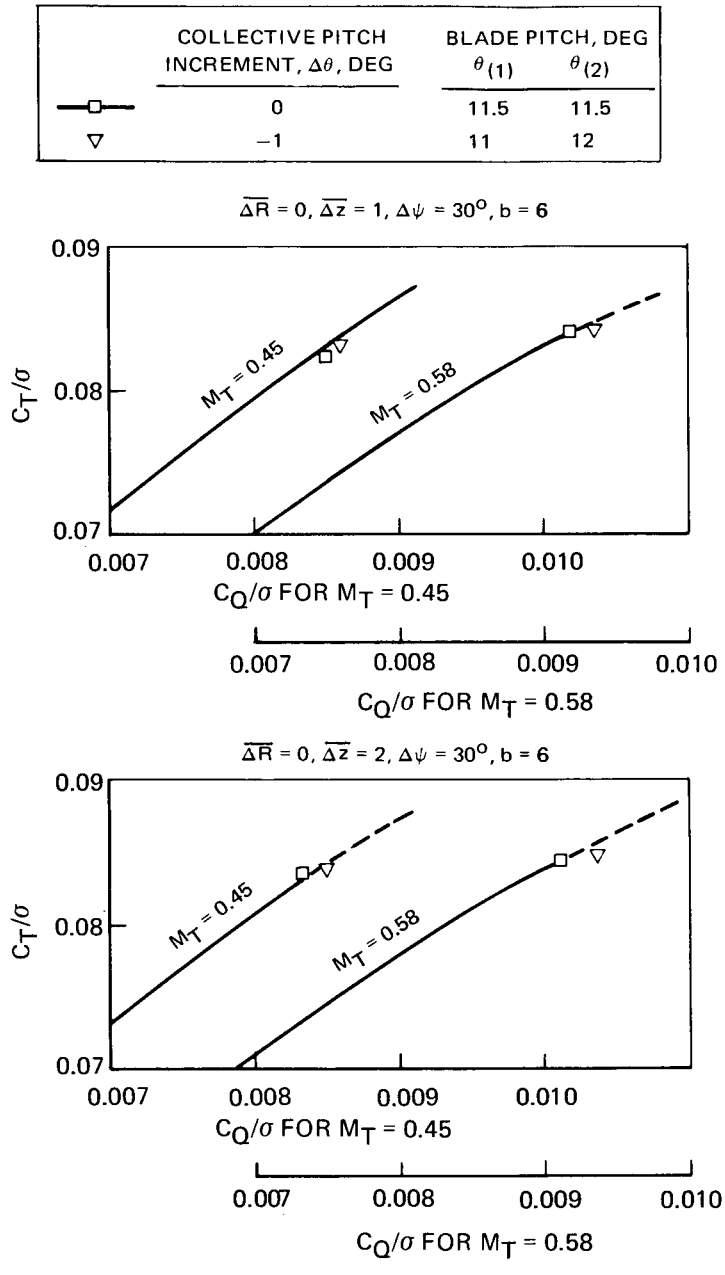

(b) - Mean Collective Pitch, θ = 11.5 deg.

Figure 18. - Concluded.

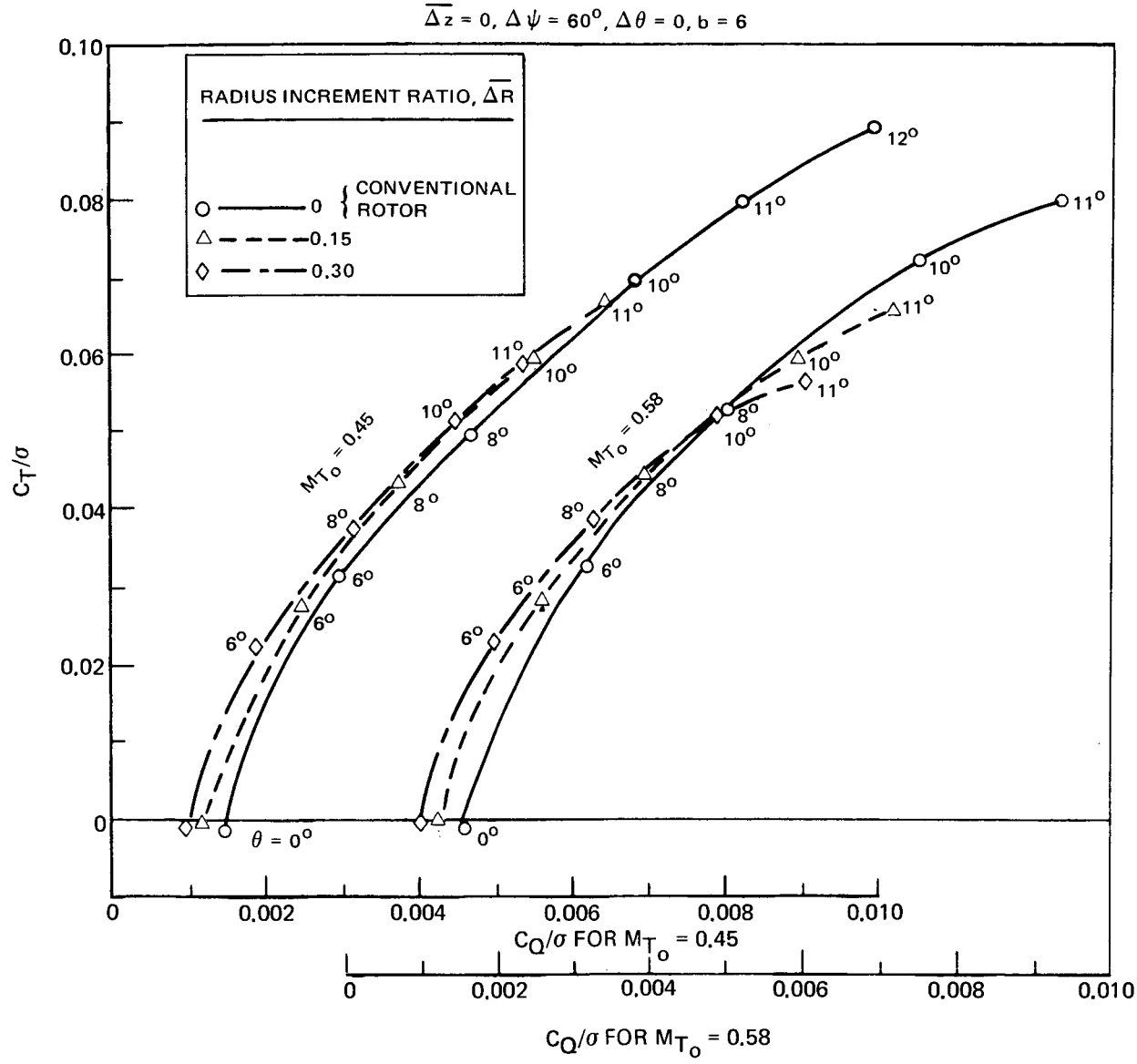

Figure 19. - Independent Effect of Differential Radius on Hover Performance.

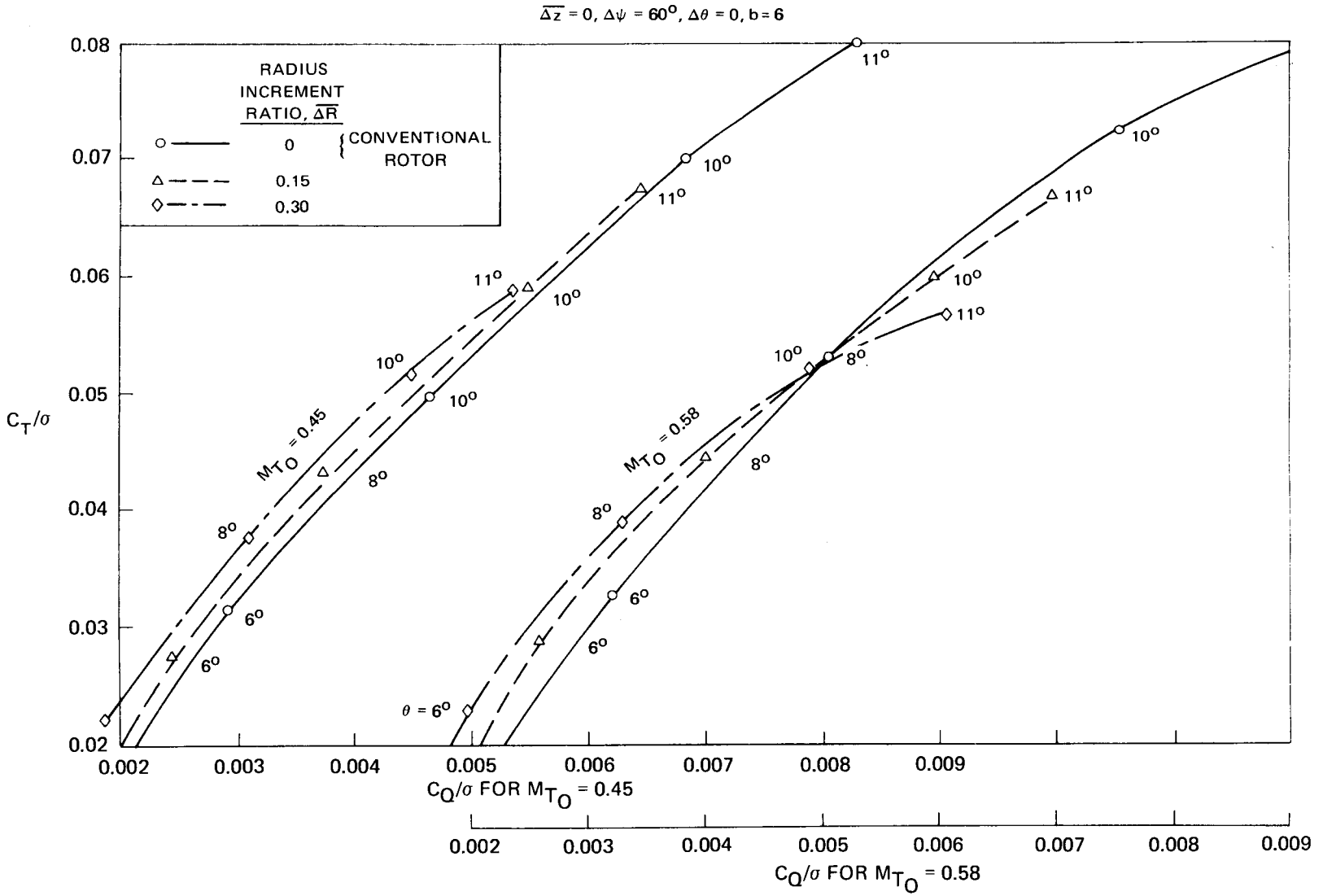

(a) - Azimuth Spacing, $\Delta\psi$ = 60 deg.

Figure 20. - Effect of Differential Radius on Hover Performance for Coplanar Blades and Selected Azimuth Spacings.

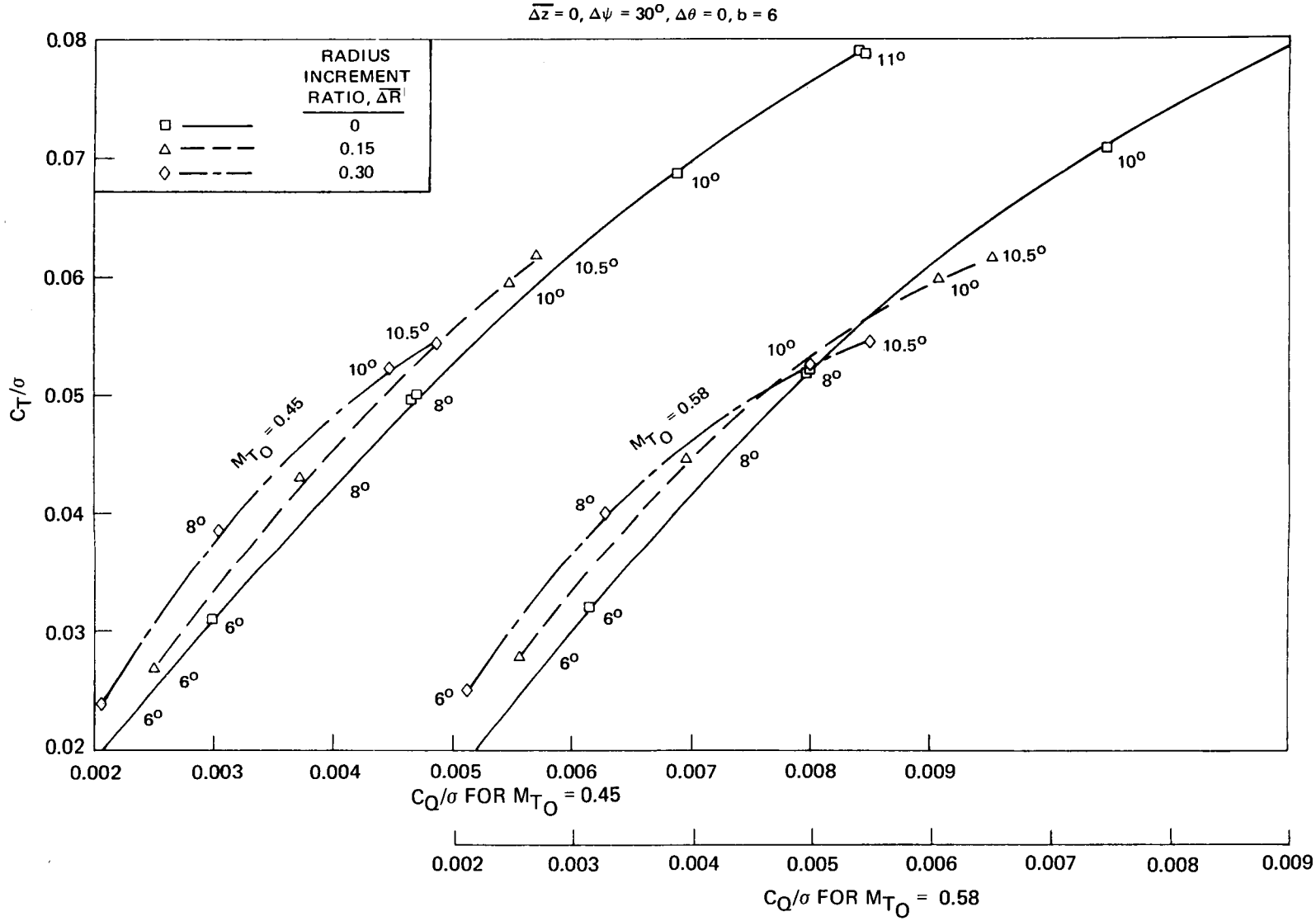

(b) - Azimuth Spacing, $\Delta\psi$ = 30 deg.

Figure 20. - Continued.

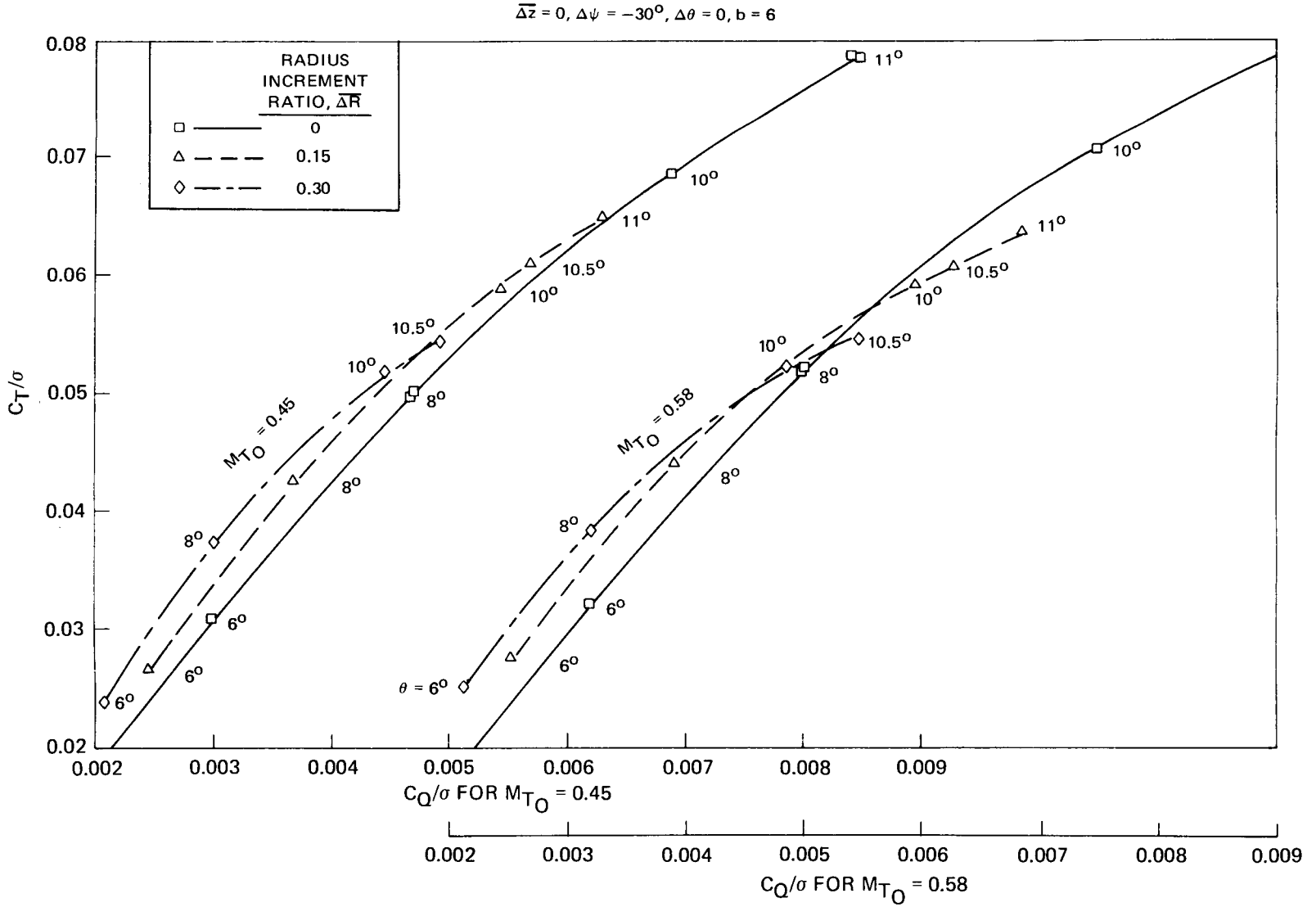

(c) - Azimuth Spacing, $\Delta\psi$ = −30 deg.

Figure 20. - Concluded.

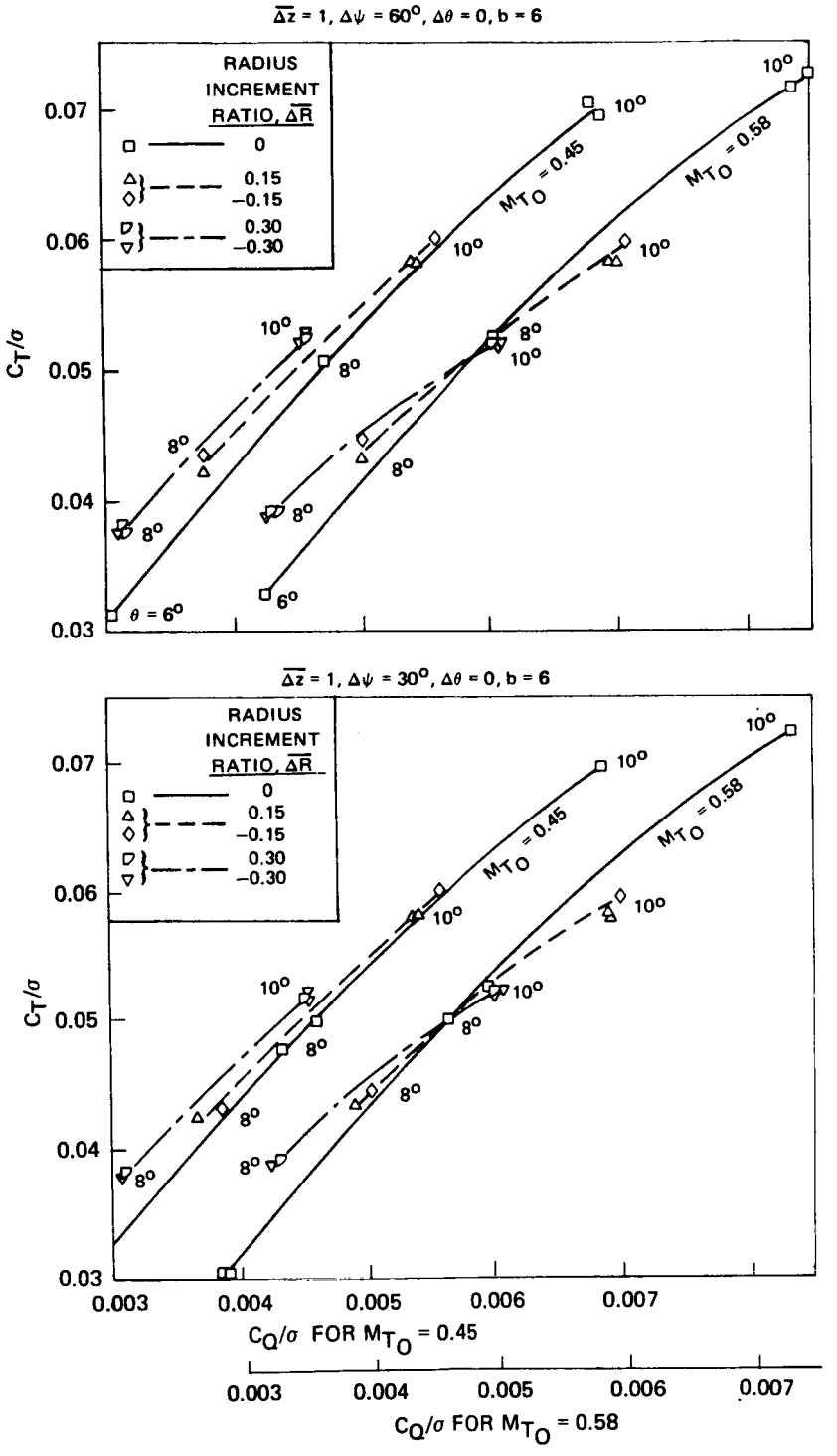

(a) - $\overline{\Delta}z$ = 1, $\Delta\psi$= 60° and 30°.

Figure 21. - Effect of Differential Radius on Hover Performance for Combined Axial and Azimuth Spacings.

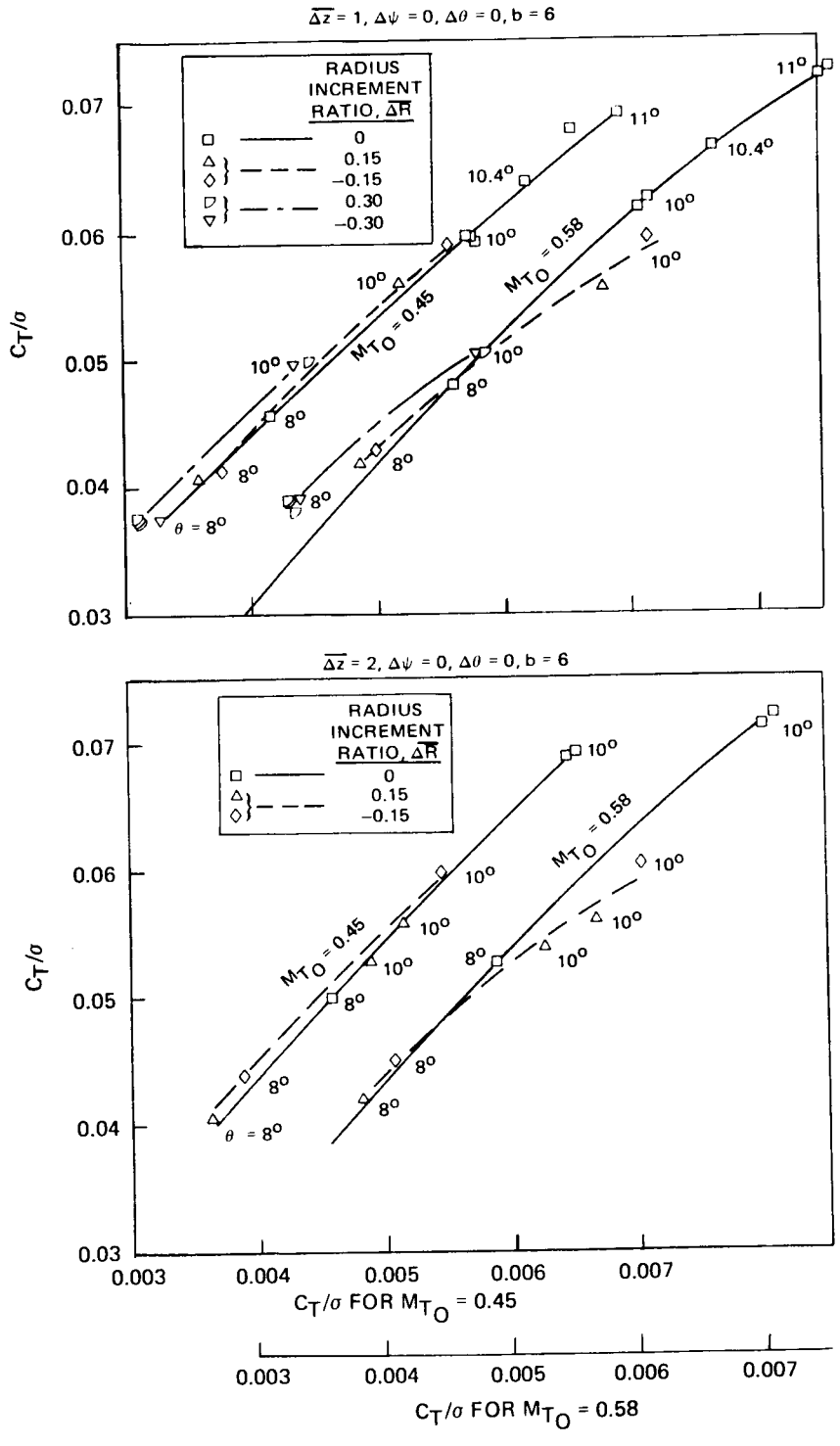

(b) - $\overline{\Delta z}$ = 1 and 2, $\Delta\psi$ = 0.

Figure 21. - Continued.

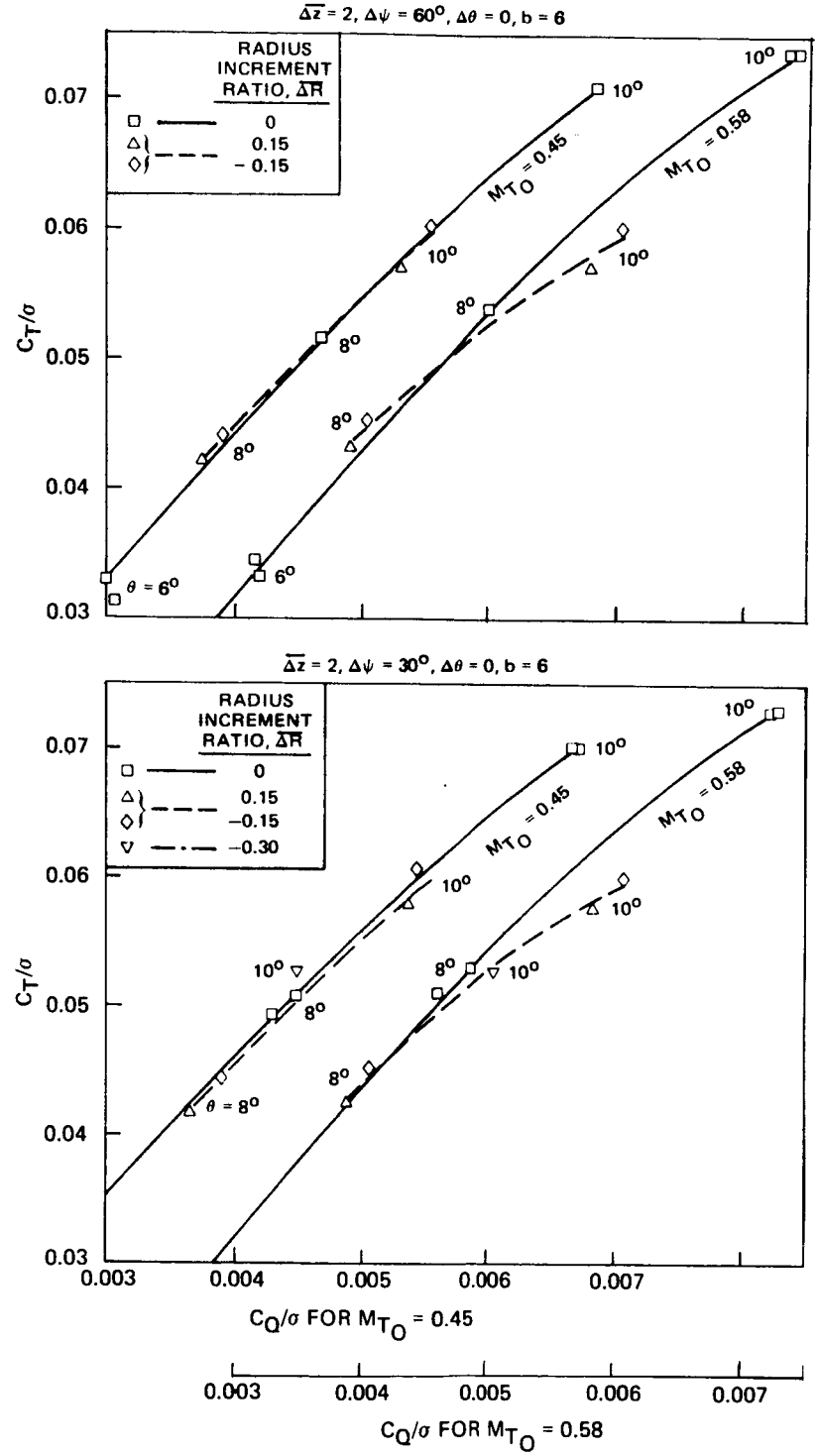

(c) - $\overline{\Delta z}$ = 2, $\Delta\psi$ = 60° and 30°

Figure 21. - Concluded.

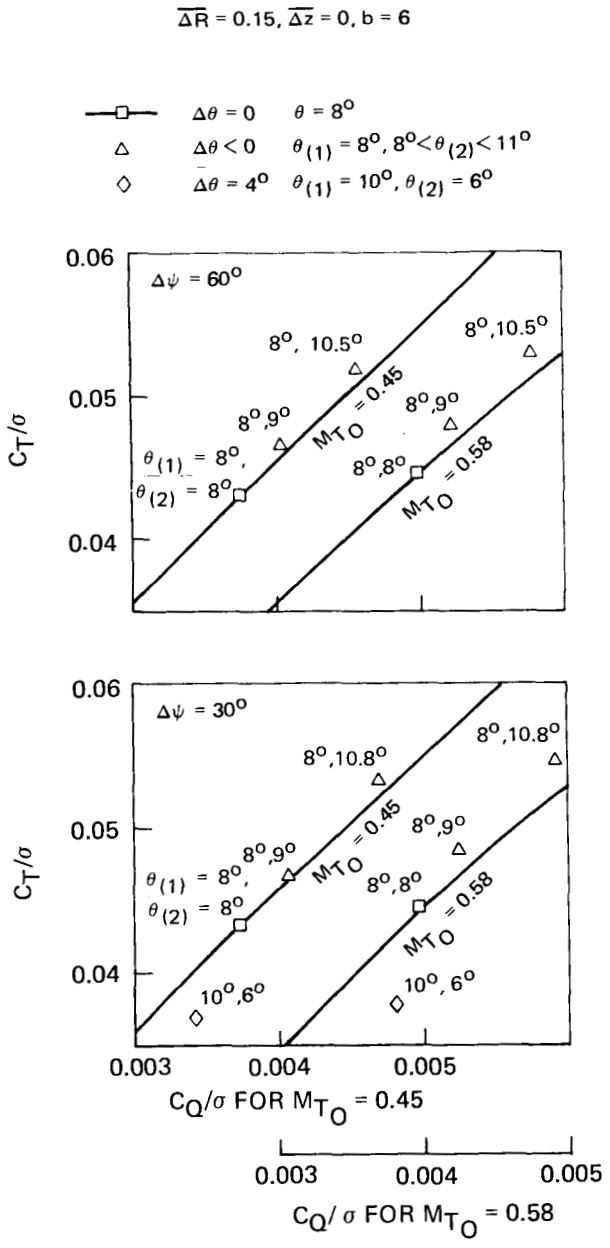

(a) - Coplanar Rotors -- $\overline{\Delta z}$ = 0.

Figure 22. - Effect of Differential Collective Pitch on Hover Performance for a Configuration With Differential Radius.

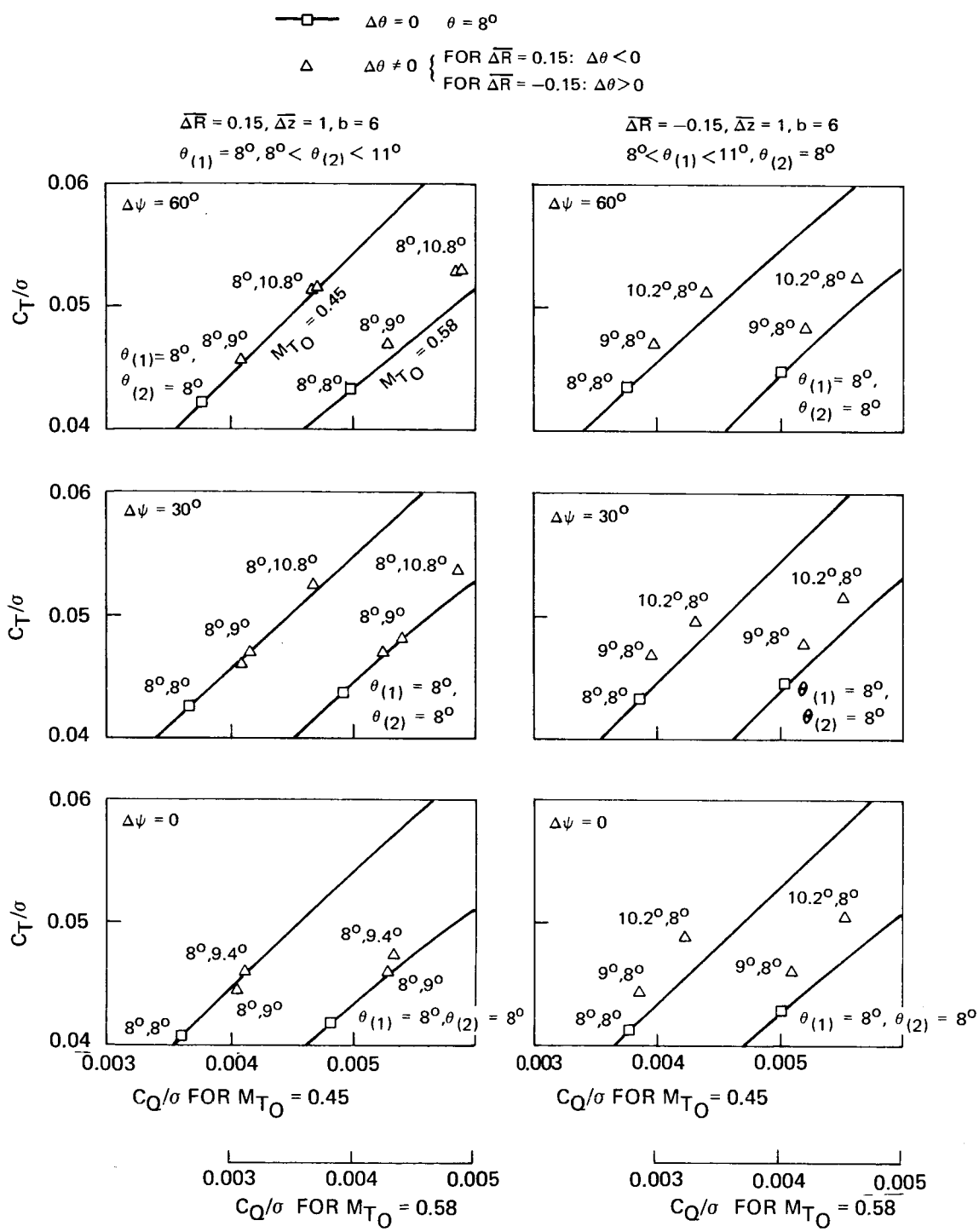

(b) - Rotors With Axial Spacing -- $\Delta\bar{z} = 1$.

Figure 22. - Concluded.

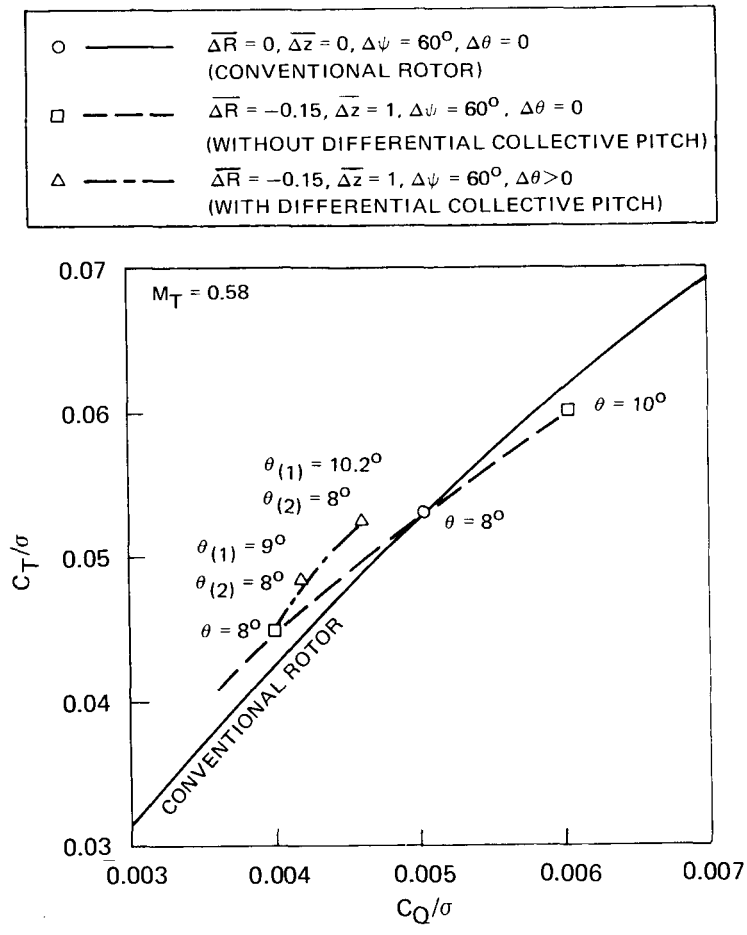

Figure 23. - Sample Results Showing Improved Performance Near Stall for a Configuration With Differential Collective Pitch Combined With Differential Radius.

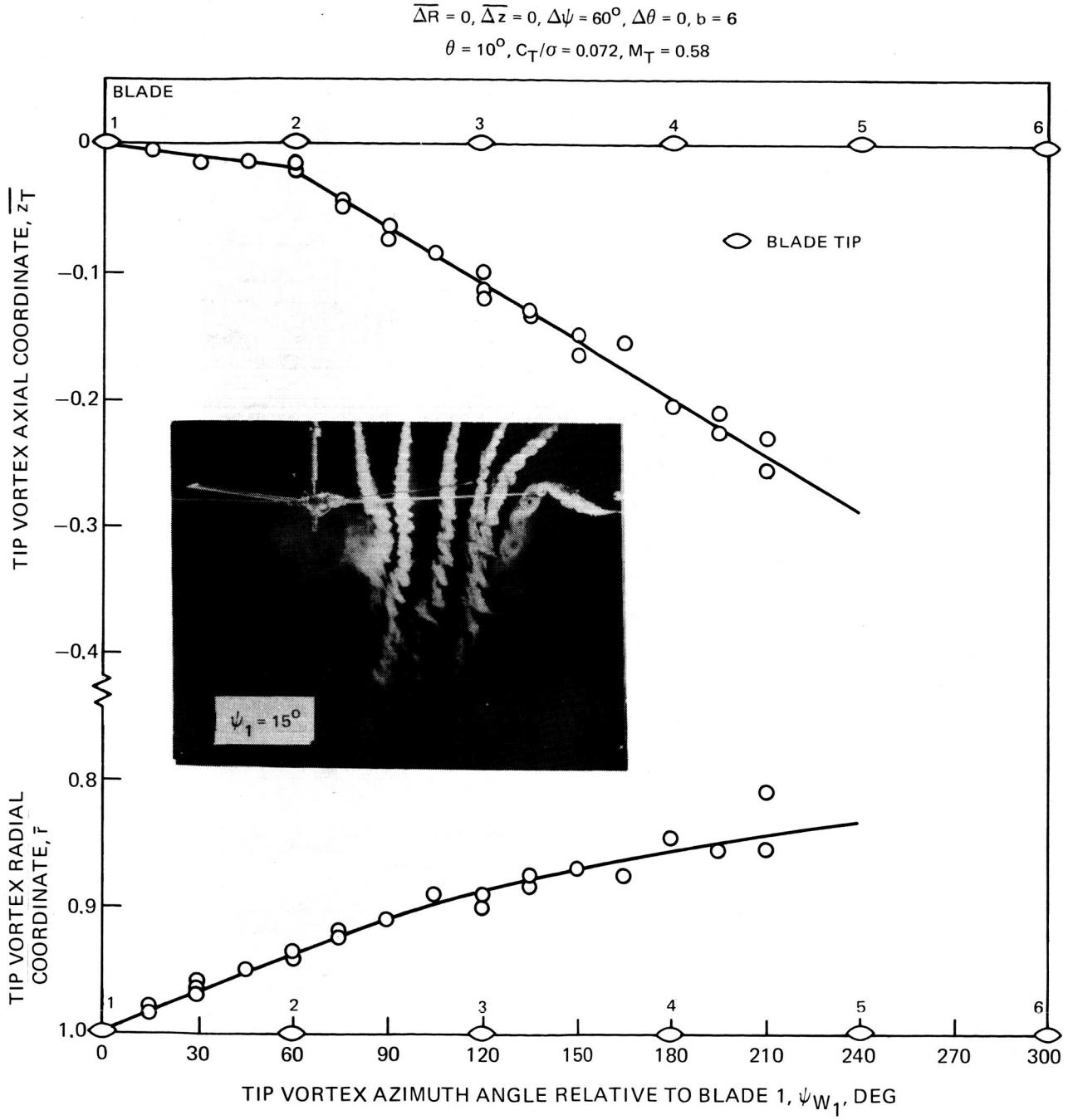

Figure 24. - Tip Vortex Coordinates for a Conventional Six-Bladed Rotor.

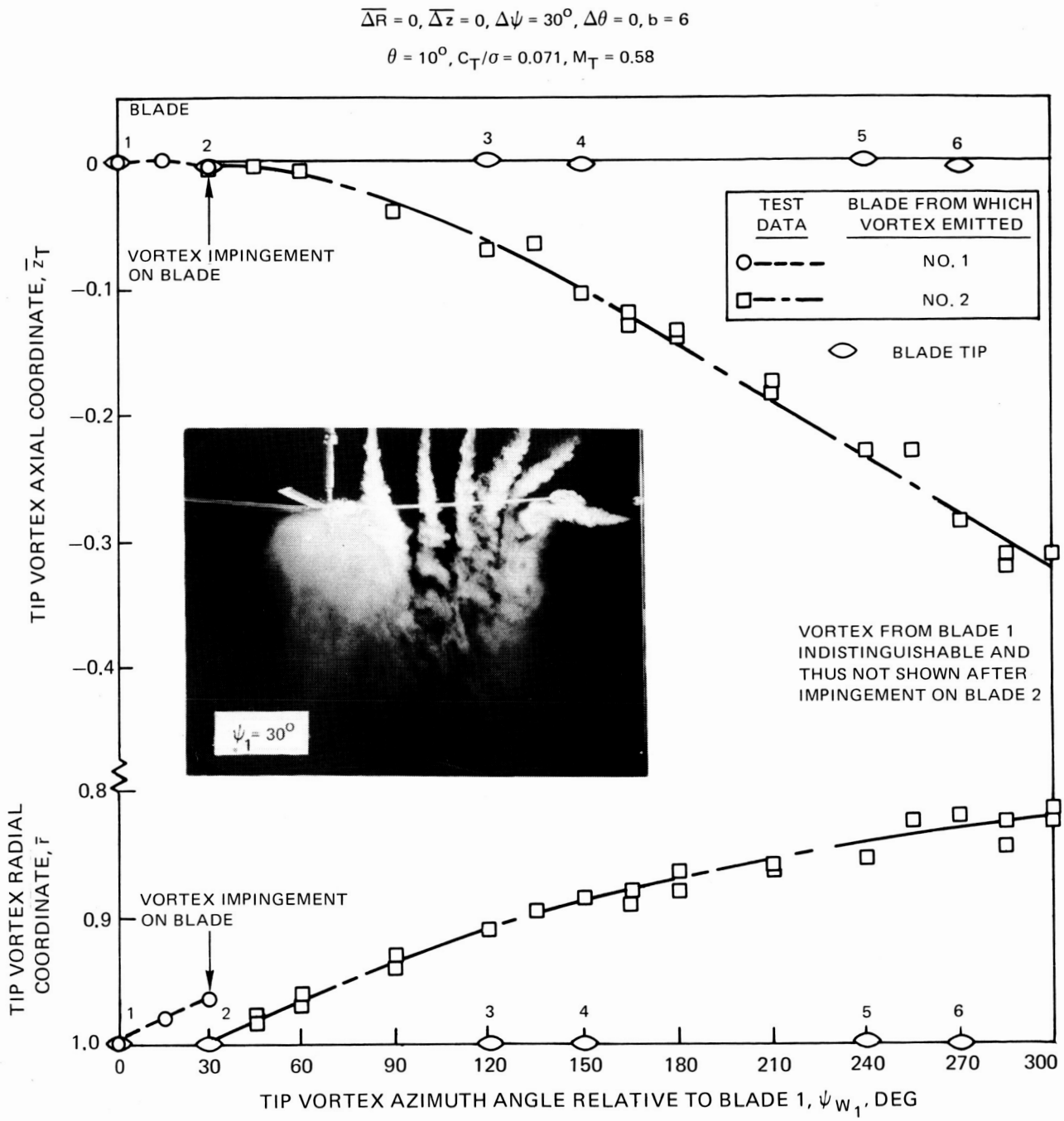

Figure 25. - Tip Vortex Coordinates for an Independent Variation of Blade Azimuth Spacing -- $\Delta\psi$ = 30 deg.

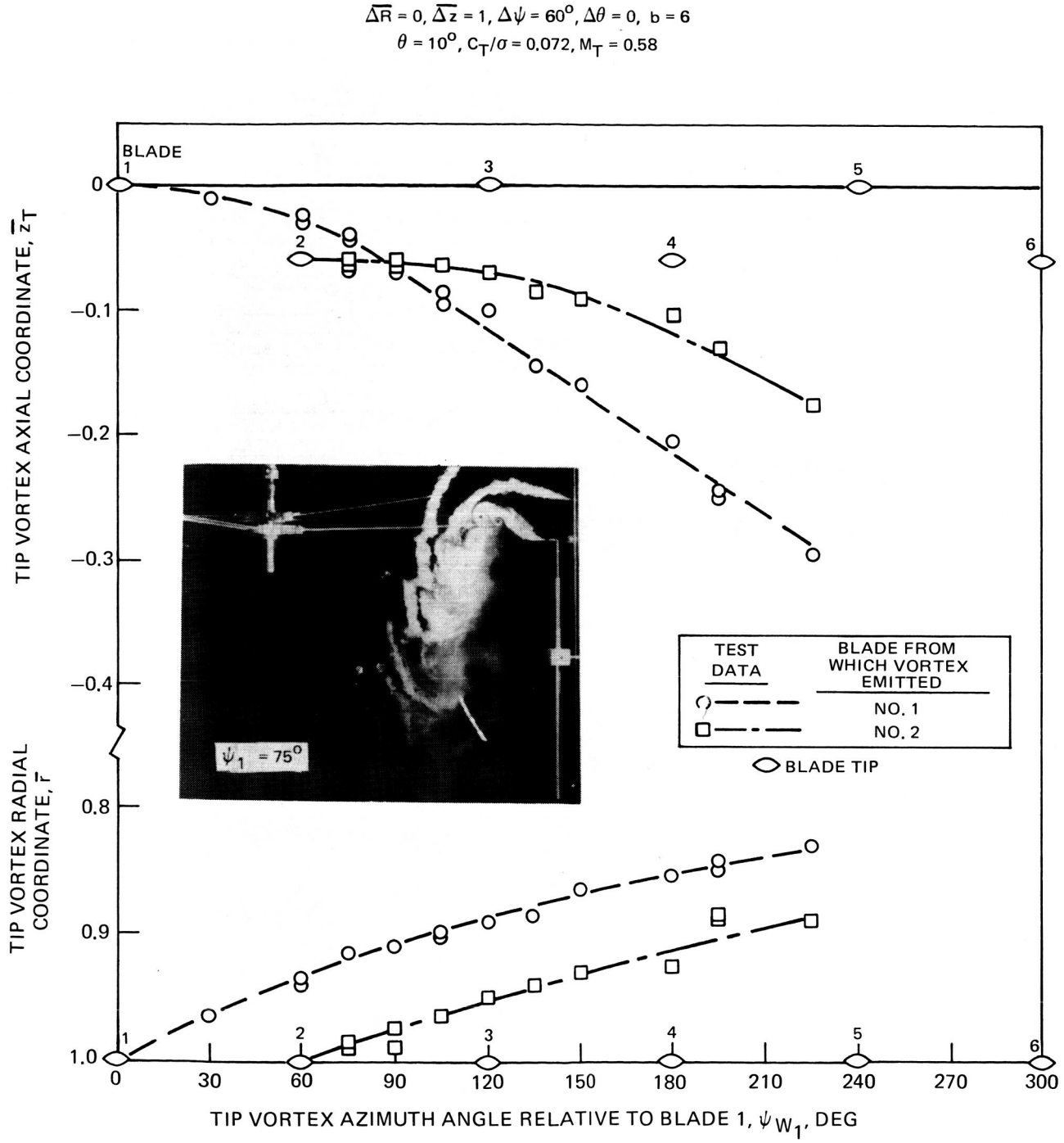

Figure 26. - Tip Vortex Coordinates for an Independent Variation of Blade Azimuth Spacing -- $\overline{\Delta z} = 1$.

$\overline{\Delta R} = 0$, $\overline{\Delta z} = 2$, $\Delta\psi = 60^{o}$, $\Delta\theta = 0$, $b = 6$
$\theta = 10^{o}$, $C_T/\sigma = 0.073$, $M_T = 0.58$

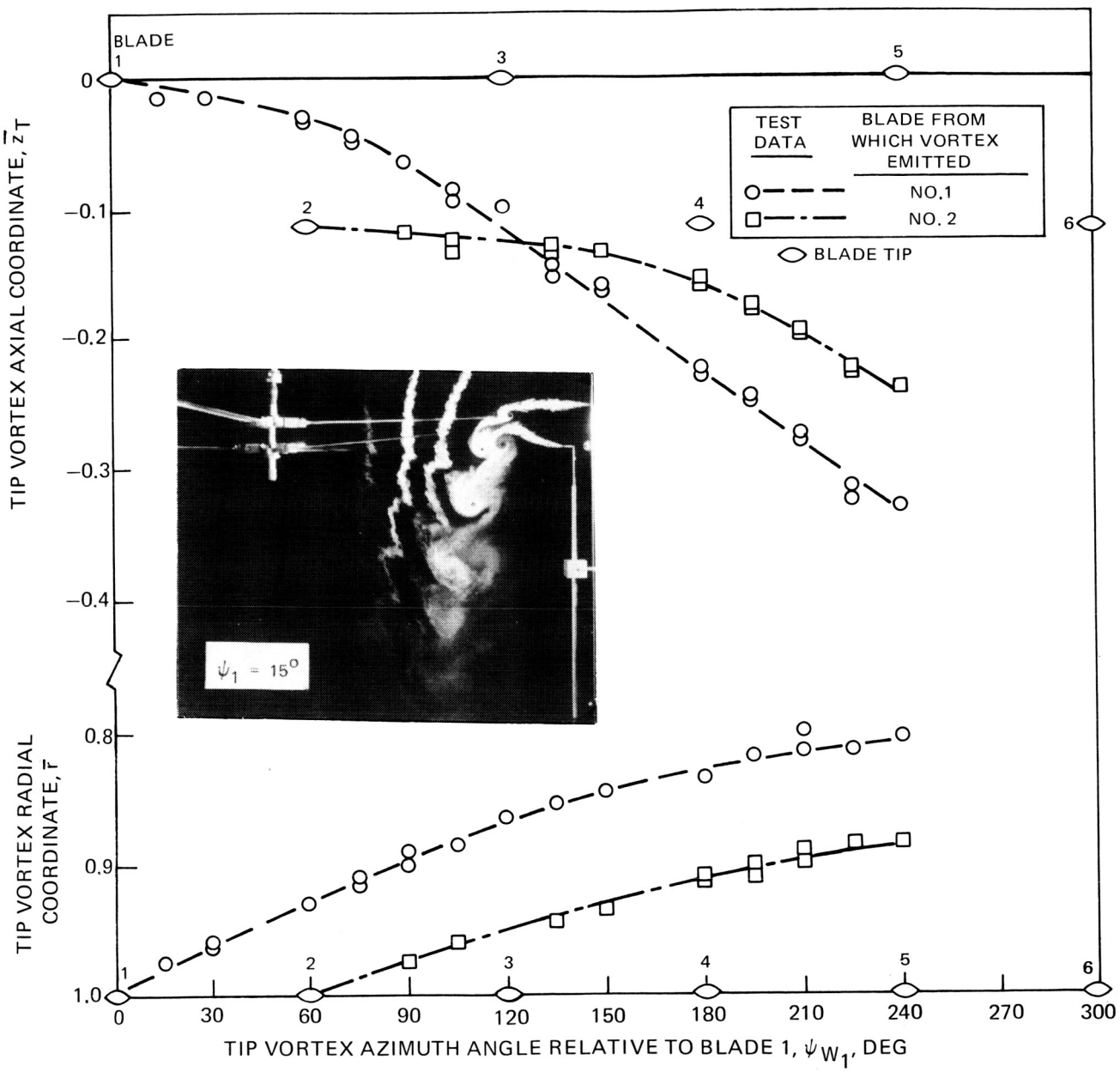

Figure 27. - Tip Vortex Coordinates for an Independent Variation of Blade Axial Spacing -- $\overline{\Delta z} = 2$.

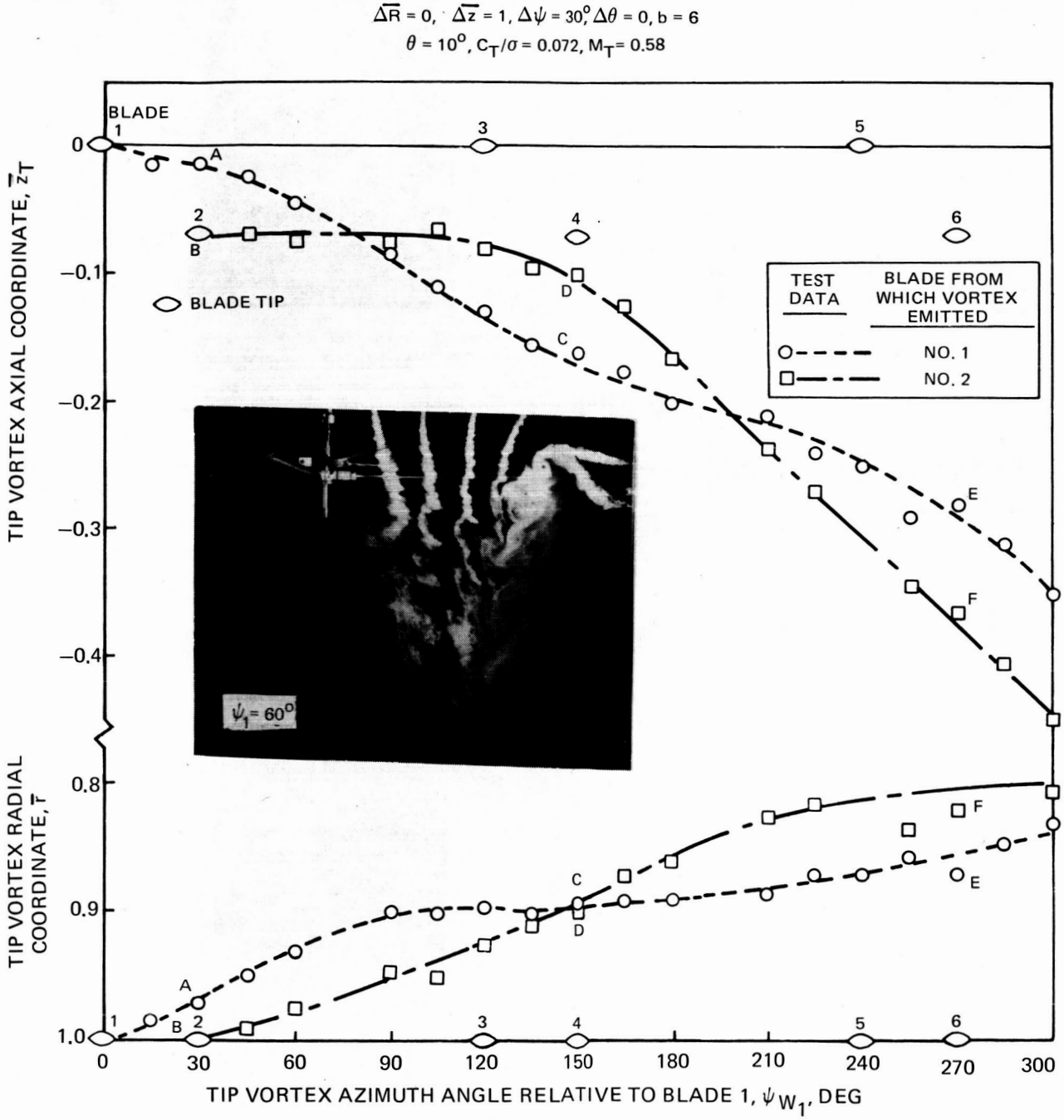

Figure 28. - Tip Vortex Coordinates for a Variable-Geometry Rotor Configuration With Axial and Azimuth Spacing -- $\overline{\Delta z} = 1$, $\Delta\psi = 30$ deg.

$\overline{\Delta R}$ = 0, Δz = 1, $\Delta\psi$ = 30°, $\Delta\theta$ = 0, b = 6

θ = 10°, C_T/σ = 0.072, M_T = 0.58

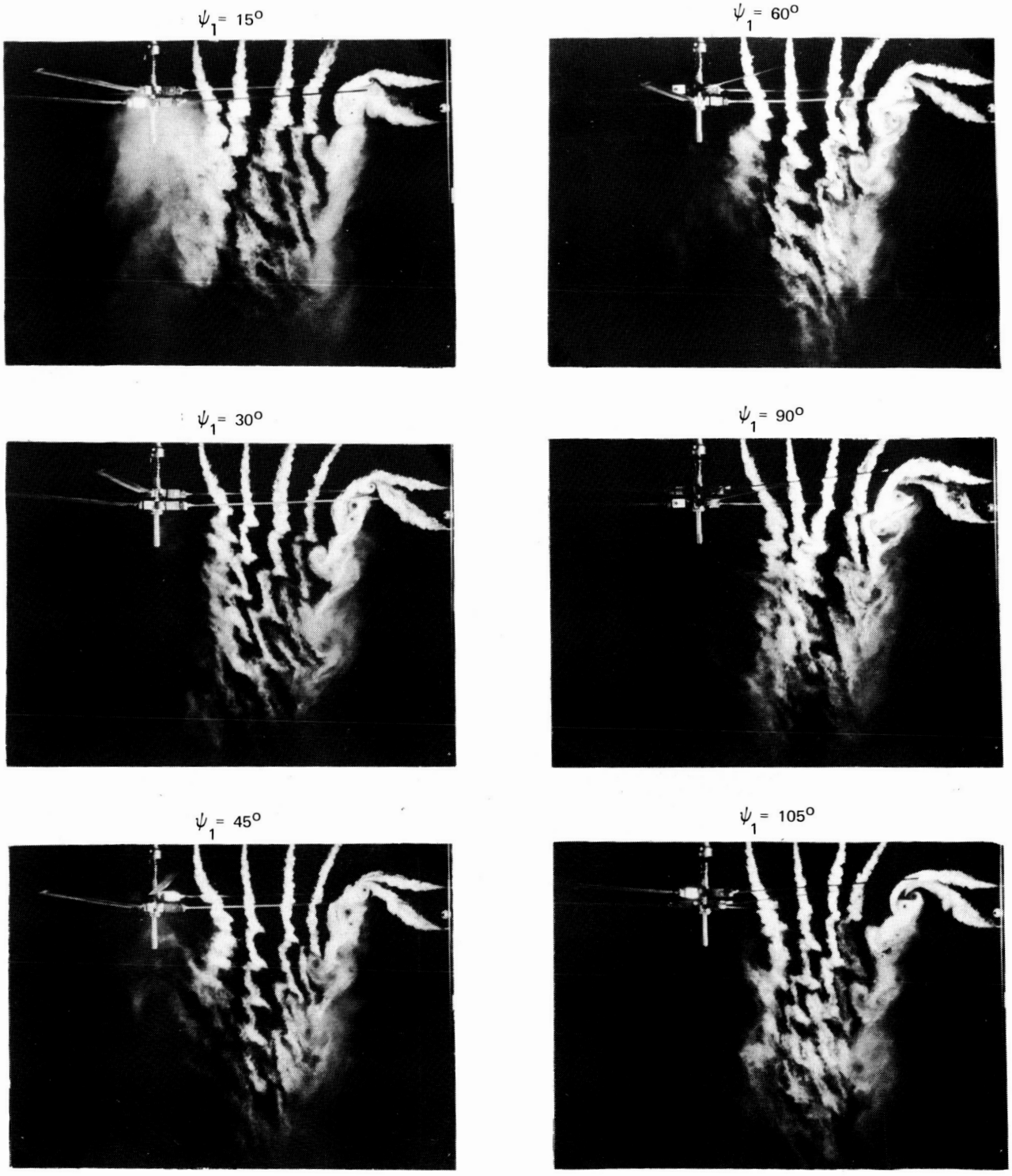

Figure 29. - Sequence of Flow Visualization Photographs Showing the Time History of the Wake for a Variable-Geometry Rotor Configuration With Axial and Azimuth Spacing -- $\overline{\Delta z}$ = 1, $\Delta\psi$ = 30 deg.

$\overline{\Delta R} = 0$, $\overline{\Delta z} = 1$, $\Delta\psi = 30^{o}$, $\Delta\theta = 0$
$\theta = 10^{o}$, $C_T/\sigma = 0.072$, $M_T = 0.58$

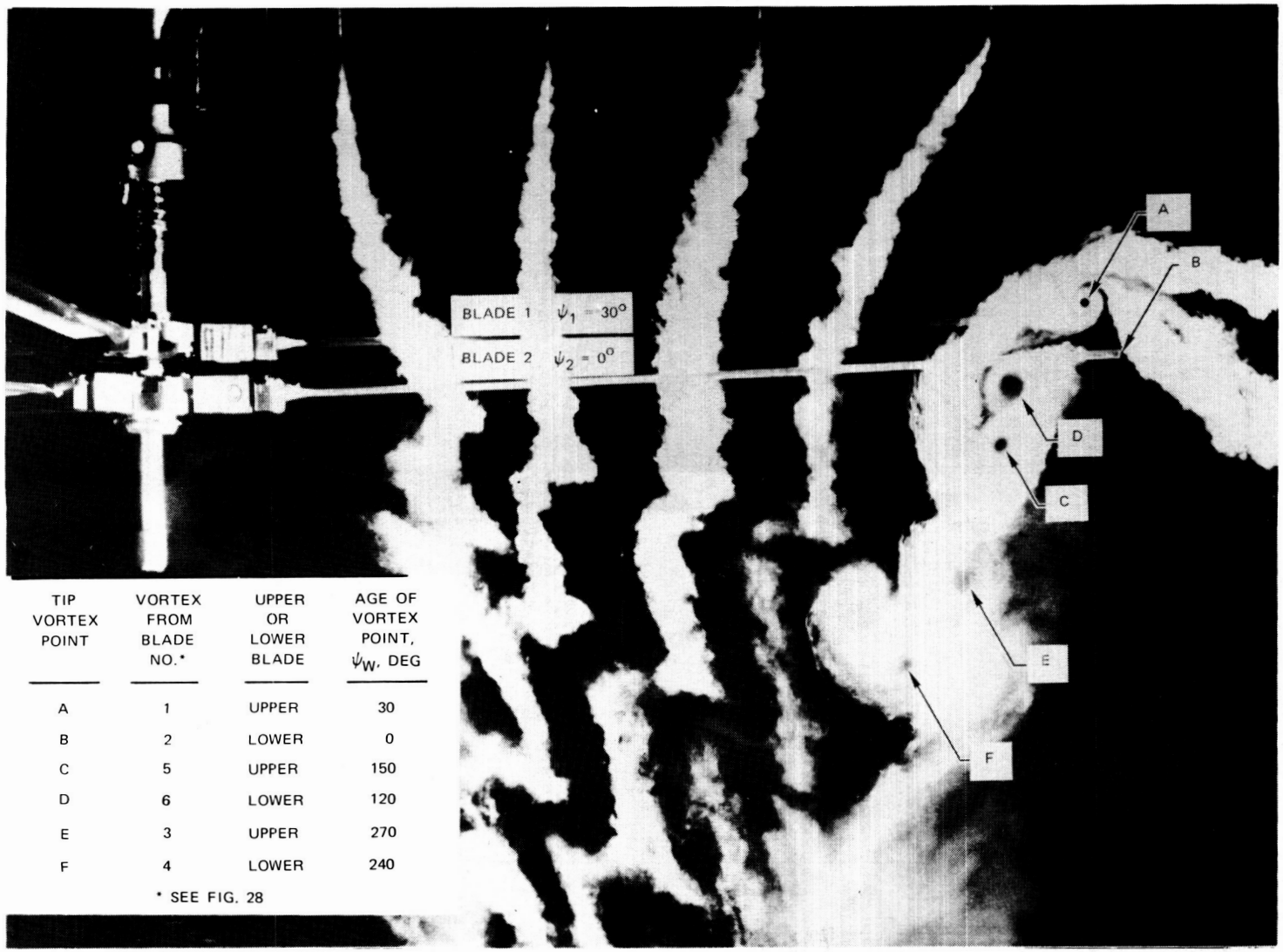

TIP VORTEX POINT	VORTEX FROM BLADE NO.*	UPPER OR LOWER BLADE	AGE OF VORTEX POINT, ψ_W, DEG
A	1	UPPER	30
B	2	LOWER	0
C	5	UPPER	150
D	6	LOWER	120
E	3	UPPER	270
F	4	LOWER	240

* SEE FIG. 28

Figure 30. - Flow Visualization Photograph for Variable-Geometry-Rotor Configuration With Axial and Azimuth Spacing -- $\overline{\Delta z} = 1$, $\Delta\psi = 30$ deg.

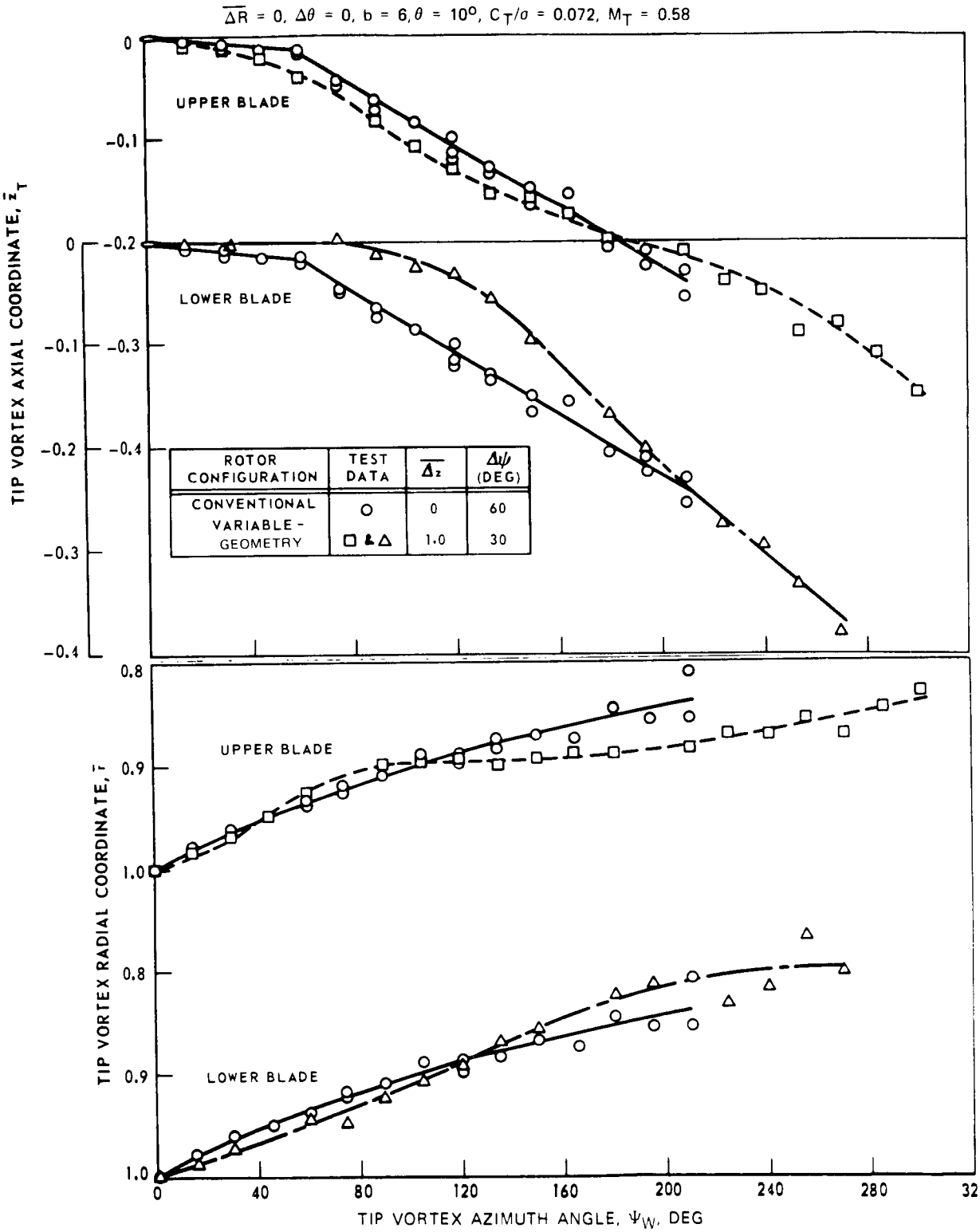

Figure 31. - Comparisons of Tip Vortex Coordinates of a Variable-Geometry Rotor Configuration ($\overline{\Delta z}$ = 1, $\Delta\psi$ = 30 deg) With Conventional Rotor Coordinates.

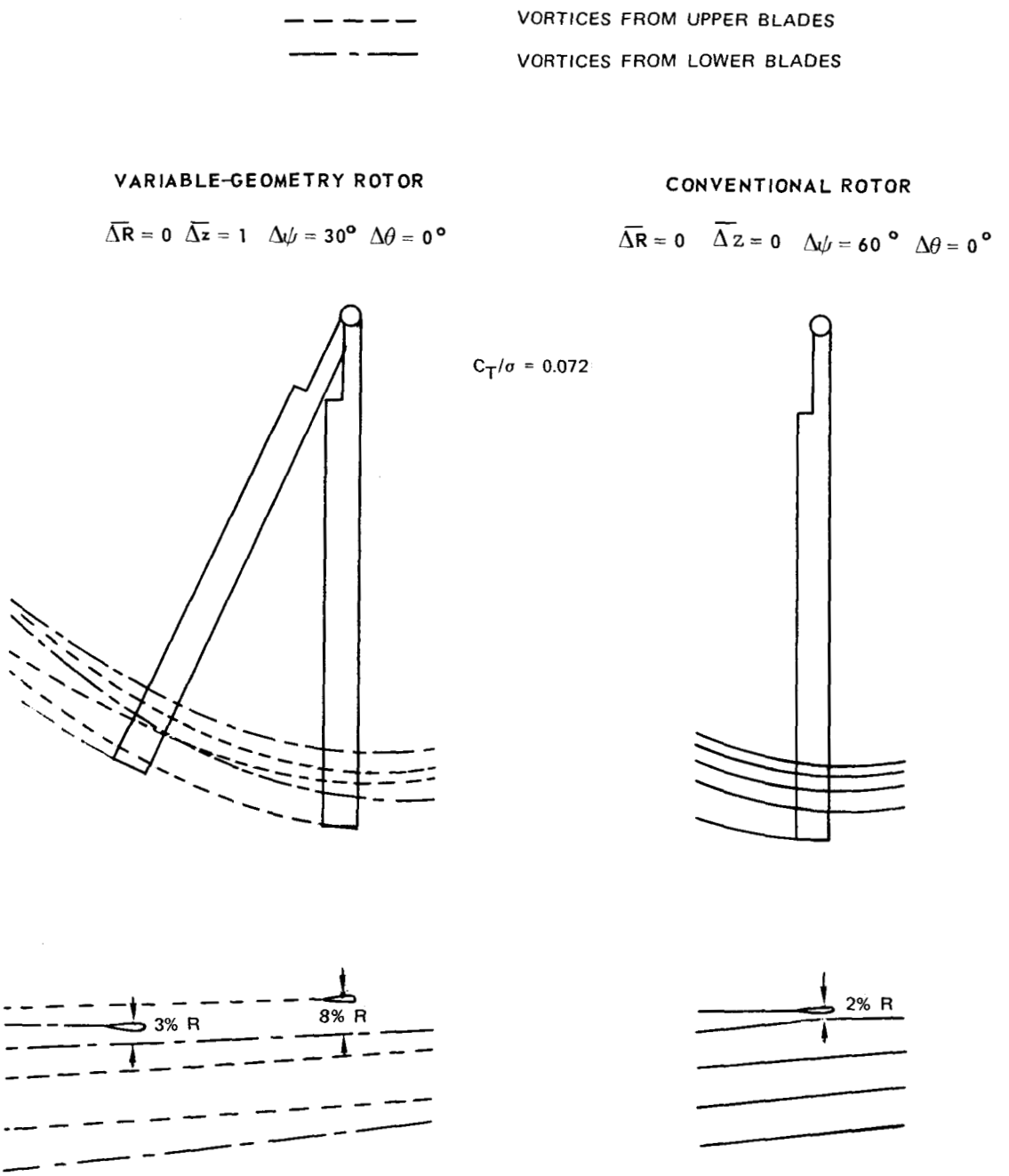

Figure 32. - Comparison of Blade-Vortex Positions of a Variable-Geometry Rotor ($\overline{\Delta z} = 1$, $\Delta\psi = 30$ deg) and a Conventional Rotor.

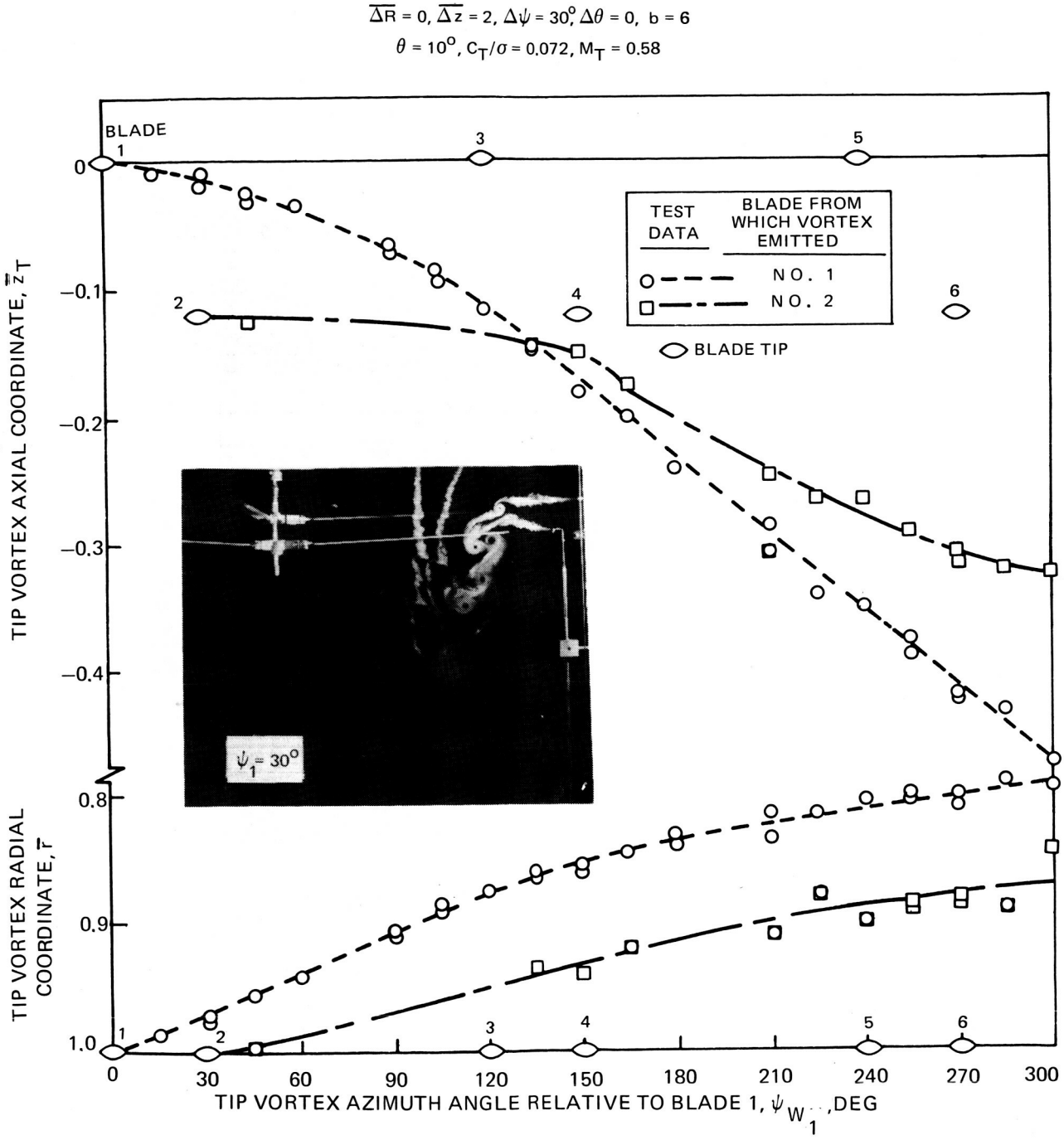

Figure 33. - Tip Vortex Coordinates for a Variable-Geometry Rotor Configuration With Axial and Azimuth Spacing -- $\overline{\Delta z} = 2$, $\Delta\psi = 30$ deg.

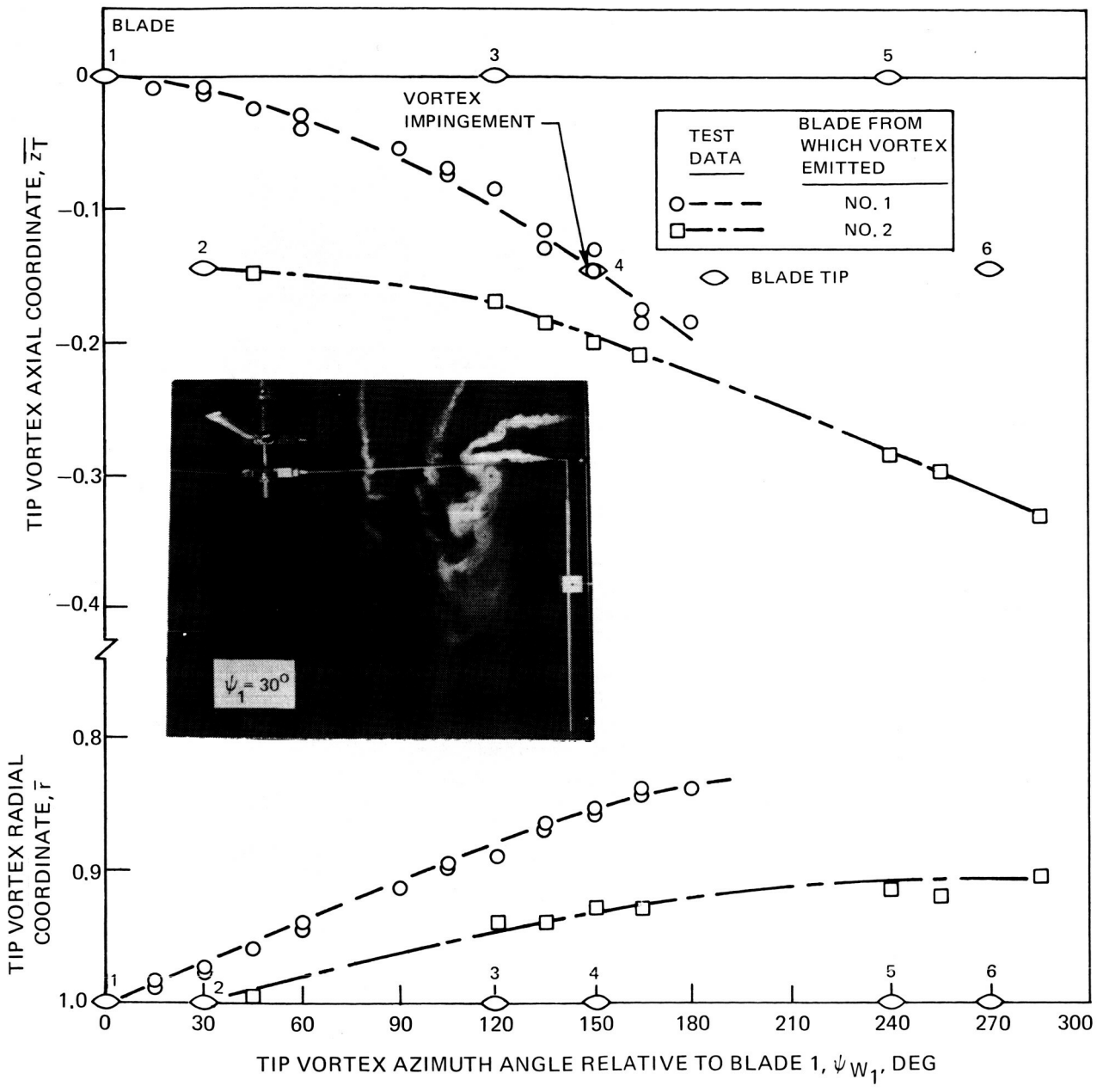

Figure 34. - Tip Vortex Coordinates for a Variable-Geometry Rotor Configuration With Axial and Azimuth Spacing -- $\overline{\Delta z}$ = 2.5, $\Delta\psi$ = 30 deg.

$\overline{\Delta R} = 0, \overline{\Delta z} = 1, \Delta\psi = 0, \Delta\theta = 0, b = 6$

$\theta = 10^{o}, C_T/\sigma = 0.067, M_T = 0.58$

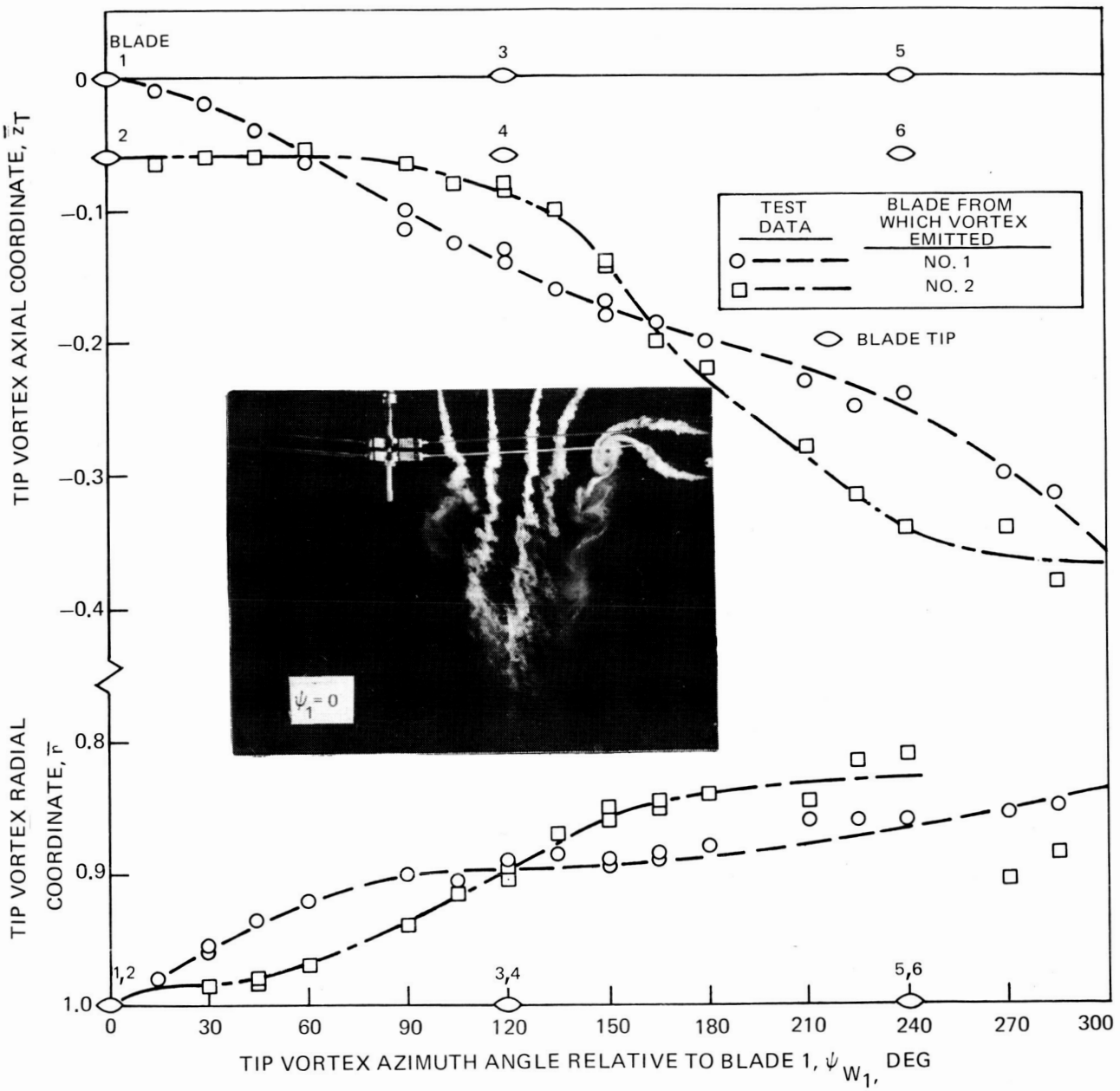

Figure 35. - Tip Vortex Coordinates for a Biplane Configuration With an Axial Spacing of One Chord Length.

$\overline{\Delta R} = 0, \overline{\Delta z} = 2, \Delta\psi = 0, \Delta\theta = 0, b = 6$

$\theta = 10^{o}, C_T/\sigma = 0.071, M_T = 0.58$

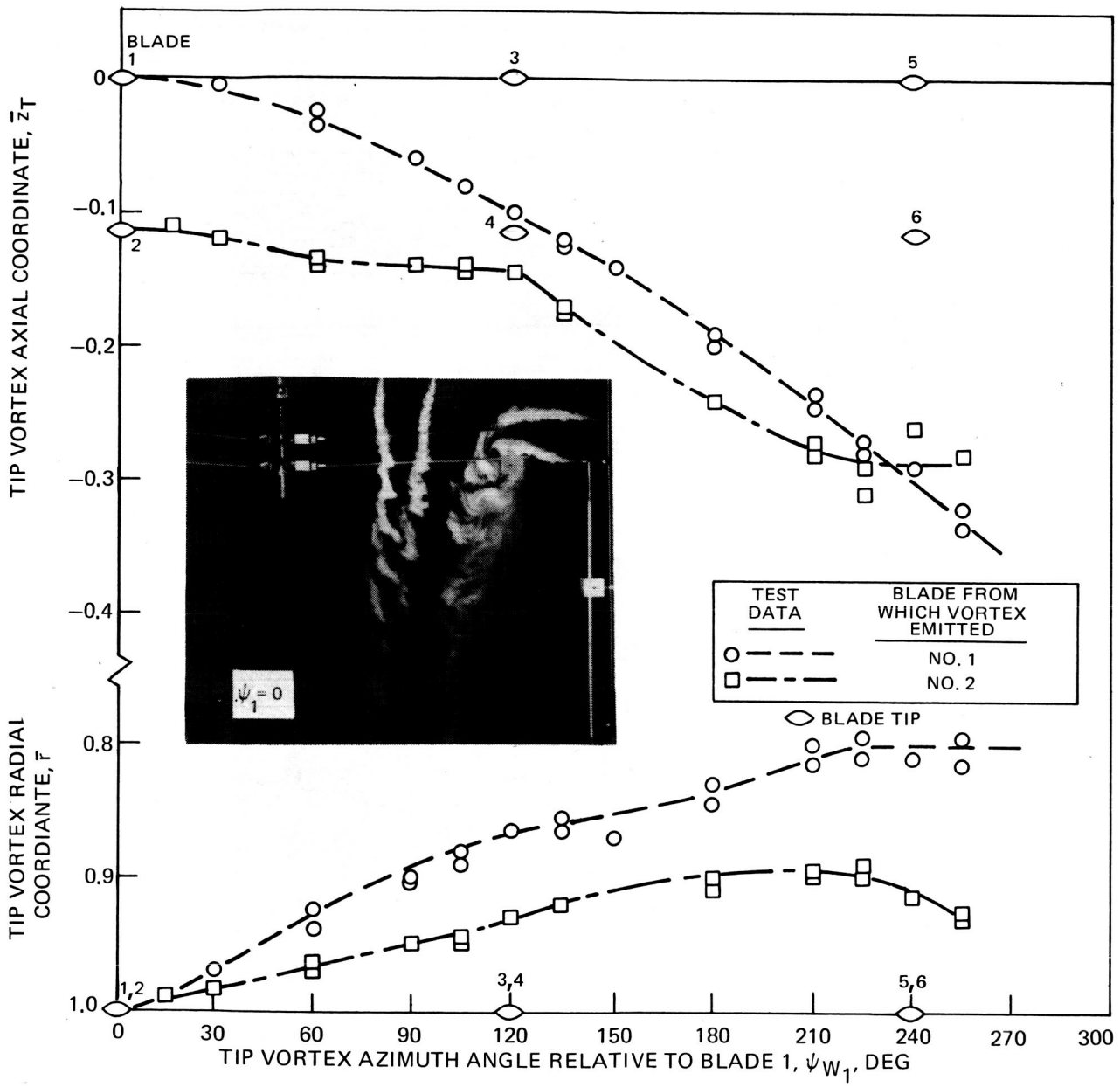

Figure 36. - Tip Vortex Coordinates for a Biplane Configuration With an Axial Spacing of Two Chord Lengths.

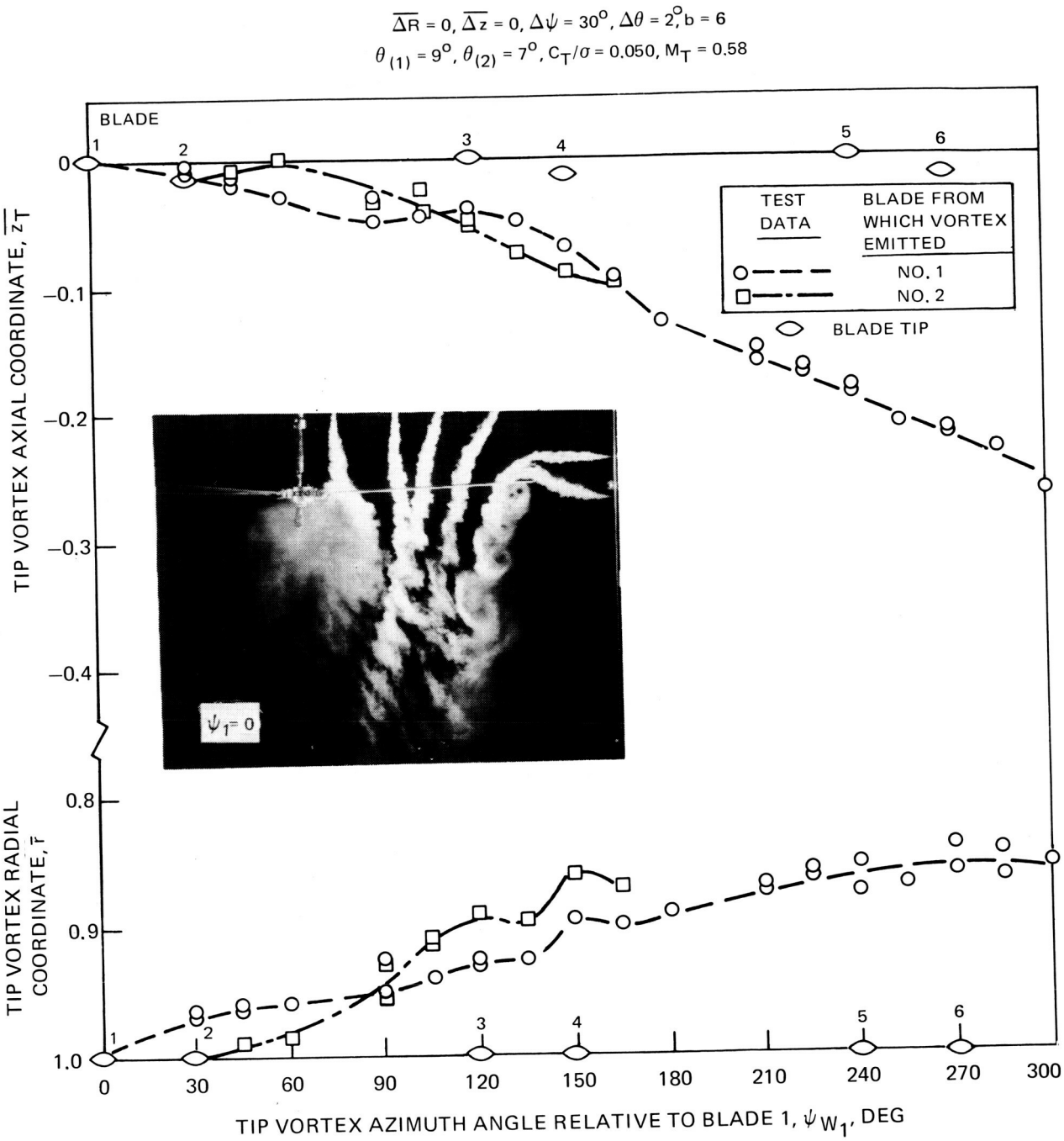

Figure 37. - Tip Vortex Coordinates for a Variable-Geometry Rotor Configuration With Differential Collective Pitch.

$\overline{\Delta R} = 0.15$, $\overline{\Delta z} = 0$, $\Delta\psi = 60^{o}$, $\Delta\theta = 0$, b = 6
$\theta = 10^{o}$, $C_T/\sigma = 0.060$, $M_T = 0.58$

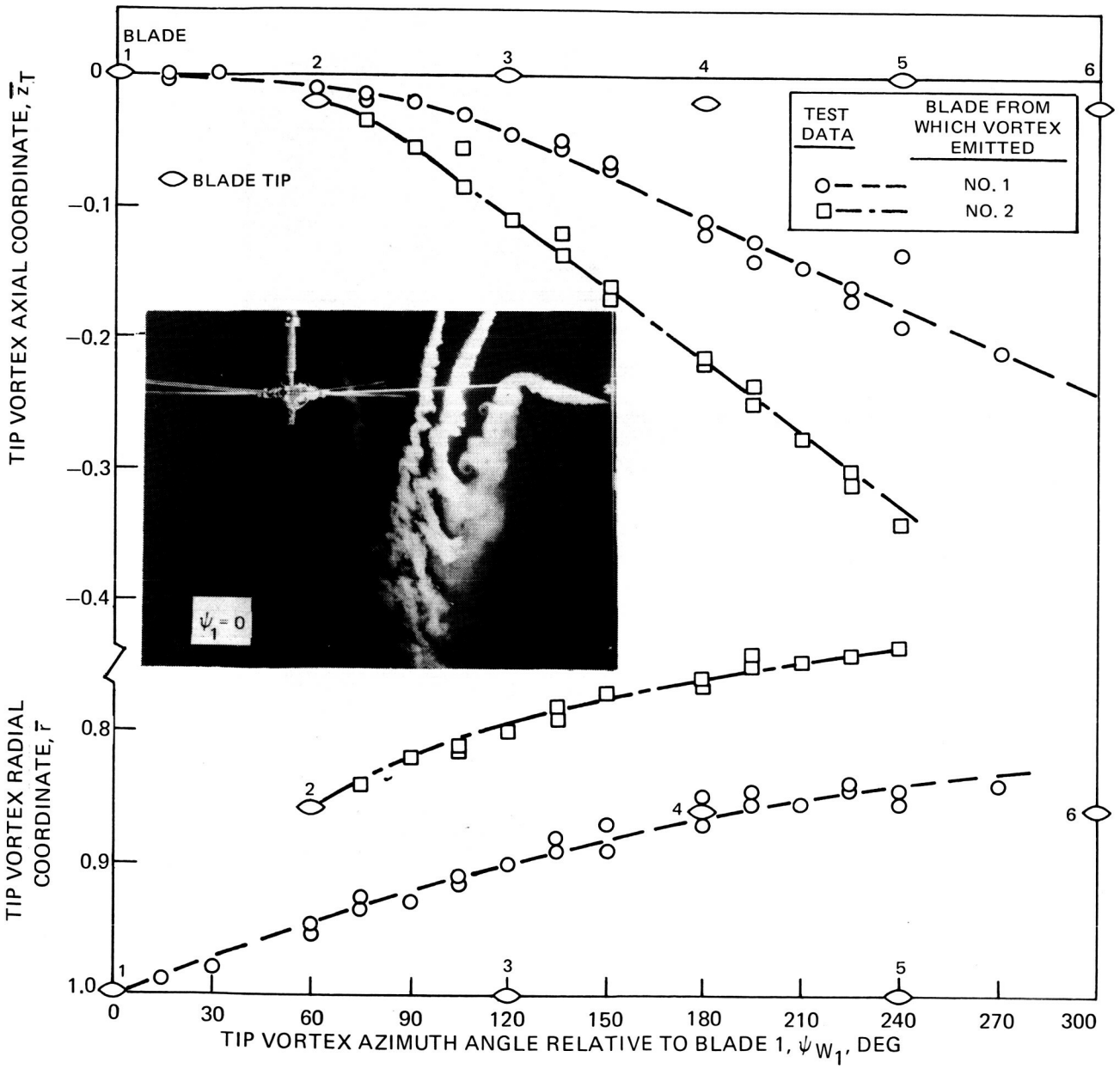

Figure 38. - Tip Vortex Coordinates for an Independent Variation of Radius Increment Ratio -- $\overline{\Delta R} = 0.15$.

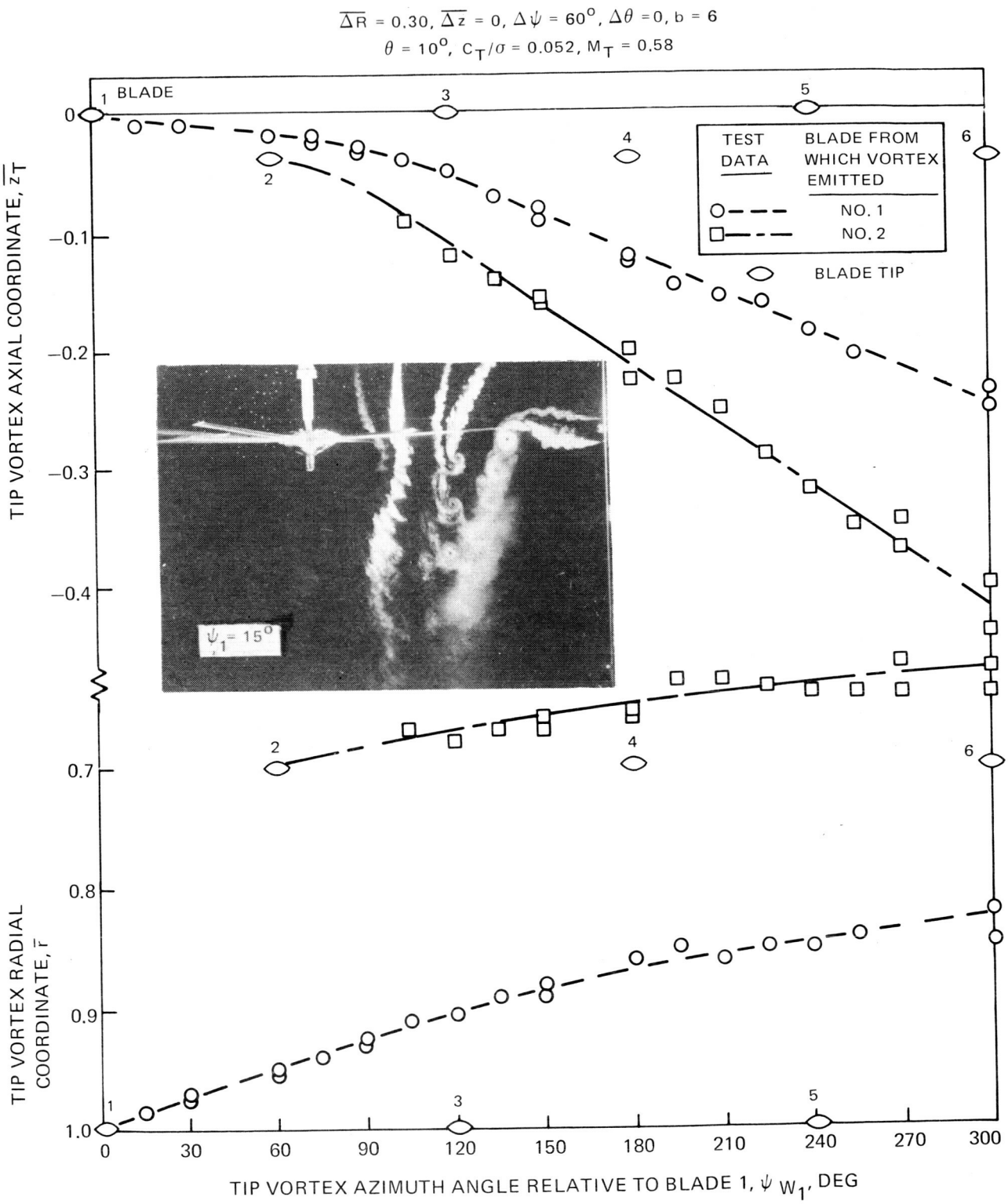

Figure 39. - Tip Vortex Coordinates for an Independent Variation of Radius Increment Ratio -- $\overline{\Delta R}$ = 0.30.

$\overline{\Delta R} = 0$, $\overline{\Delta z} = 1$, $\Delta\psi = -30^{o}$, $\Delta\theta = 0$, $\theta = 10^{o}$, $\psi_{(1)} = 30^{o}$

$\overline{\Delta R} = 0.15$, $\overline{\Delta z} = 0$, $\Delta\psi = -30^{o}$, $\Delta\theta = 0$, $\theta = 8^{o}$, $\psi_{(1)} = 30^{o}$

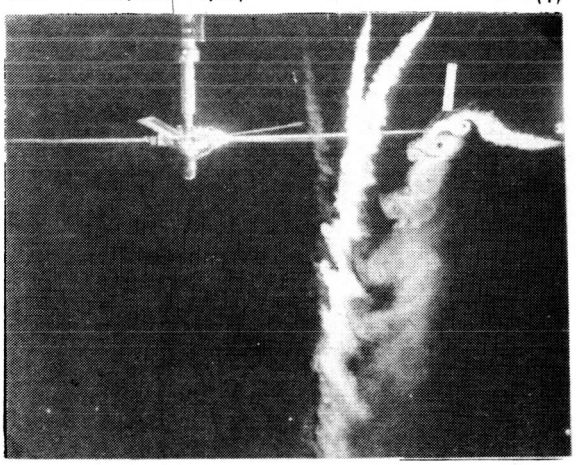

$\overline{\Delta R} = 0$, $\overline{\Delta z} = 2.5$, $\Delta\psi = 30^{o}$, $\Delta\theta = 0$, $\theta = 8^{o}$, $\psi_{(1)} = 60^{o}$

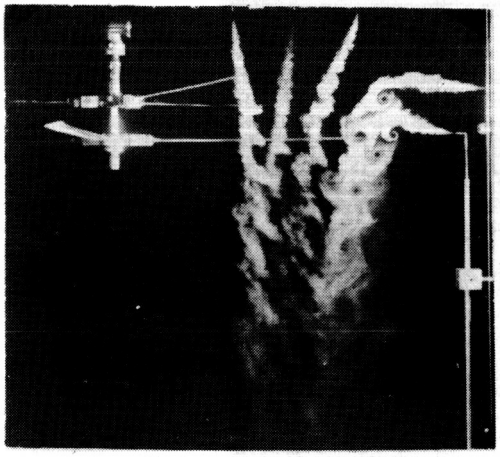

$\overline{\Delta R} = -0.15$, $\overline{\Delta z} = 2$, $\Delta\psi = 60^{o}$, $\Delta\theta = 0$, $\theta = 10^{o}$, $\psi_{(1)} = 60^{o}$

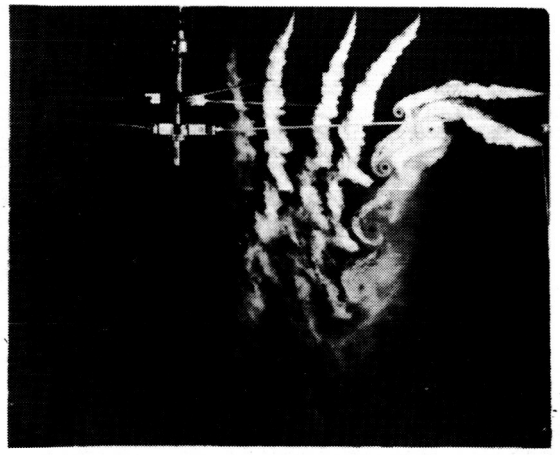

$\overline{\Delta R} = 0$, $\overline{\Delta z} = 0$, $\Delta\psi = 60^{o}$, $\Delta\theta = 2^{o}$, $\theta_{(1)} = 11^{o}$, $\theta_{(2)} = 9^{o}$, $\psi_{(1)} = 15^{o}$

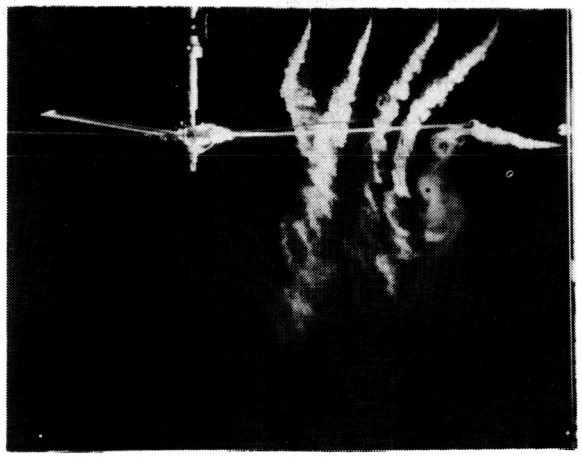

$\overline{\Delta R} = 0.15$, $\overline{\Delta z} = 0$, $\Delta\psi = 60^{o}$, $\Delta\theta = -2.5^{o}$, $\theta_{(1)} = 8^{o}$, $\theta_{(2)} = 10.5^{o}$, $\psi_{(1)} = 0$

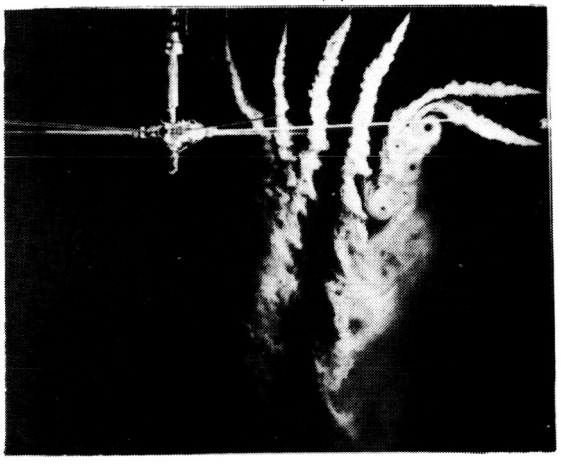

Figure 40. - Flow Visualization Photographs for Selected VGR Configurations.

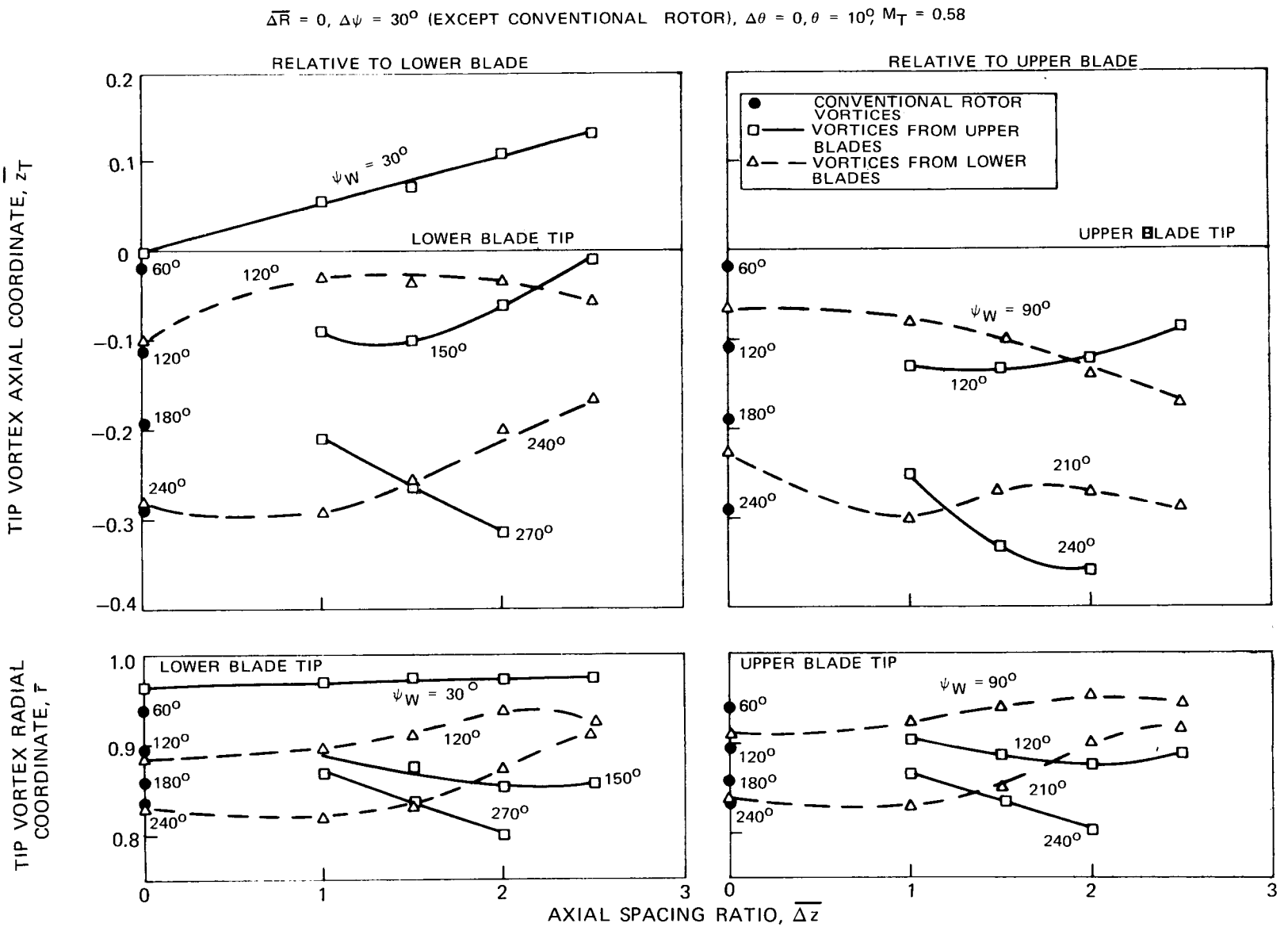

Figure 41. - Effect of Axial Spacing on Tip Vortex Coordinates.

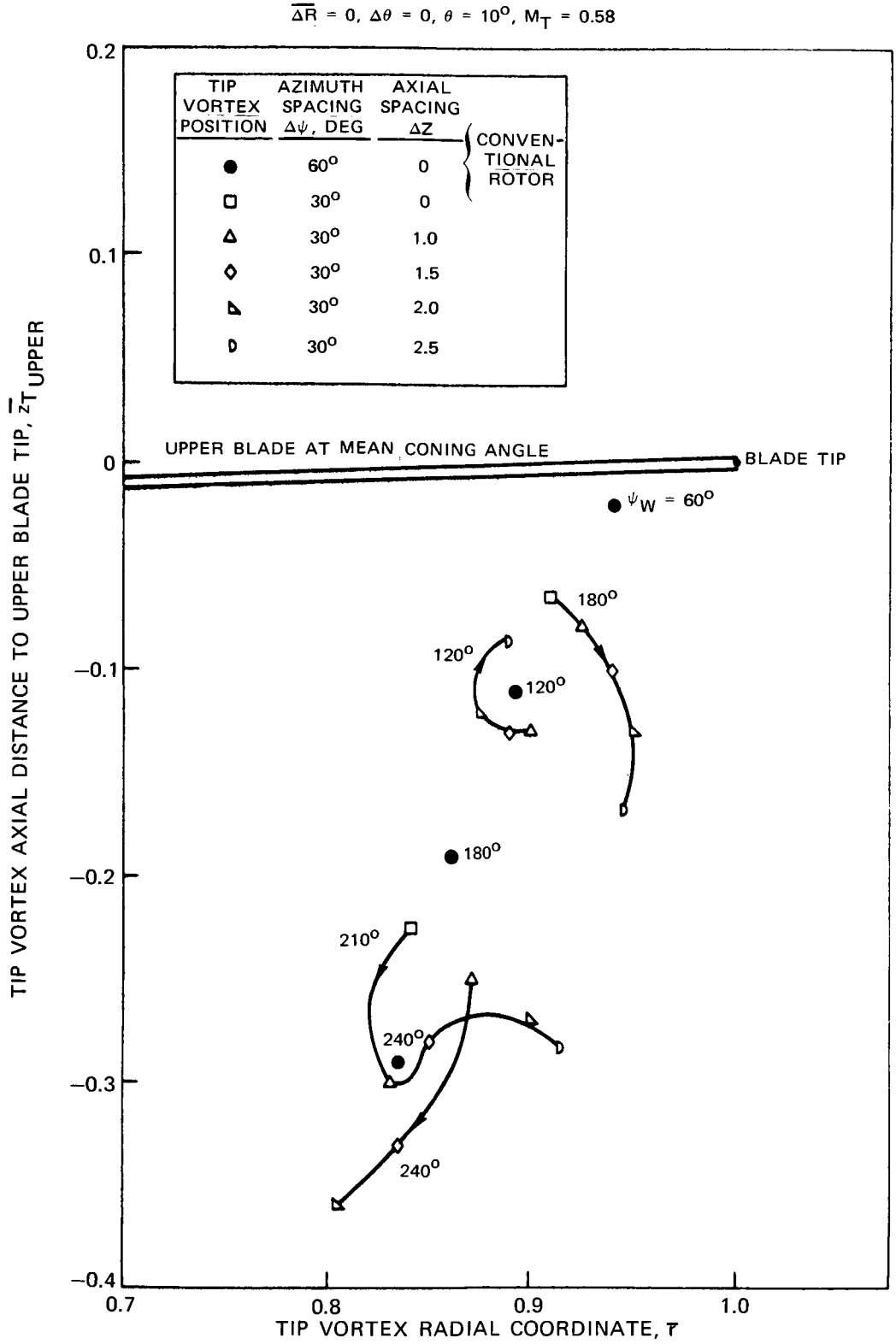

(a) - At Upper Blade.

Figure 42. - Effect of Axial Spacing on Tip Vortex Positions Relative to the Blades.

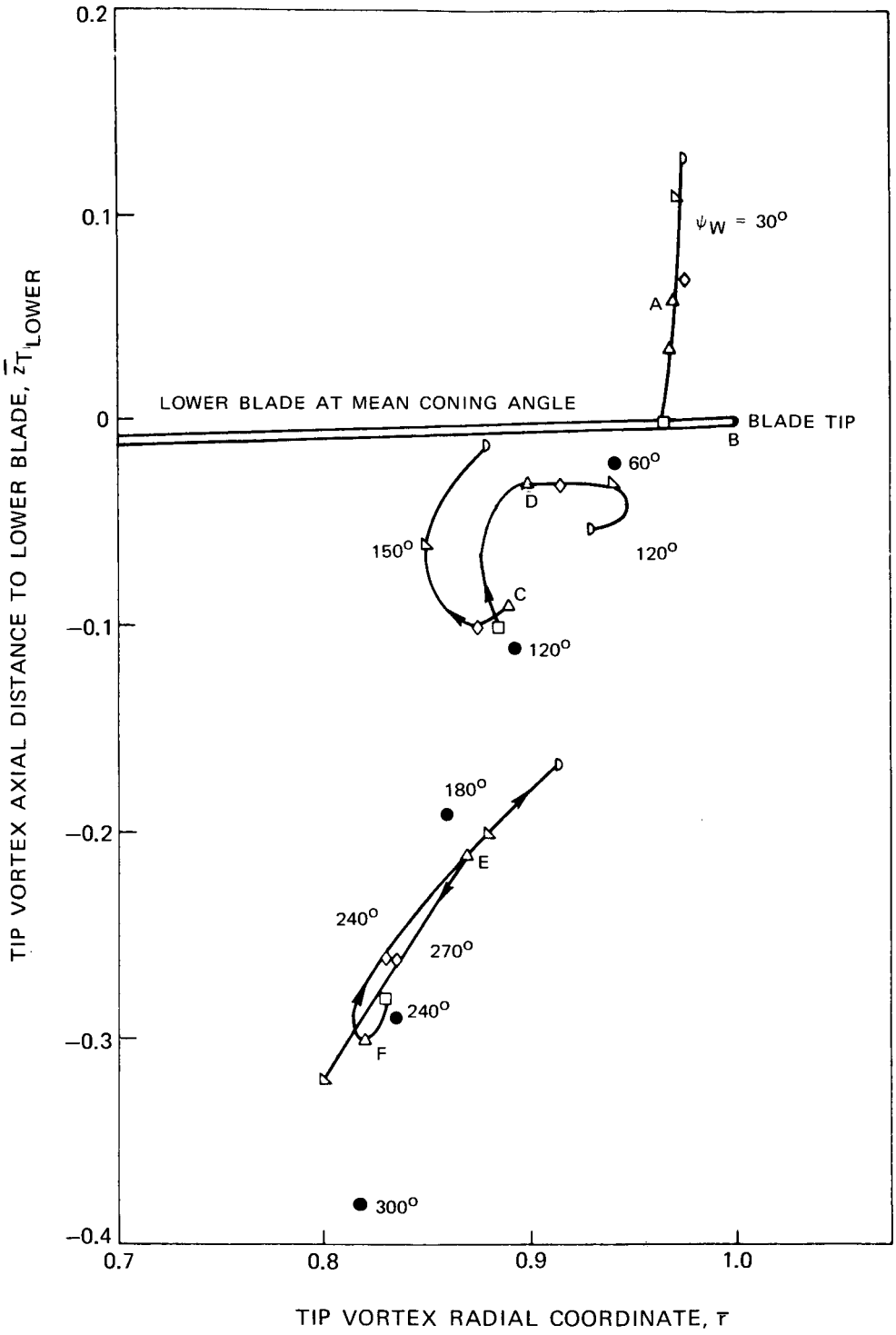

(b) - At Lower Blade.

Figure 42. - Concluded.

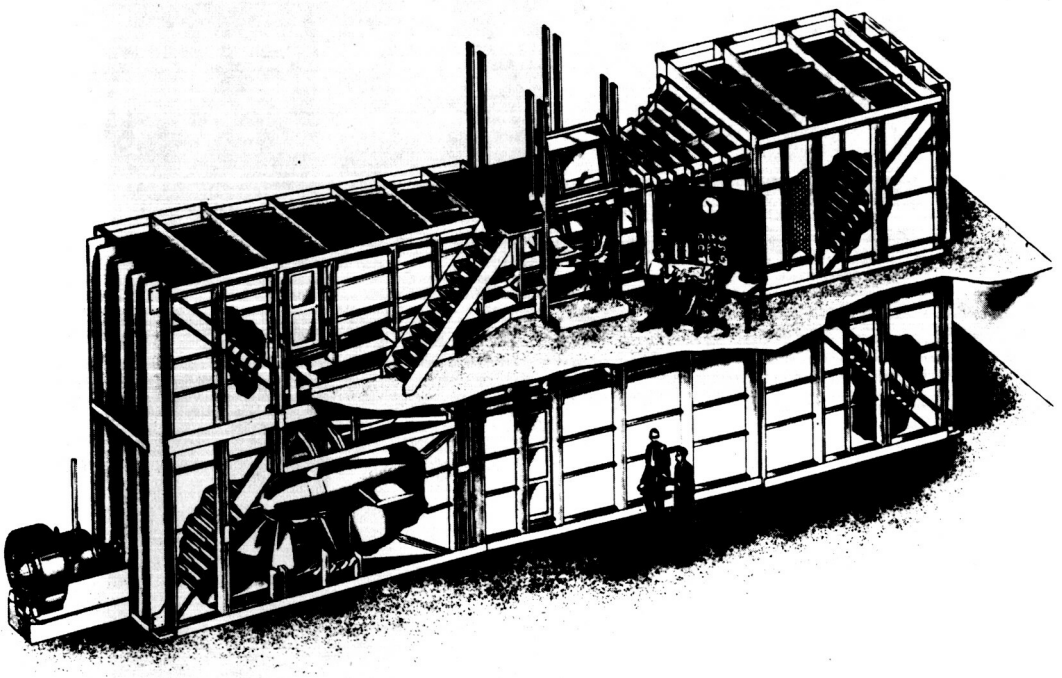

Figure 43. - UARL 4 x 6 ft Subsonic Wind Tunnel.

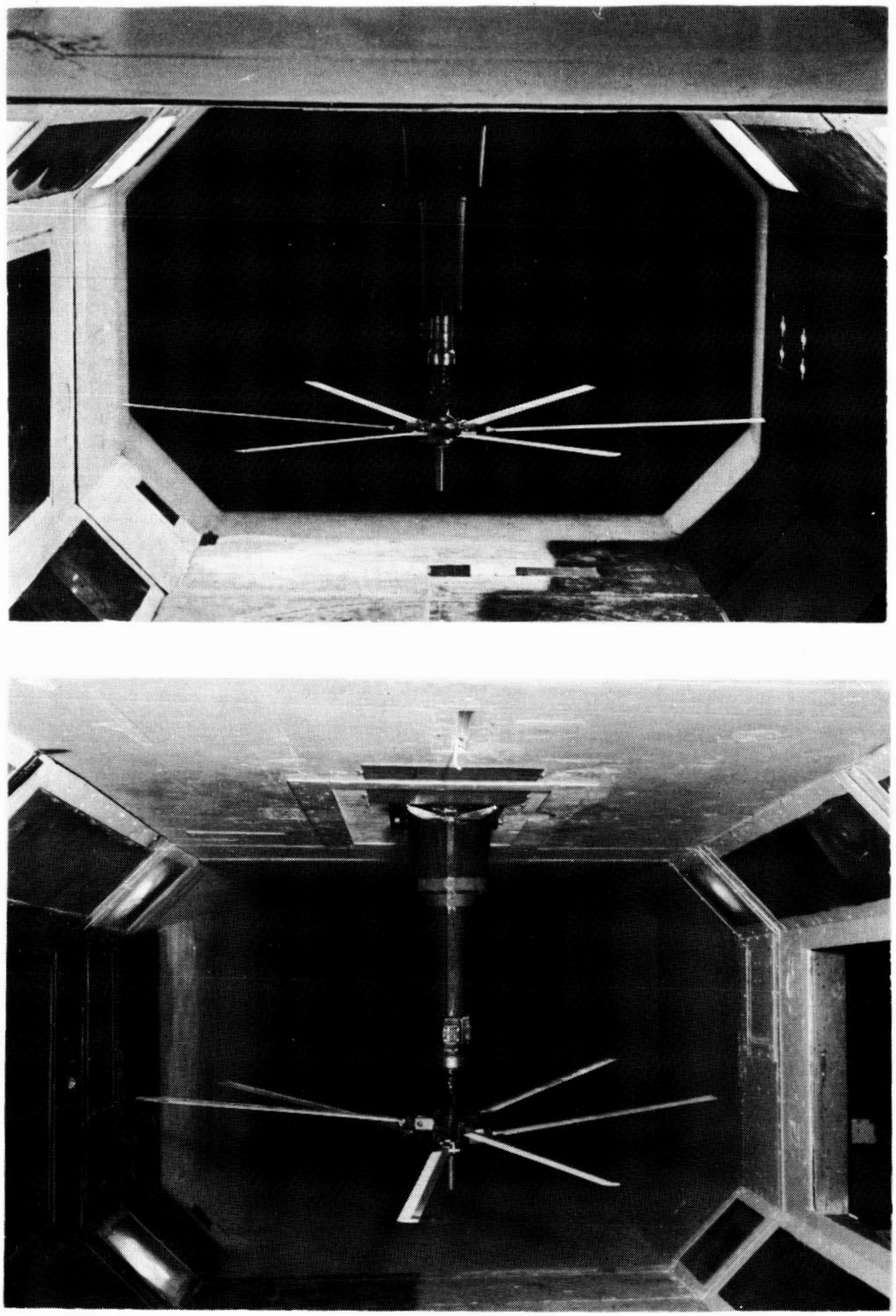

Figure 44. - Conventional and Variable-Geometry Rotors in Wind Tunnel.

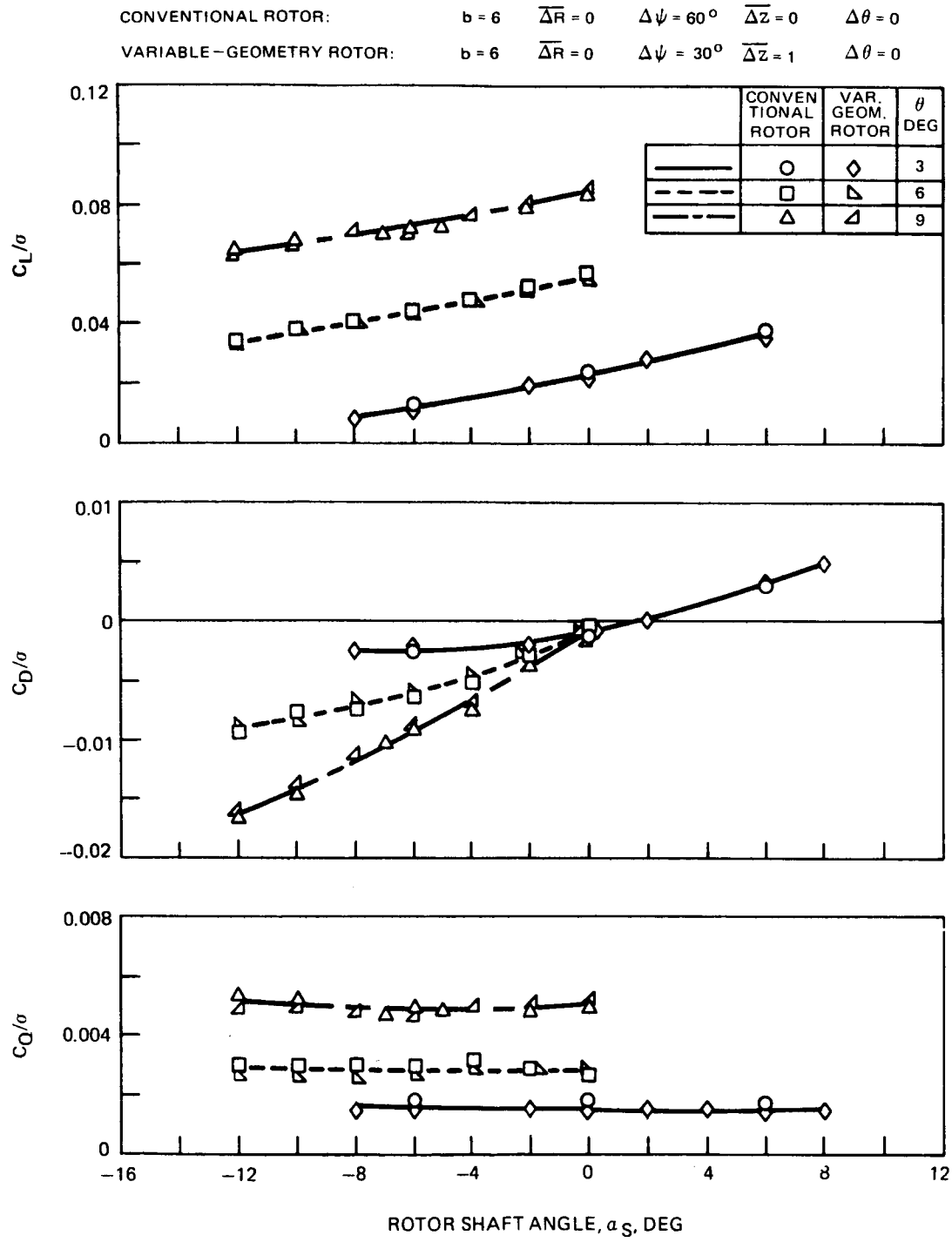

(a) - Advance ratio, μ = 0.1.

Figure 45. - Effect of Axial and Azimuth Spacing on Forward Flight Performance -- $\overline{\Delta z}$ = 1, $\Delta\psi$ = 30°.

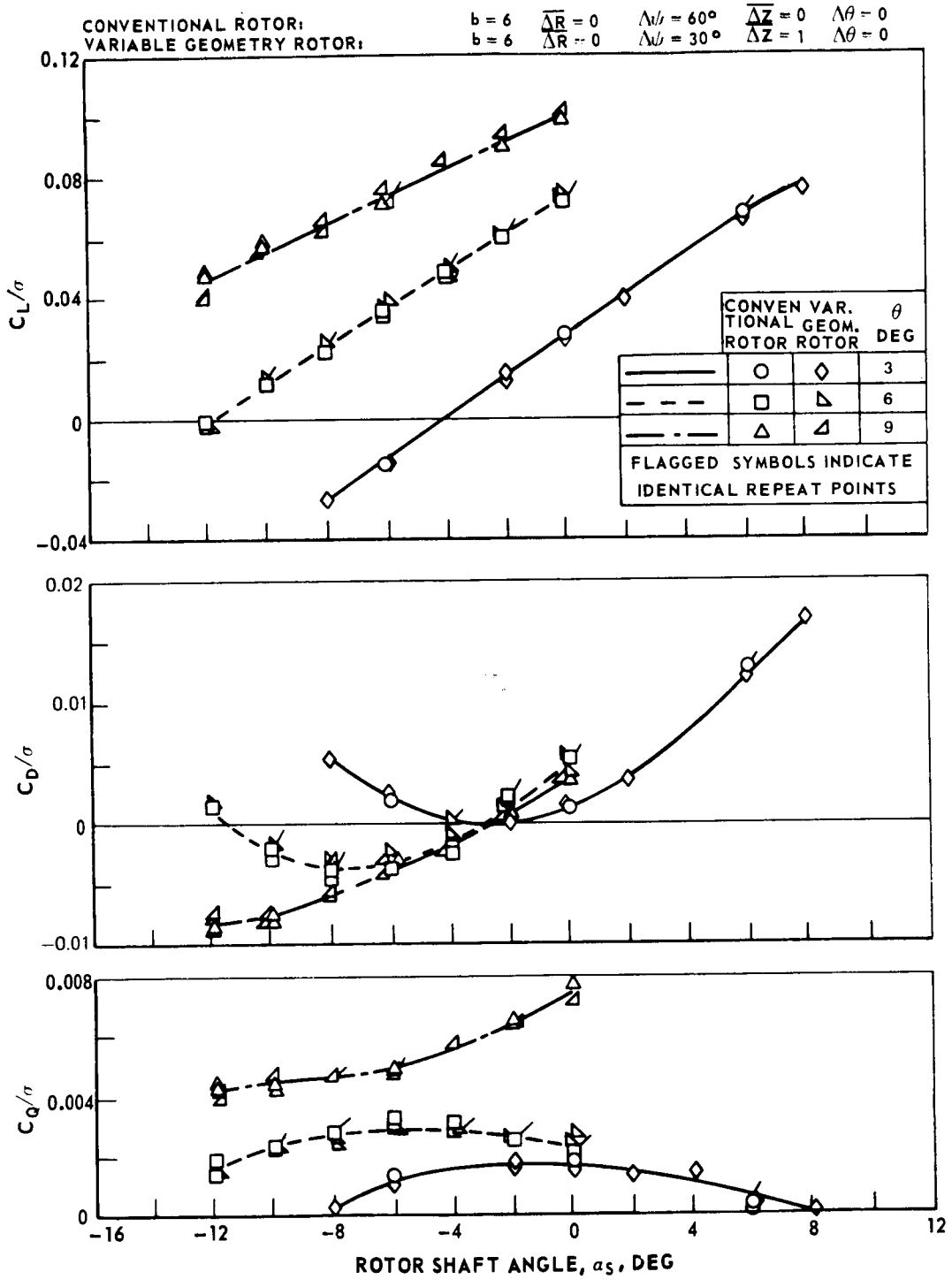

(b) - Advance Ratio, = 0.3.

Figure 45. - Continued.

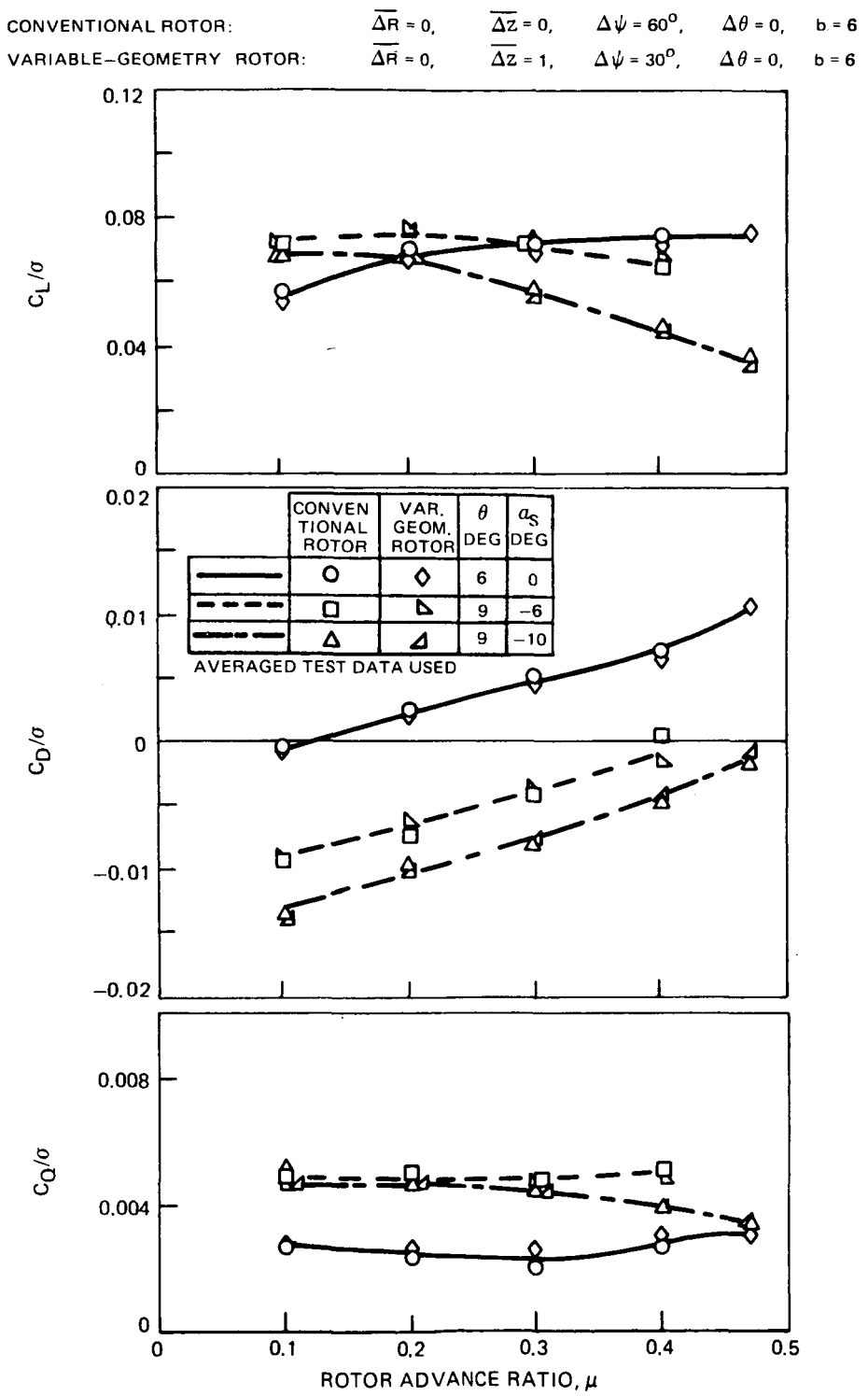

(c) - Selected Control Settings and Varying Advance Ratio.

Figure 45. - Concluded.

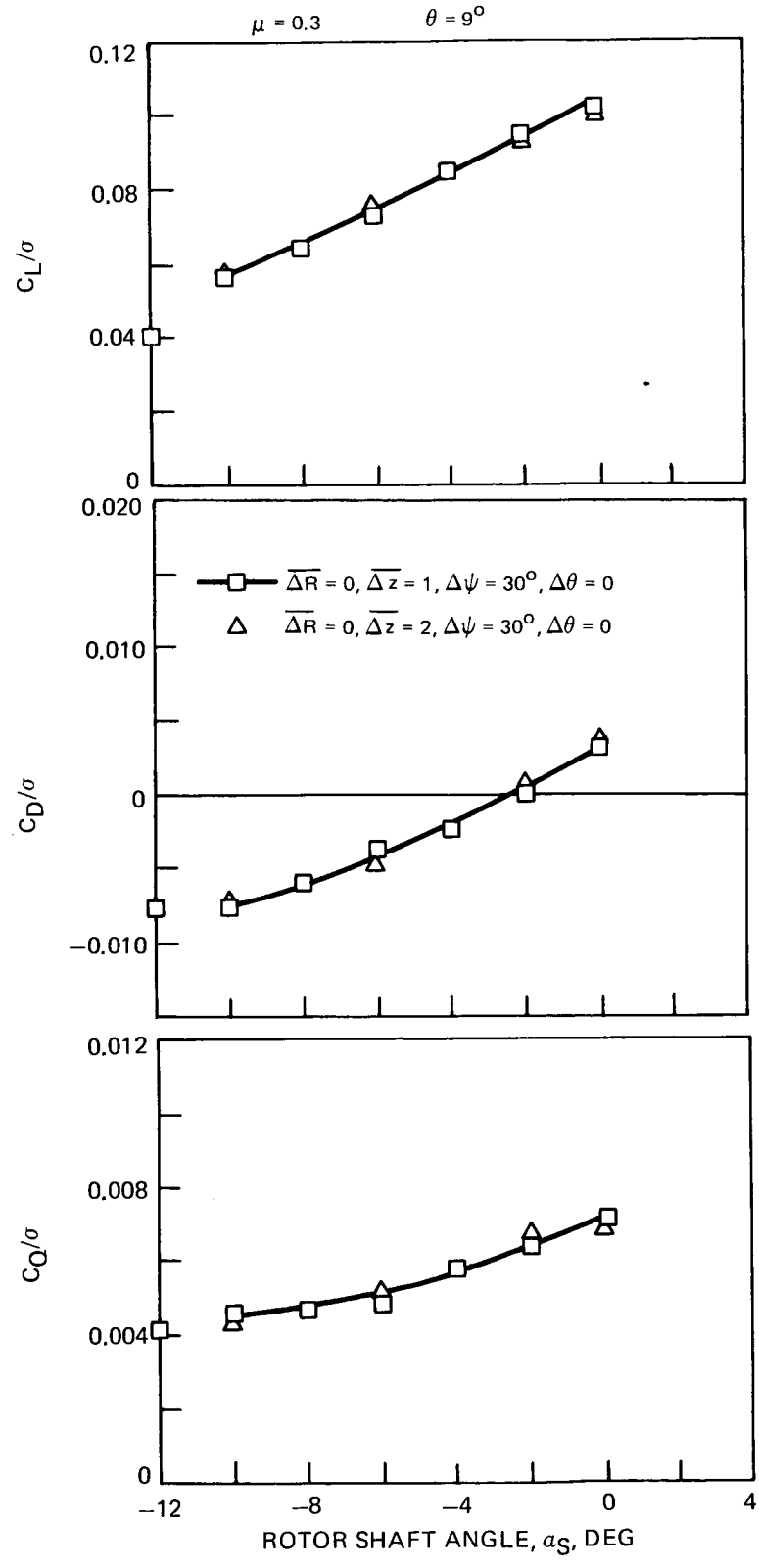

Figure 46. - Effect of Increased Axial Spacing on Forward Flight Performance.

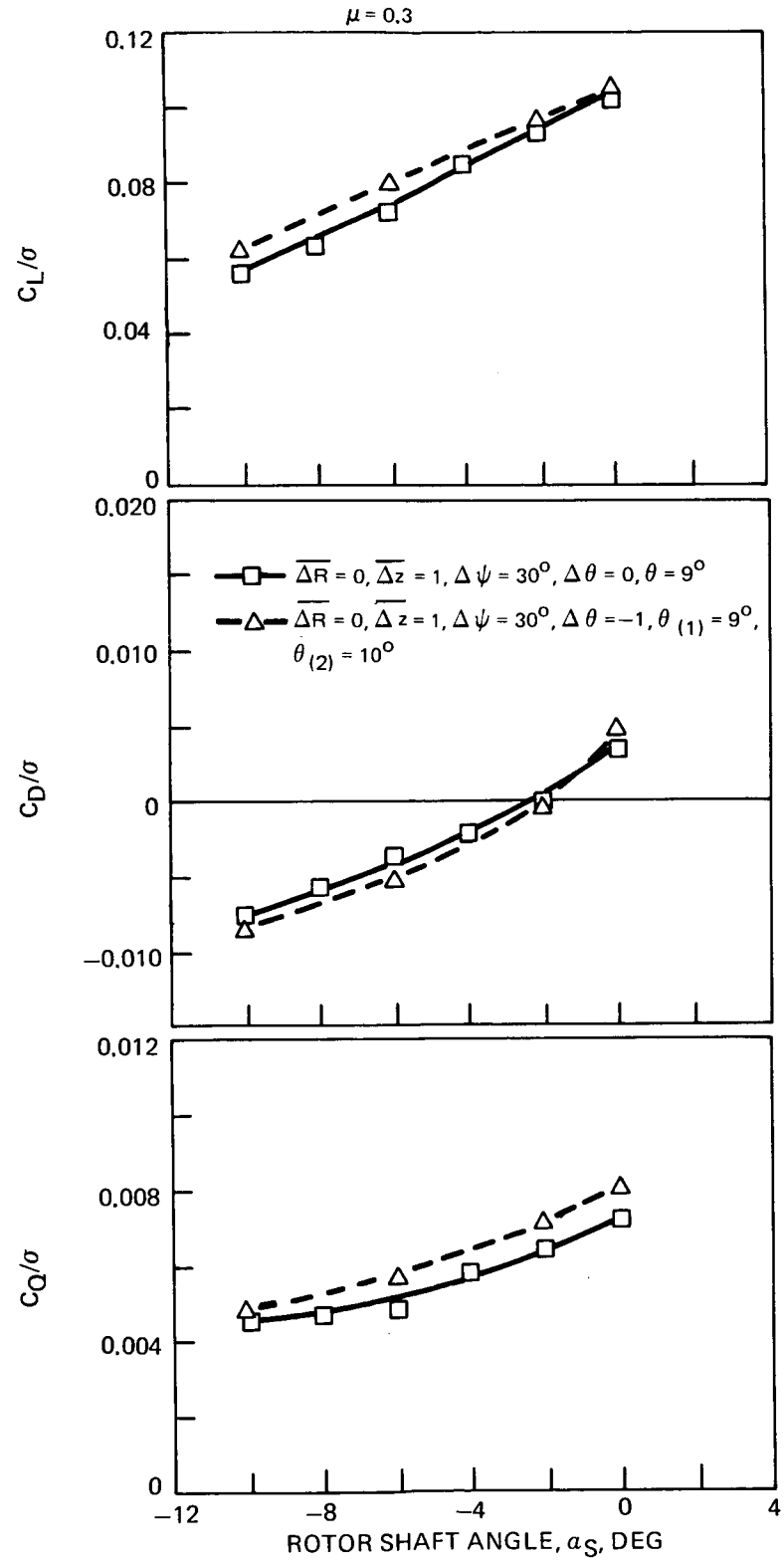

Figure 47. - Effect of Differential Collective Pitch on Forward Flight Performance.

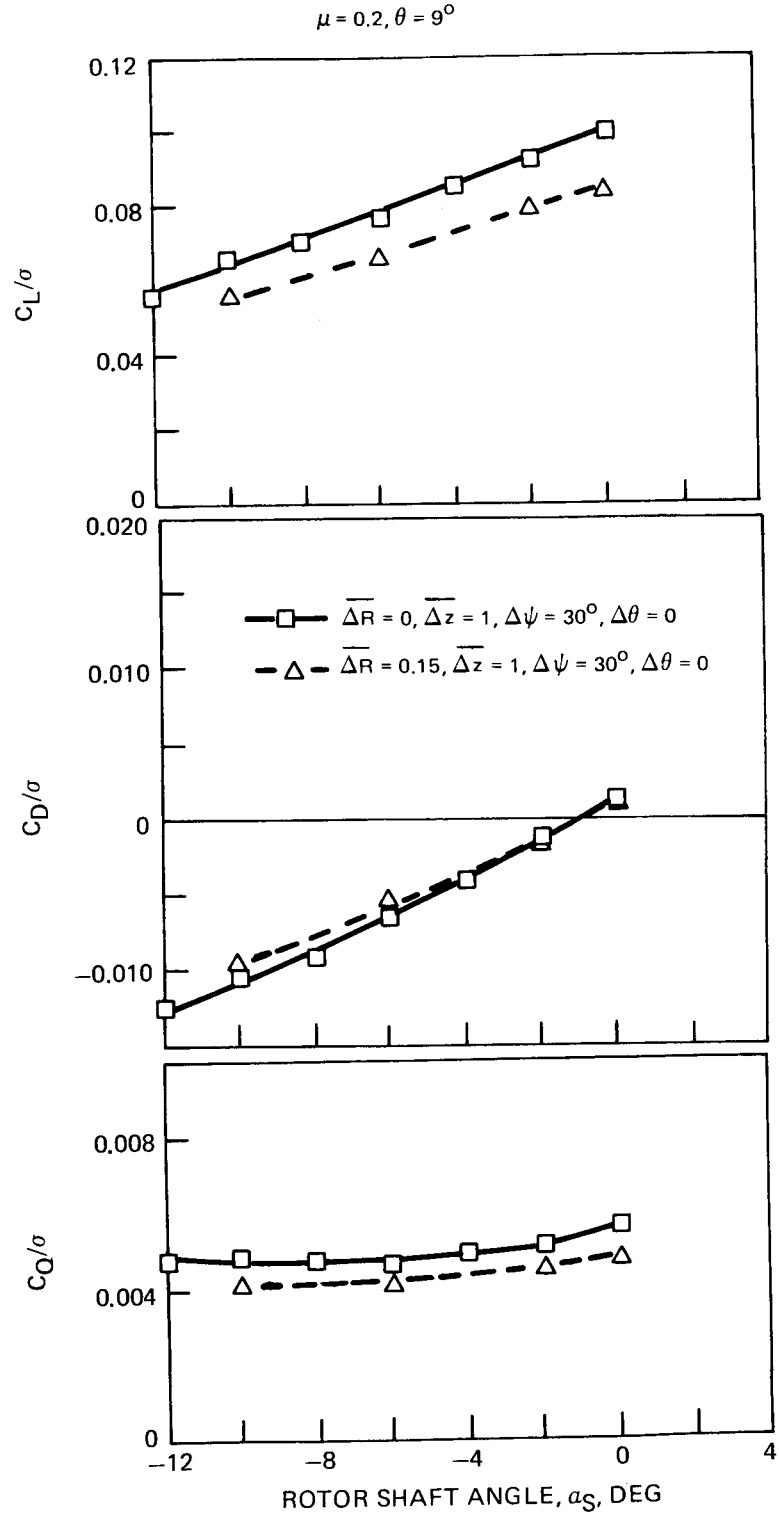

Figure 48. - Effect of Differential Radius on Forward Flight Performance.

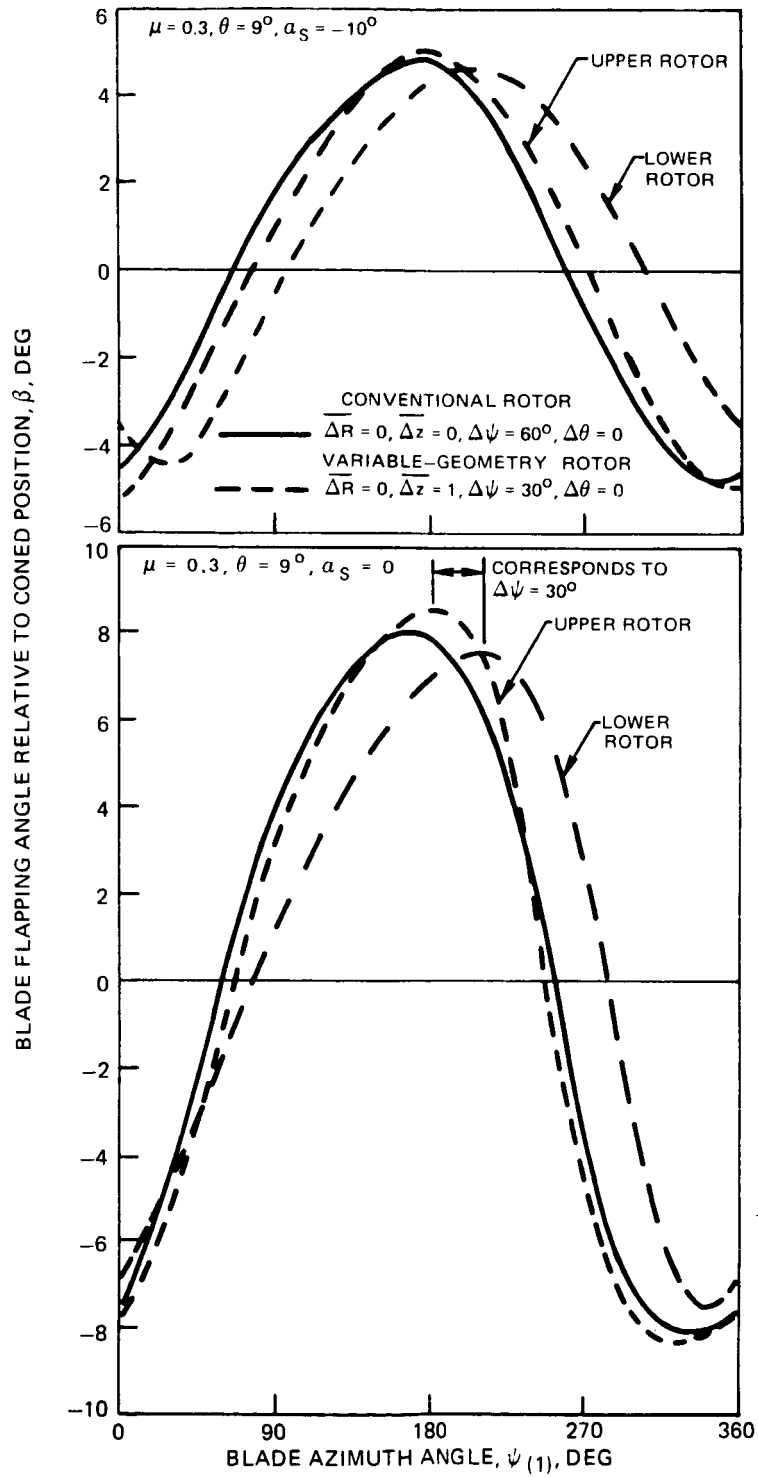

Figure 49. - Comparison of Blade Flapping Angle for a Variable-Geometry Rotor and the Conventional Rotor.

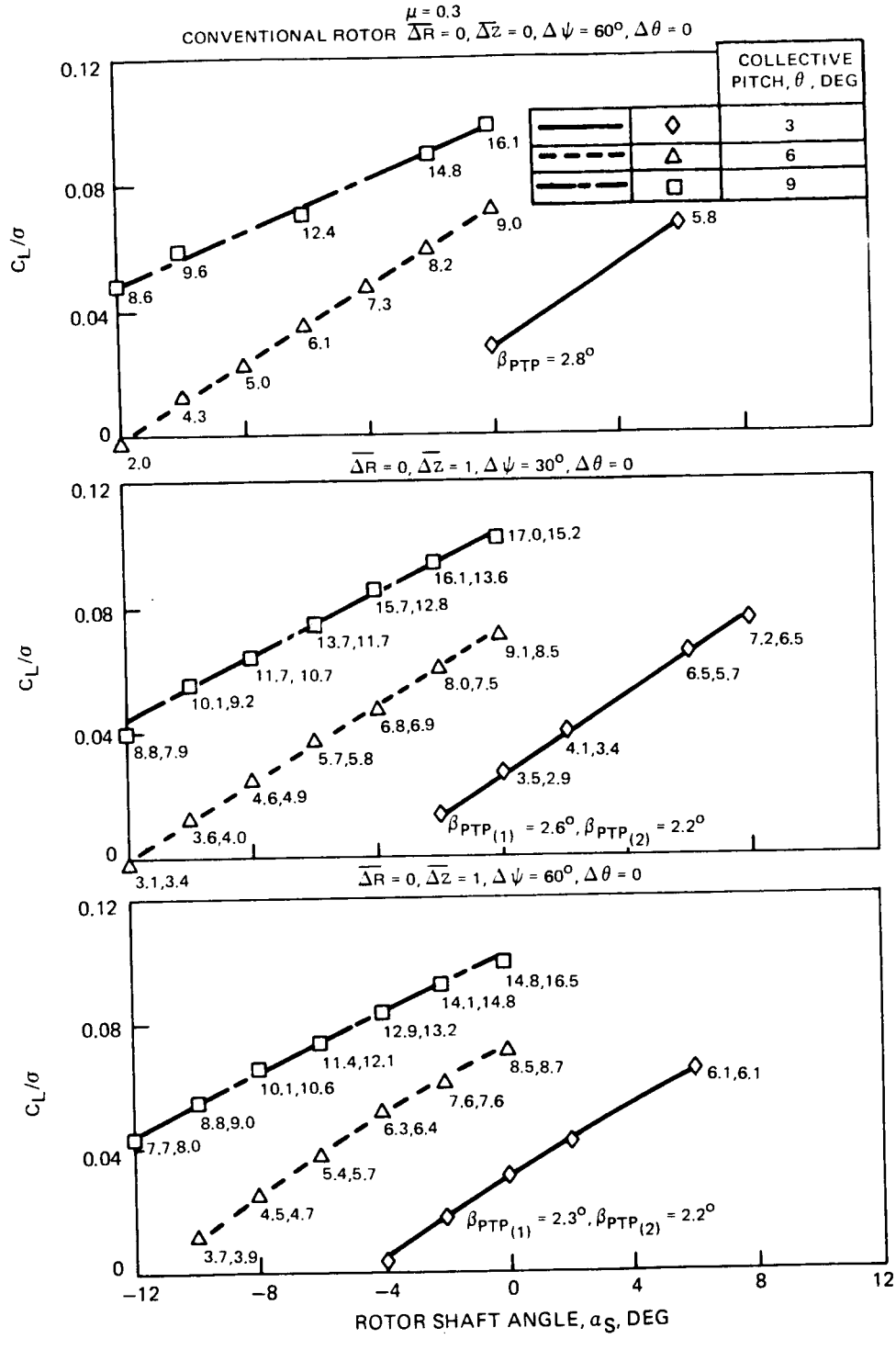

(a)

Figure 50. - Peak-to-Peak Flapping Angles for Various Rotor Configurations and Test Conditions.

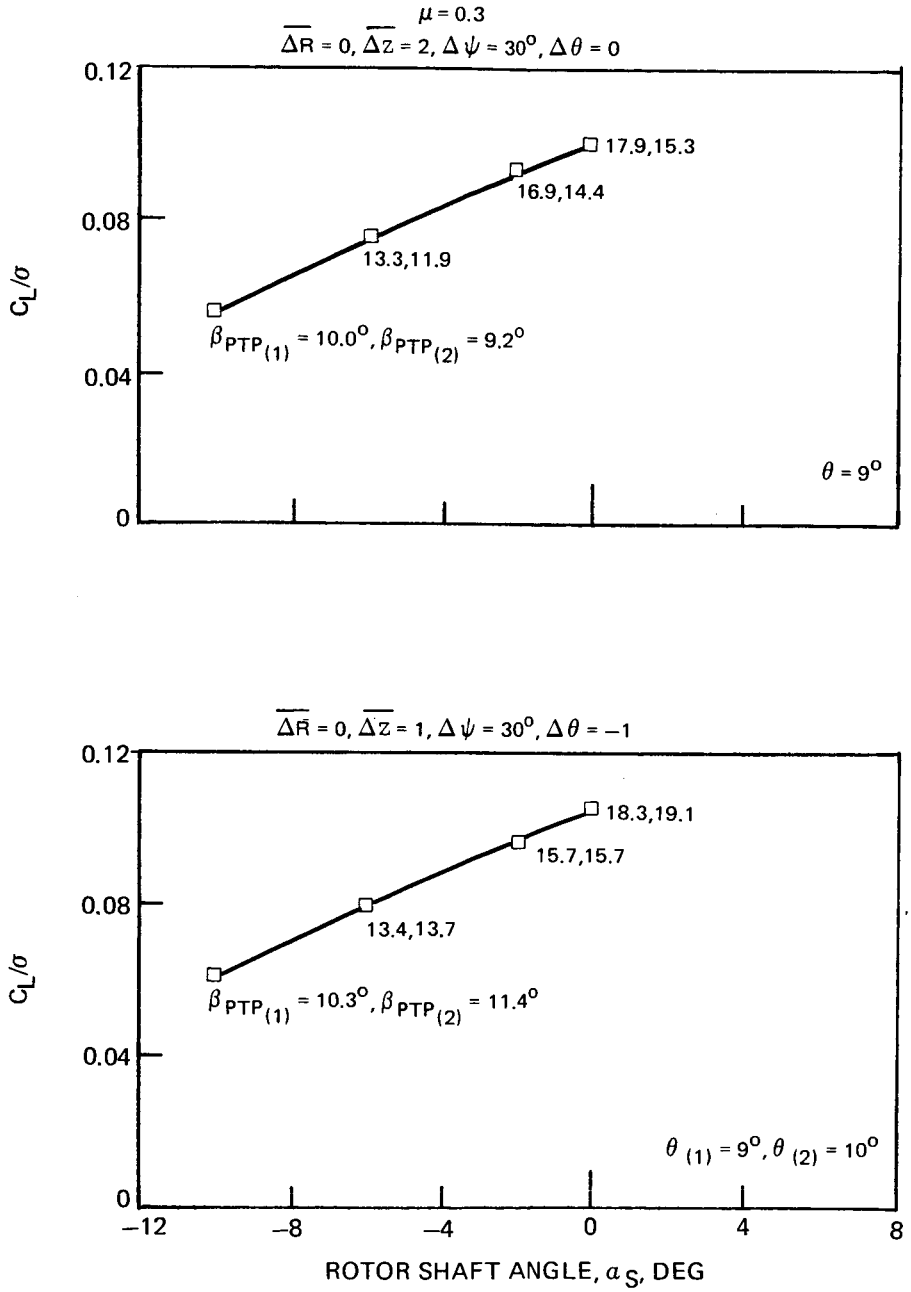

(b)

Figure 50. - Continued.

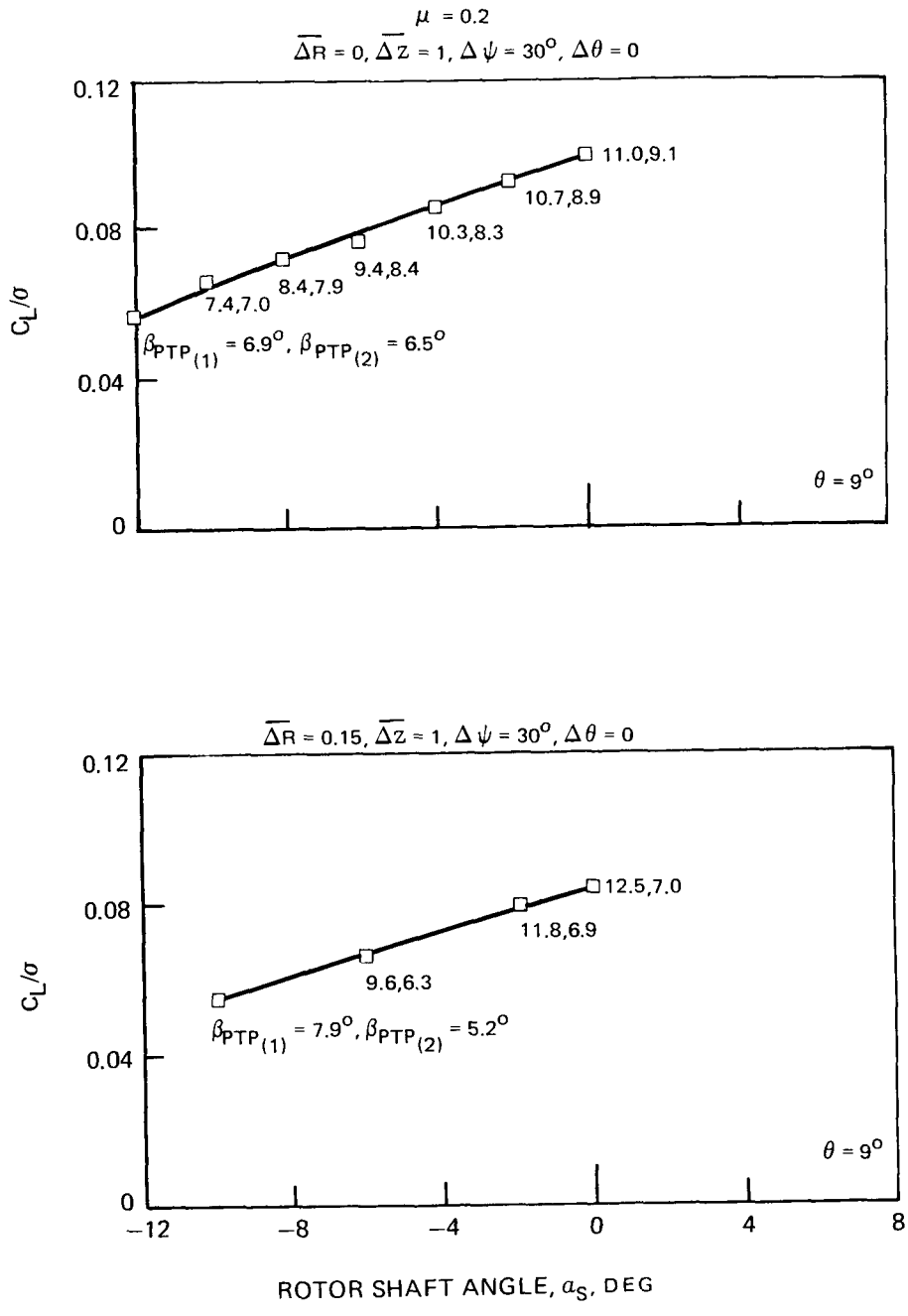

(c)

Figure 50. - Concluded.

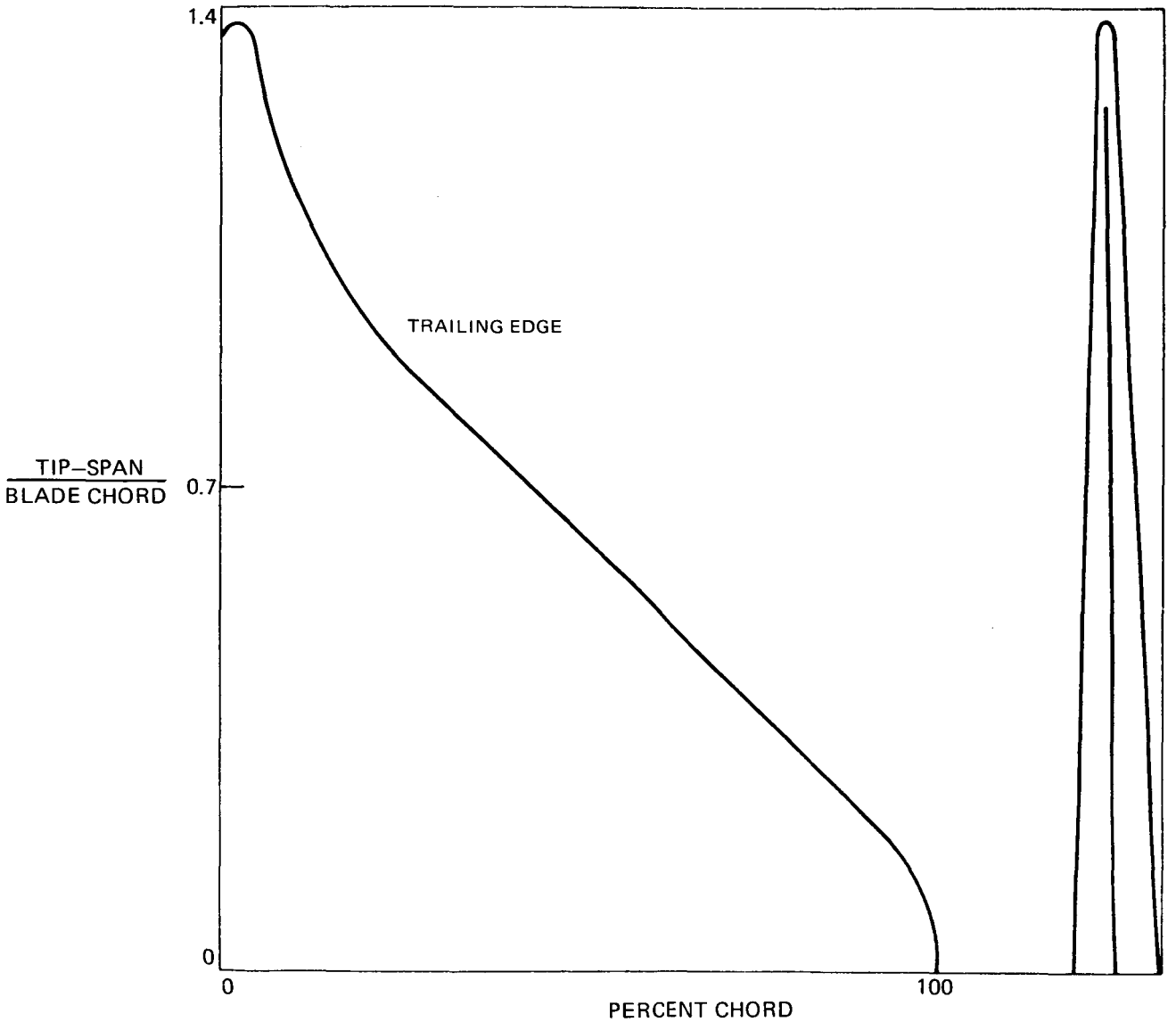

Figure 51. - Ogee Tip Planform and Edge View.

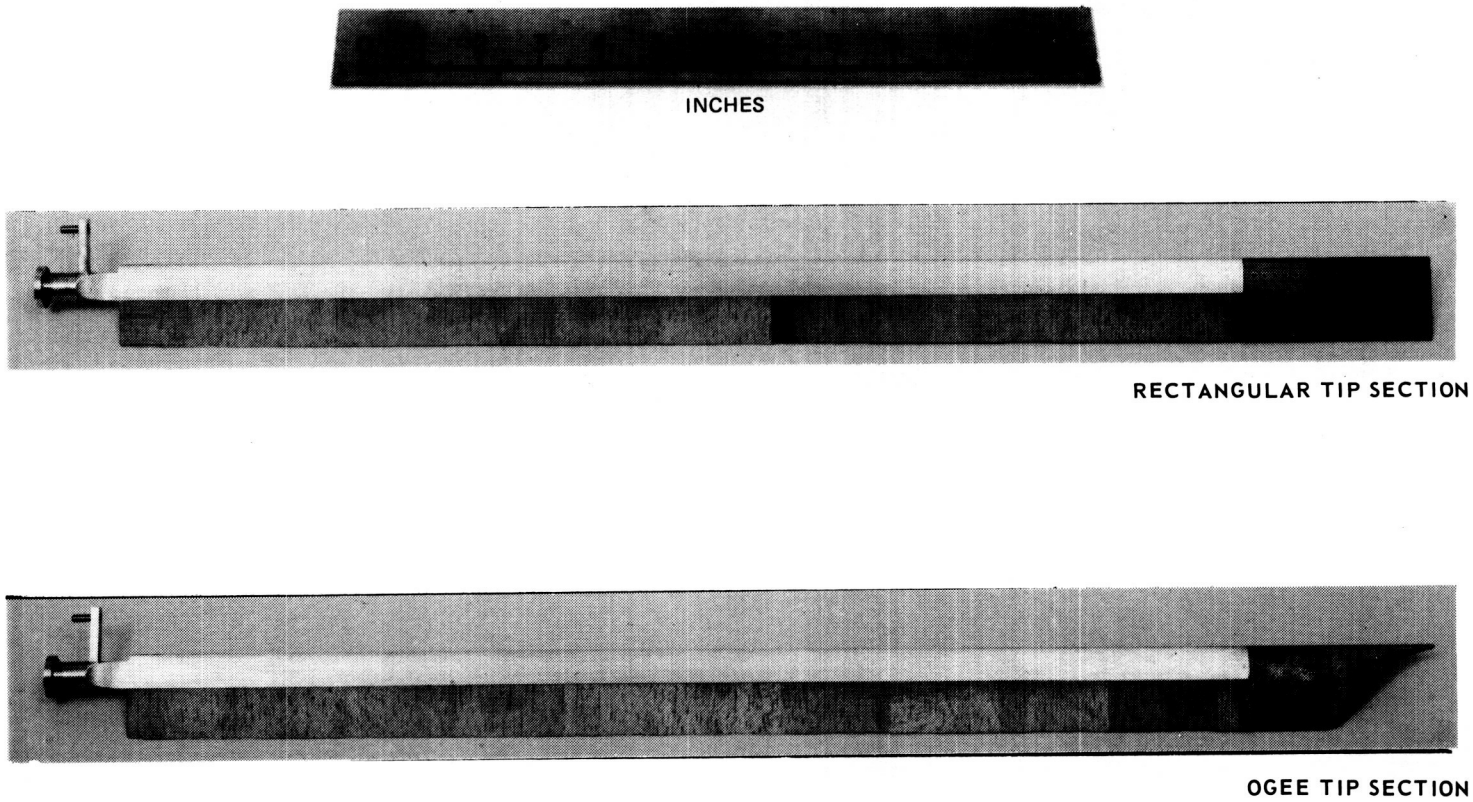

Figure 52. - Variable Tip Section Blades.

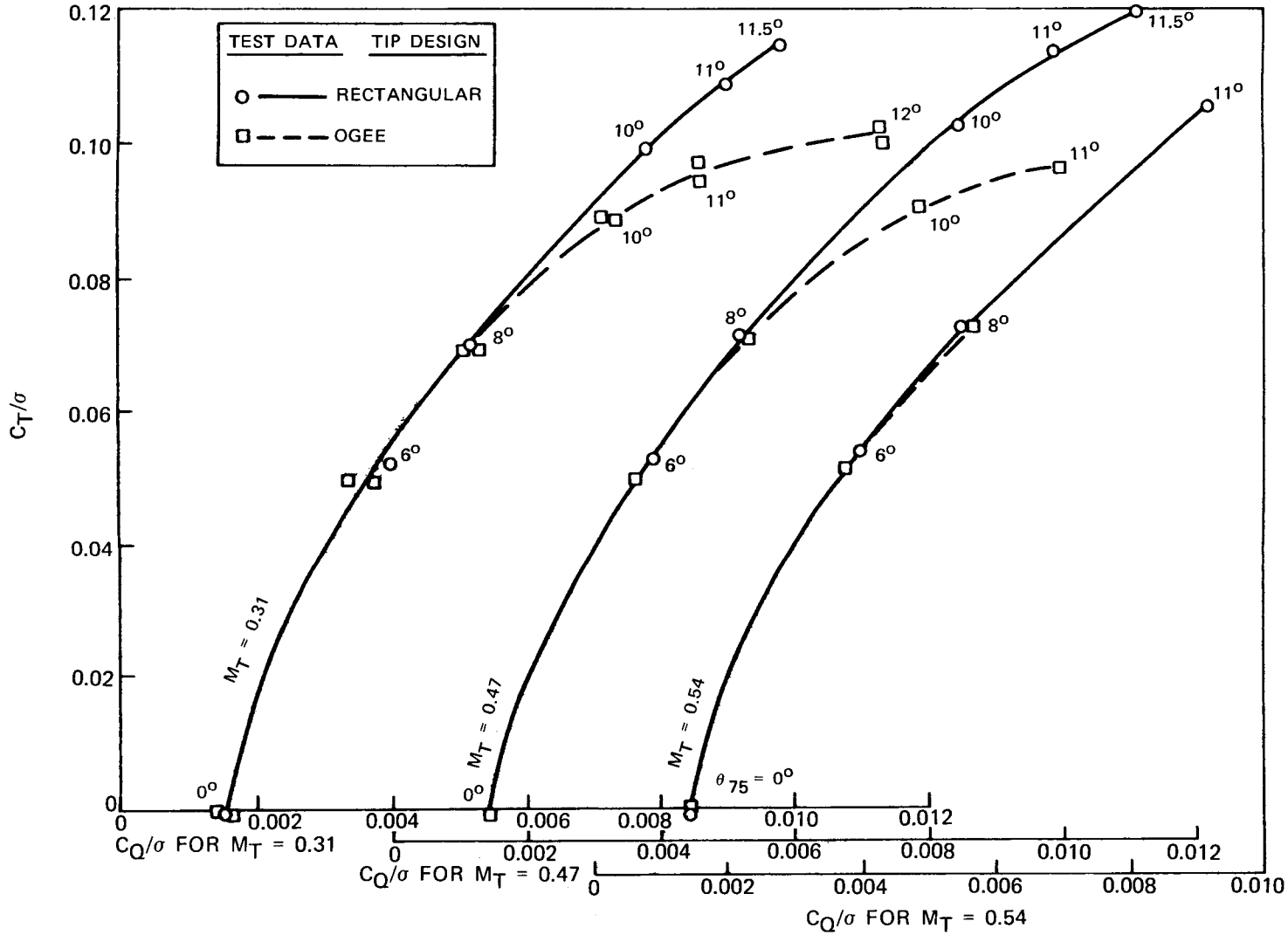

(a) - Three-Bladed Rotor, θ_1 = -8 deg.

Figure 53. - Comparison of Model Rotor Hover Performance of Blades With Ogee and Rectangular Tips.

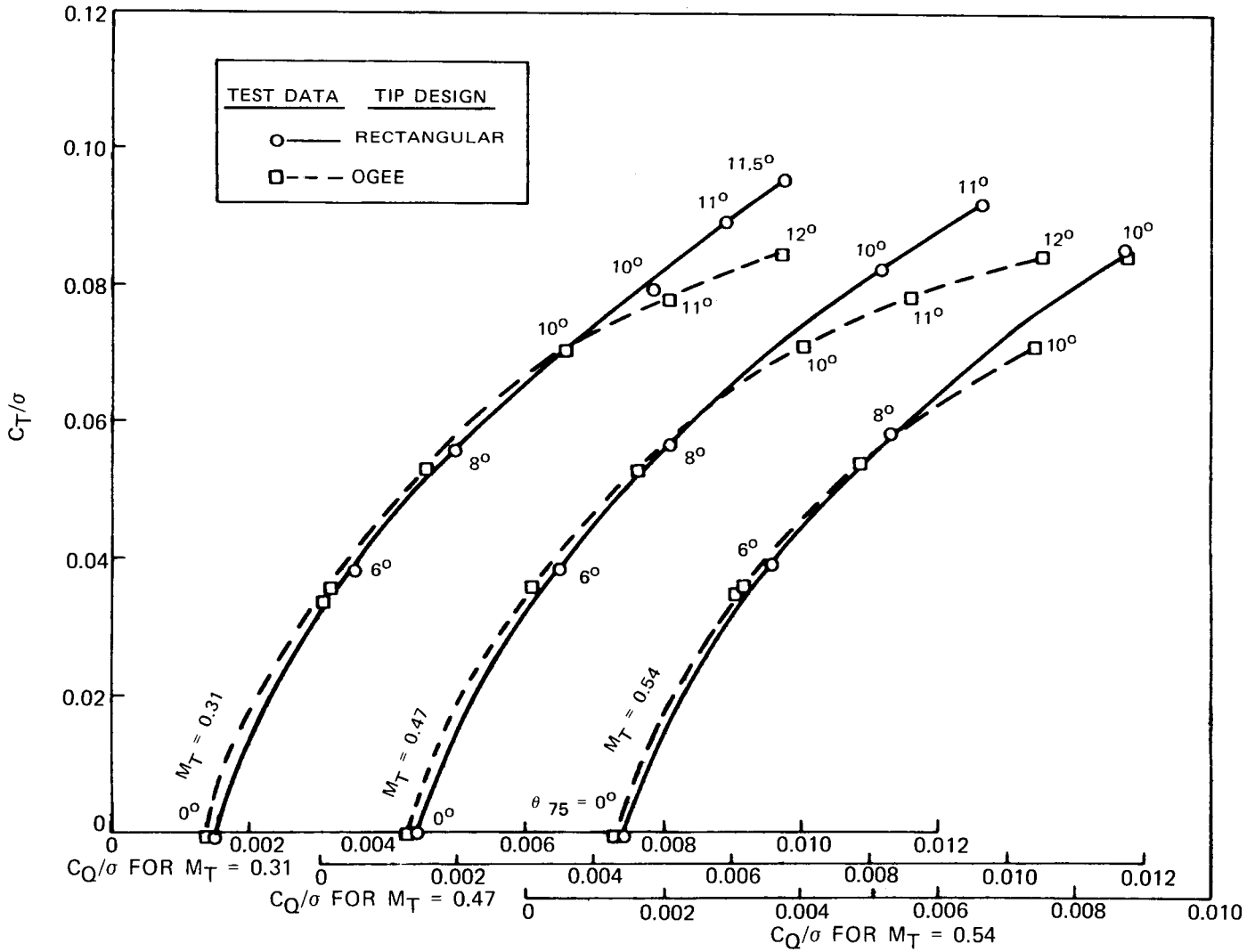

(b) - Six-Bladed Rotor, θ_1 = -8 deg.

Figure 53. - Concluded.

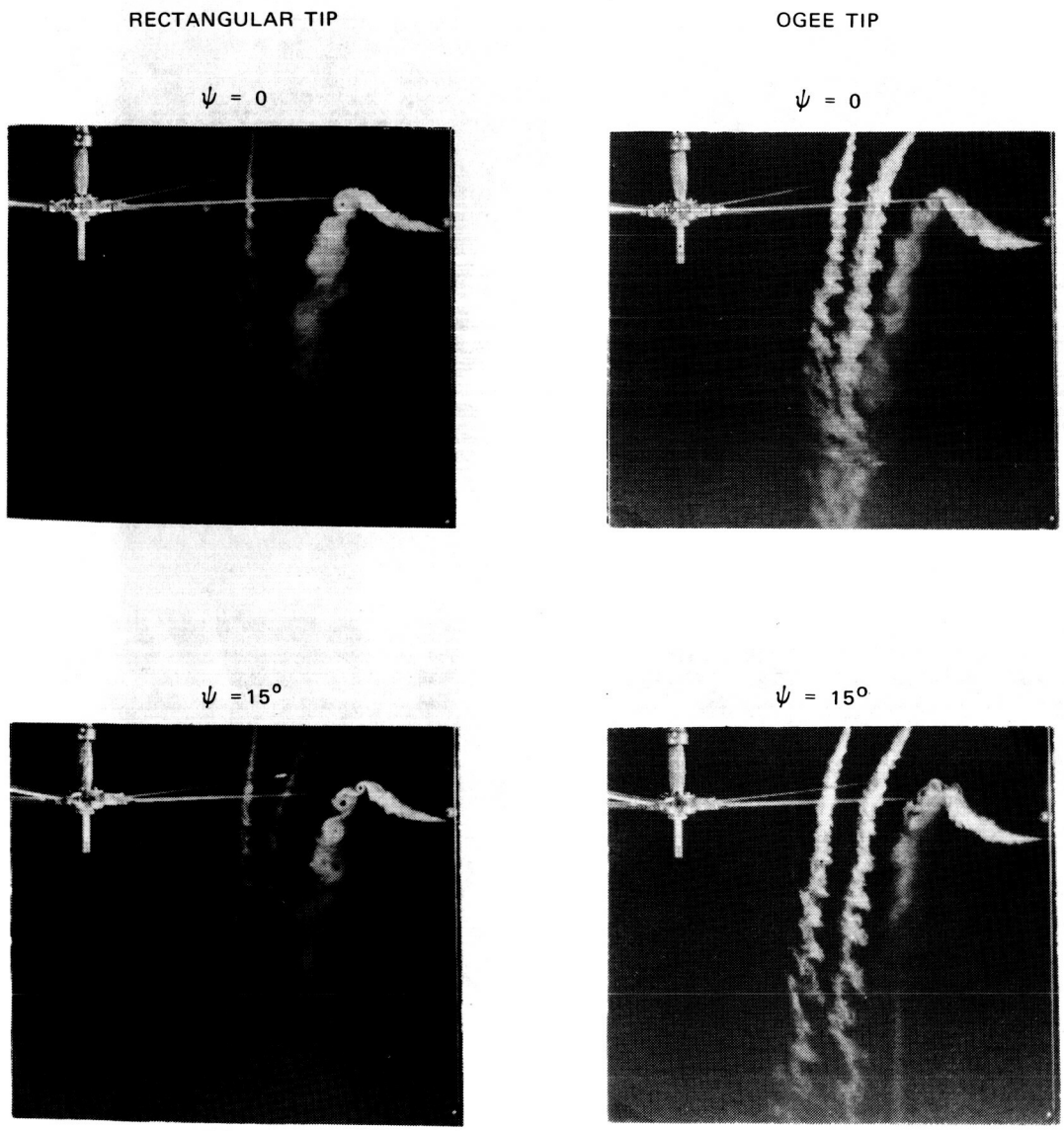

(a) - Six-Bladed Rotor

Figure 54. - Comparison of Flow Visualization Results for Rotors With Ogee and Rectangular Tip Sections.

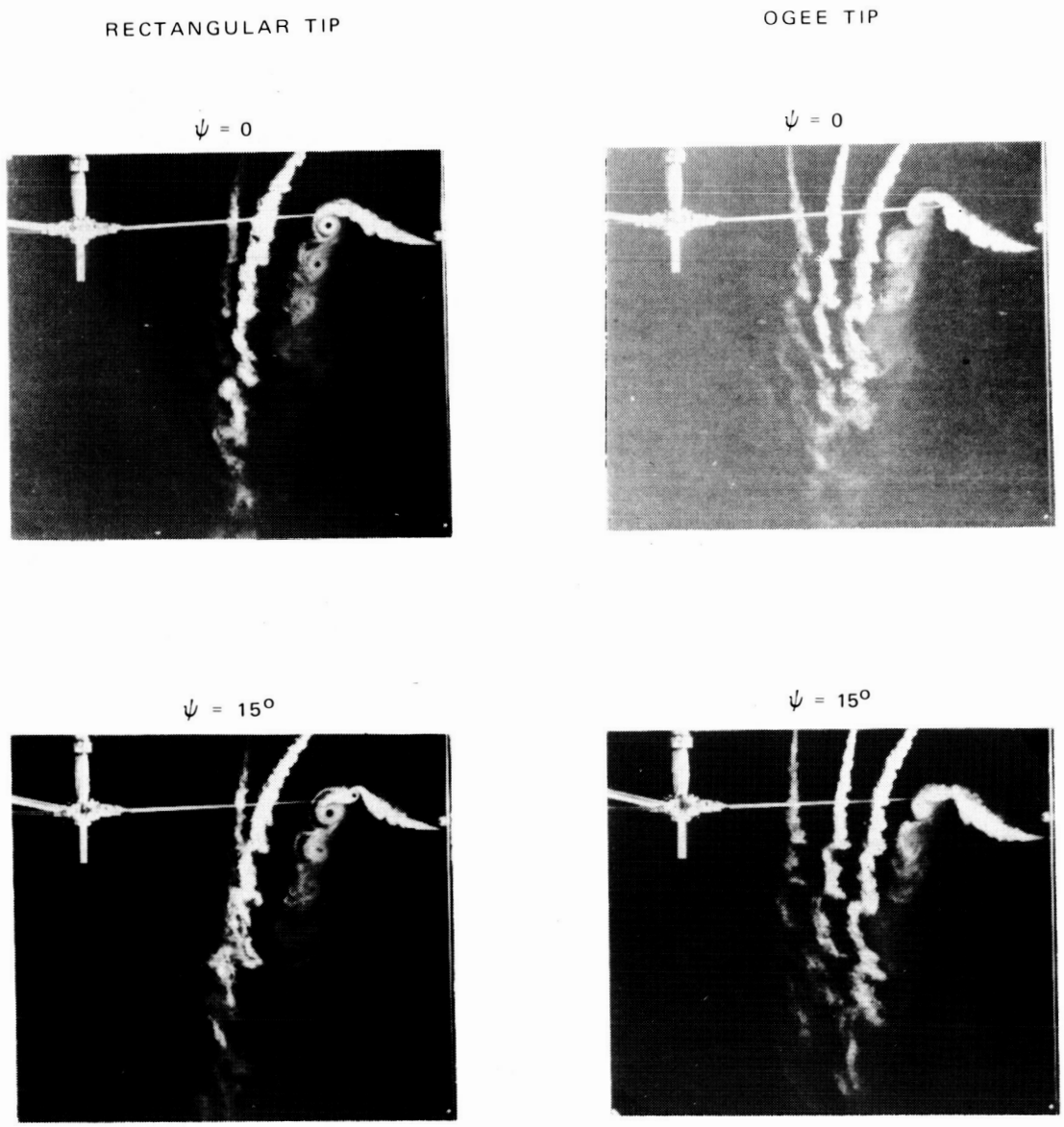

(b) - Three-Bladed Rotor

Figure 54. - Concluded.

*U.S. GOVERNMENT PRINTING OFFICE: 1974-739-157/88